# MSc Thesis

## Evaluation of Grid-Stiffened Structures For Applications on Drones

Y. Elnily


TU Delft

# MSc Thesis

# Evaluation of Grid-Stiffened Structures For Applications on Drones

by

Y. Elnily

to obtain the degree of Master of Science
at the Delft University of Technology,
to be defended publicly on Wednesday January 18, 2023 at 09:30 AM.

| | | |
|---|---|---|
| Student number: | 4668669 | |
| Project duration: | February, 2022 – December, 2022 | |
| Thesis committee: | Prof. dr. ir. C. Kassapoglou, | TU Delft, supervisor |
| | Dr. ir. O. K. Bergsma, | TU Delft |
| | Dr. ir. D. M. J. Peeters, | TU Delft |
| | Ir. B. J. R. Smeets, | ATG Engineering B.V. |

Cover: Pipistrel Nuuva V300 Cargo Drone [35].

An electronic version of this thesis is available at http://repository.tudelft.nl/.

TU Delft

ATG europe

# Contents

# List of Figures

# List of Tables

# List of Appreviations

Table 1: List of Abbreviations

| Abbreviation | Meaning |
|---|---|
| VID | Visible impact damage |
| BVID | Barely visible impact damage |
| AGS | Advanced grid-stiffened structures |
| RBE | Rigid body element |
| EASA | European Aviation Safety Agency |
| MTOW | Maximum takeoff weight |
| NDT | Non-destructive testing |
| UD | Uni-directional |
| WP | Work package |
| TTS | Technology transfer study |
| DASML | Delft Aerospace Structures & Manufacturing Laboratory |

# Acknowledgments

Firstly, I would like to thank ATG for giving me the opportunity to work on this project, it was a great opportunity with a lot of experience and knowledge gained. A big thanks to the entire composites team, and special thanks to Bart for his continuous support, and before him Camille.

On the TU Delft side, Prof. Christos Kassapoglou provided a great and continuous support. I cannot thank him enough, thanks for being very responsive whenever I send an email or ask for help, thanks for your constructive feedback, thanks for cheering me up during the hard times, thanks for everything. My happiest moments during the thesis were those when I saw you excited about my work or the results, it is my pleasure to work with you.

The project marks the end of my journey at TU Delft, which started back in 2017. This journey, which started as a dream when I was in high-school, would not have been possible to achieve without the support from my parents and sisters, Somya and Habiba. No words can describe how grateful I am to have you in my life. The worst part of this journey was that, I always missed you.

This project will always remain special to me, not just because of what is mentioned above, but also because I got married to the love of my life, Sarah, during the project. She knew it all when I was exhausted and when I felt burned out, and she was always the cure. Thank you for being by my side, sharing the good and bad times, and I wish us a happy life.

Last by definitely not least, a large part of the duration of this project was spent in the laboratory on manufacturing and testing. I would like to thank all the TU Delft laboratory staff for their help and instructions. And thanks to my laboratory friends who helped whenever needed help, special thanks to Mohamed El-Alfy.

*Y. Elnily*
*Delft, January 2023*

# 1

# Introduction

The use of grid stiffened structures has been increasing noticeably over the last few years, thanks to their good specific and damage tolerance properties. The grid-stiffened structure typically consists of load bearing ribs that can form iso- or aniso-grid patterns with a skin attached either on one or both of the grid, which allows for a more tailored design depending on the loading conditions. A well-known application within the aerospace industry is launchers' inter-stages and fairings. [3] A very limited number of aircraft models made use of that type of structure, and consequently, limited information can be found in the literature about the use of grid-stiffened structures in aeronautics, with one of the most well-know application being the Vickers-Wellington aircraft. [27]

A structural concept that was proven to be suitable and good for one application, is not necessarily as good for another application. That is due to the different design requirements, financial constraints, or loading conditions associated with the different applications. For example, the damage tolerance requirements of aircraft can easily result in many structural concepts or materials being unsuitable for this application despite their high strength. That being said, this project is evaluating the suitability of using grid-stiffened composite structures for applications on drones. This was done by making use of an existing design as a reference design, replicating the same design using grid-stiffened structures, check compliance with damage tolerance requirements, and comparing the weight of the new structure with the mass budget provided by the industrial partner. The project was done in collaboration with different industrial partners, including the one which provided the technical data and requirements to ATG. The project history is further discussed later in this chapter.

The document is structured as follows: it starts with presenting the literature study done before the start of the thesis work in chapter 2, which is concluded by formulating the research question. In chapter 3, the approach taken to answer the research question formulated in the subsequent chapter is explained. This is then followed by the two main work packages in the project, modelling and manufacturing & testing, in chapter 4 and chapter 5, respectively. The results from these two chapters are listed and discussed in chapter 6; which is followed the conclusion and recommendations in chapter 7. In this chapter, the research questions are re-visited, followed by a list of recommendations for future work in this area.

## Project history and objective

This project started as a technology transfer study (TTS) for ESA [1]. The reason for this project from the perspective of ATG Europe B.V. is that ESA is looking if ATG could apply their space technology to non-space applications, where in this specific project ATG decided to look at large drone fuselages. With ATG being an expert in the development of grid-stiffened structures, [29, 32, 33, 34] the proposal was to look into the potential of using grid-stiffened structures in the aeronautics industry. In this section, the research plan to be followed in this literature study is explained.

[1] The views expressed herein can in no way be taken to reflect the official opinion of the European Space Agency

The first step in this project was to find a reference airplane model on which this research can be based. It was decided by ATG to collaborate with an aircraft manufacturer in Europe. They were willing to provide the technical data for their new cargo drone shown in Figure 1.1, a concept unmanned cargo drone; which is close in size to light aircraft. This means that the results of this research can be generalized, to some extent, to aircraft within this weight category. The technical information provided by industrial partner included, but not limited to, technical drawings of the current design, material properties, structures and payload masses, production costs, etc.


Figure 1.1: Pipistrel Nuuva V300 aircraft [35]

The objective of the project was then defined as follows:

> "To evaluate the feasibility of using grid stiffened structures on drones by means of optimizing, manufacturing, and testing of a grid stiffened drone fuselage and comparing it to the existing design."

# 2

# Literature study

Lattice structures and grid-stiffened structures, two terms that are used interchangeably in the literature. In this chapter, the differences between the different terminologies is explained, followed by a more detailed and project-related discussion, which covers the manufacturing, modelling, and failure modes of grid-stiffened structures. In the first section, chapter 2, an introduction to grid-stiffened structures is given, followed the explanation of their design parameters in section 2.2. The manufacturing and modelling of grid-stiffened structures are explained in section 2.3 and section 2.4, respectively. The failure modes and the effect of the design parameter on the failure modes are discussed in section 2.5. Airworthiness regulations, from which the damage tolerance requirements originate, are reviewed in section 2.6, followed by section 2.7 where the applicability of the results of this project on different aircraft is discussed. Finally, the chapter is concluded in section 2.8, where the research questions are formulated.

## 2.1. Introduction to Grid-stiffened structures

Lattice and grid-stiffened structures have not just been used within the aerospace industry, but for other applications requiring light structures with good mechanical and damage tolerance properties as well. Unlike in the aerospace industry, where the use of composites is dominant, the isogrid structures have been built using other materials since the last century. A well-known application is the Russian radio tower, which was made from metal. Following that, a recent research highlighted the potential of using grid-stiffened structures for armoring applications. [31] In addition to the 2D parameterization of lattice structures, they have also been researched for 3D printing application where they are optimized in a very tailored way to conform with two aspects: individual struts aligns with the principal stress and struts on the boundary capture the curved nature of the optimized structure. This type of structure, known as Conforming Lattice Structures, allow for the manufacturing of any shape while minimizing its weight. [43] An aerospace-specific application for this type of lattice pattern is, composite-based active morphing wing. [21]

The increased use of grid-stiffened structures in the aerospace industry started in the 70s of the previous century, where several composite isogrid launch vehicles were flown in the Soviet Union. [18] At this time, however, the full potential of grid-stiffened structures was not realized due to the low fiber-volume fraction and poor part quality. A renewed interest in grid-stiffened structures took place at the end of this century, where the production of higher quality product was easier, and more composites knowledge became available. In the 1997, a composite grid-stiffened payload shroud was built and flown by the US Air force Research Lab, which was 61% lighter, 300% stronger, and 1000% stiffer than the preceding aluminum structure. Before this period in the US, the McDonnell-Douglas Corporation, currently part of Boeing group, lied the foundations of grid-stiffened structures where they held the patent right for the development of the first aluminum isogrid, which formed the basis structures for the shrouds and interstages of a few launch vehicles later, including Delta, Atlas, and Titan. [18] Other applications also included MightySat I satellite, Delta II, and the Minotaur launch vehicles. Recent research investigated the use of Grid-stiffened structures for Ariane 6 as well. [29]

When it comes to the applications within the aeronautics, however, a limited number of aircraft were flown. A few examples were found in the literature, but not much about the design of these aircraft was found. The main reason is that most of them were either for military application or developed by defense institutes, hence, very confidential projects. Well-known applications include the Wellington aircraft,[27, 41] a British bomber that was built and flew during WWI, and the Russian turboprop IL-114 aircraft [41], Figure 2.1; which was 60% lighter than the aluminum structure, this percentage goes down to 40% when considering the end rings, door, joints, etc. [41] Another project done in the 90s by Scaled Composites of Mojave, CA, where they developed a grid-stiffened structure fuselage for its V-jet, Boomarng, and Vantage demonstrator aircraft. These aircraft, however, never made it to production with grid-stiffened structures. [18]

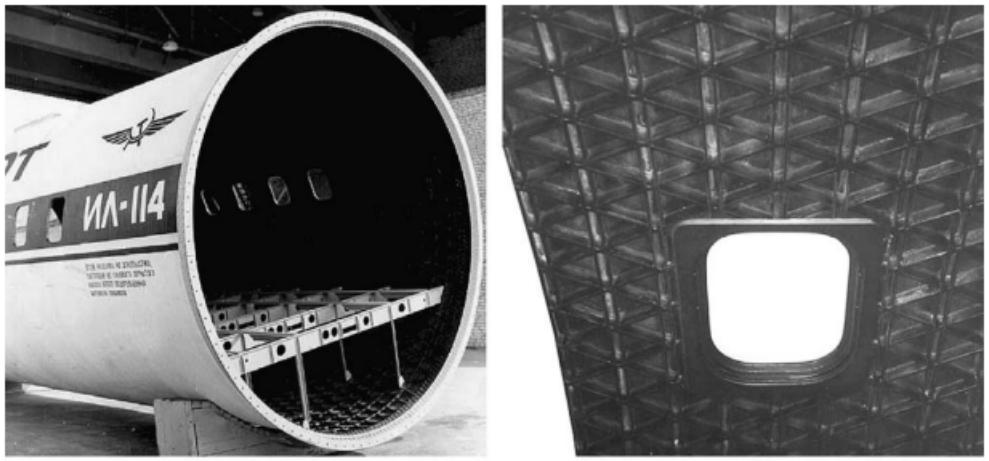


Figure 2.1: Grid-stiffened fuselage structure

## 2.2. Design and parameterization

Lattice structures can be divided into different types, while the nomenclature is inconsistent in the literature, three main types exist: Orthogrid, Isogrid and Anisogrid structures. They can often be designed with a thin shell/skin, either on both sides or on one side, in which case they are referred to as grid-stiffened structures, since in that case, the grid works as the stiffening elements for the skin. The differences between the different grid types are illustrated in Figure 2.2 and the possible skin configurations are shown in Figure 2.3. While those remain the main types, a less-popular class of grid-stiffened structures exist, where the ribs do not form regular patterns, but fibers are steered to provide stiffness wherever needed. This class is often referred to as Advanced Grid-Stiffened (AGS) structures. [28] An example for this is shown in Figure 2.4, where ribs form curvilinear grid-patterns [2]. Although this type of structure expand the design space a lot, they also add complexity both to the optimization and manufacturing efforts. Hence, only traditional types are considered in this study, and the name grid-stiffened structures will be consistently used.

One of the main concerns that arise with grid-stiffened structures is, how easy is it to repair them. [18] Sources in the literature focused mainly on the development without diving deep in the maintainability of the structures, one research was found where they used patches on both sides of the structure to repair the damage. [16] However, the decision seemed arbitrary and no attempts were made to explore the most suitable technique. This raises the question about how optimal is this technique, and whether the repaired structure retain the same mechanical properties as the original one or not. It is expected, however, that the difficulty of the repair is associated with the damage type, for example, a fiber breakage in the rib is probably more critical than rib-skin separation, and just using patches might not be enough depending on how this part is loaded. Depending on the repairing techniques, curvilinear grid-stiffened panels can be more difficult to repair. For example, warping can be expected near the skin-rib interface and along the curved rib for curvilinear grid-stiffened structure if patches are used, which might not be favorable. If an existing composites repair method is proven to be working

for grid-stiffened structures, tailoring or even changing the method might be necessary for advanced grid-stiffened structure. Due to the nontraditional patterns which share less similarities with the existing, the structures for which these methods were deemed plausible.

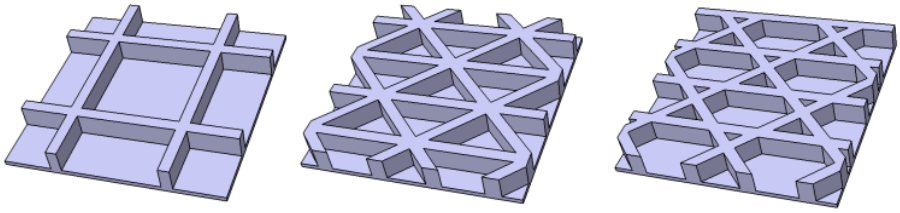

Figure 2.2: Different grid types

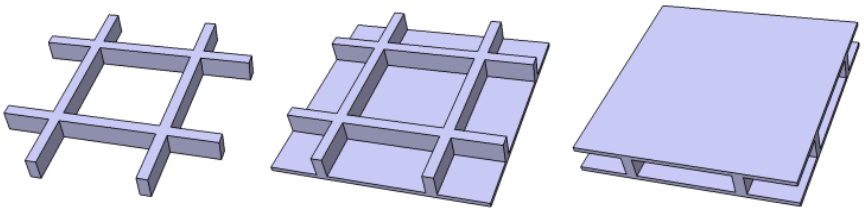

Figure 2.3: Skin configurations of lattice structures

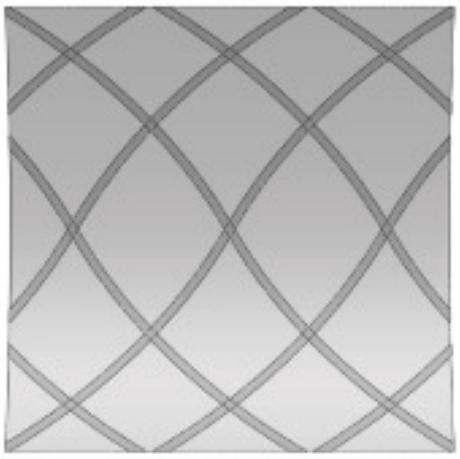

Figure 2.4: Curvilinear Grid-stiffened panel

Grid-stiffened structures consist of helical ribs, axial ribs, and hoop ribs, from which most of the structure parameters originate. The axial ribs considered to lie in the primary or the $0^o$ direction, hoop ribs in the $90^o$ directions, and helical ribs often have the same angle in two opposite directions $\pm\phi$ measured from the $0^o$ axis, which makes the first design parameter. Then comes the ribs separation, rib height, rib width, and skin thickness (if applicable), a visual presentation of the parameters can be seen in Figure 2.5. In case of the presence of skin, the angle of the plies is measured similarly to the helical ribs. It should be noted, however, that, it is more common to have either hoop or axial ribs and not both. The underlying difference between the isogrid and anisogrid is their grid parameters, where the parameters in the first one results in a semi-isotropic behavior of the structure. While for the later one,

the grid can provide anisotropic behavior. [30] This means that for isogrid structures, the ribs form equilateral triangles, which reduces the number of grid parameters. While this could simplify the design, the anisogrid structures provide a more tailored design depending on the loading conditions, which can result in weight saving. Finally, it is important to note that lattice structures can be used for different geometries and shapes not only flat panels, a common example is cylindrical structures.

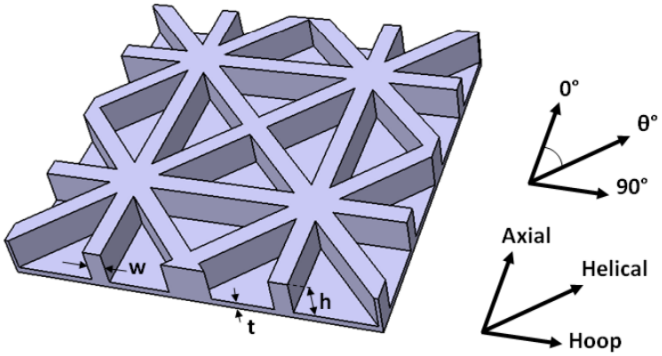


Figure 2.5: Key parameters of Grid-stiffened structures.

## 2.3. Manufacturing techniques

In this section, the manufacturing of Grid-stiffened structures is discussed. Since the material of the structure is often a decisive factor in the selection of manufacturing techniques, it is important to select the material first. As mentioned in chapter 2, in the early development stages of grid-stiffened structure, metals were used. For lattice structures without skin, one can expect that metal rods are either welded together or mechanically fastened. For Grid-stiffened structures, however, more options exist, for example, milling of thick metal plates, or other machining techniques. While for metal structures the processes might seem straightforward, that is not the case with composites. More design parameters affect the selection of the manufacturing technique, for example, type of polymer (thermoset or thermoplastic) and specification of the resin (viscosity, pot life, curing temperature, etc.) directly affect the manufacturing process and the curing cycle. The fact that more than one component needs to be added to manufacture the part makes the manufacturing process more challenging. Starting with the mixing ratio of the resin system to controlling the fiber volume fraction. The introduction of pre-impregnated fibers eliminated a small part of these challenges, but one still has to deal with the rest. Since it is already known that carbon fiber reinforced polymer is used for this project, only composites manufacturing techniques will be discussed.

Most of the techniques found in literature make use of the possibility to co-cure both the ribs and the skin together. However, the main concern is always getting the shape and dimensions of the ribs as intended. One method suggested an out-of-autoclave manufacturing process, using a combination of robotic winding and resin infusion processes. The process starts by grooving a carpet of expendable male flat mold reproducing the pattern of the ribs. Then a robotic arm winds the dry fibers in these groves, Figure 2.6. After the layup is complete, resin infusion tooling is prepared, and a set of heating copper tubes are placed around the laminate to control the curing cycle. [39]

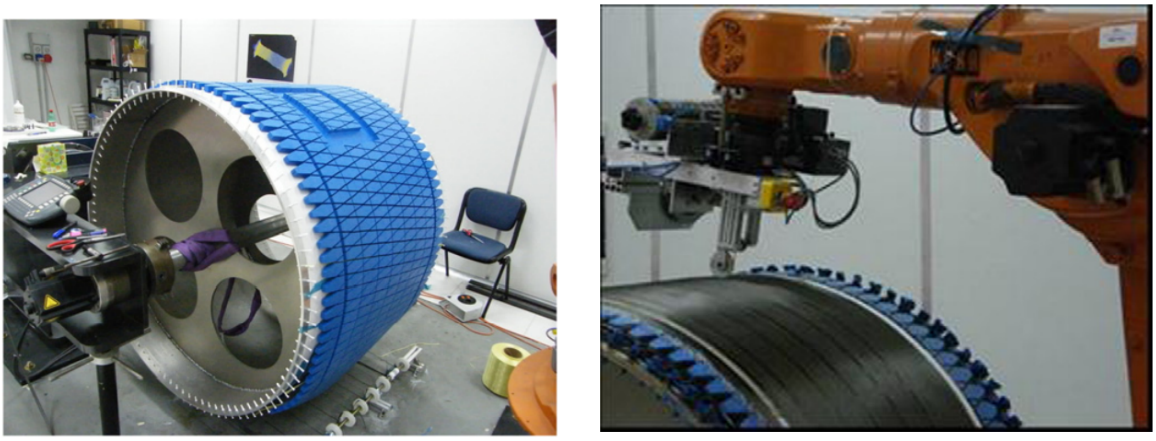

(a) Rubber carpet (b) Robotic arm

Figure 2.6: Manufacturing technique using robotic winding and resin infusion

While the grid-stiffened cylinder was successfully produced using this process, a couple of question arises about the quality of the final product. The set of copper tubes are used to heat the laminate locally and cure the parts of interest, but this did not prevent the rubber tooling from heating up and expanding, resulting in different ribs dimensions. It was found, however, that other researches worked on an improved thermal model that determines the final dimensions of the ribs based on the coefficient of thermal expansion of the used tooling. Reverse-engineering this method, one can use the right combination of tooling and pre-cured dimensions of the laminate to get the final dimensions as per the design. [19] While resin infusion can be limited by other parameters such as the viscosity of the used resin system and/or the details in the geometry of the structures, tow placement is often used with pre-impregnated (prepreg) fibers. This technique has the advantage of being feasible for both hand and automated layup processes.

Since the idea is to move to automated manufacturing later, the chosen manufacturing technique in this project should be representative for any future developments. Tow placement can be done either using in-situ curing or not. During in-situ curing, the placement head is fitted with a heat source where the pre-impregnated tape is placed and cured, it should be noted that in-situ curing is applicable only to thermoplastic structures. Tow placement is sometimes referred to as Automated Fiber Placement (AFP) in literature as well. The Herclues NASA ACT program has proved tow placement to have a low-cost nature compared to existing techniques, and showed the high utility and capability of tow placing robots. Higher costs are often expected if in-situ curing is not used; that is mainly due to the high costs associated with using ovens or autoclaves. Another advantage of using in-situ curing for grid-stiffened structures is that it is not necessary to use male molds or groove carpets similar to that shown in Figure 2.6. The technology was also used in the technology demonstrator in the European RLV program [13].

A very common application for grid stiffened structures is launchers' inter-stages, which are cylindrical structures. For such an application, tow placement can also be used. However, filament winding was also found to be used for cylindrical grid-stiffened structures. [7, 8] Unlike tow placement, where the placement of the fibers is controlled by the movement of a robotic arm placing the fibers precisely; in filament winding, the fibers, in both dry or pre-preg from, are wound around a mandrel under tension following the path of least resistance unless they are trapped either mechanically or by a special mandrel, the process shown in Figure 2.7. This makes tow placement a more common method for complex, high-performance products. [6]

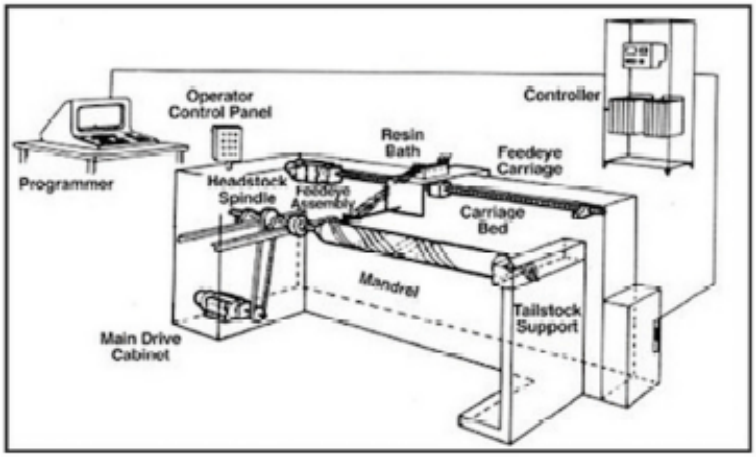


Figure 2.7: Filament winding process

Considering the fact that grid-stiffened structures are often used in cylindrical structures, both manufacturing techniques are deemed to be plausible, except for flat panels or non-cylindrical structures where tow placement has to be used. Either methods are to be used with a mold replicating the grid pattern to prevent crushing the plies from under the vacuum and/or autoclave pressure, except for the case when in-situ tow placement is used. While in-situ curing is still doubting and uncommon in case of using thermosets, other researchers looked into applying thermoplastics technology to the manufacturing of grid-stiffened structures; which might result in using in-situ curing more often in the future. This, however, might be limited to certain applications due to the difference in mechanical properties between thermosets and thermoplastics. [4].

## 2.4. Modeling of Grid-stiffened structures

When it comes to modeling of grid-stiffened structures, limited number of sources could be found in literature, out of them the work explained in the Isogrid Design Handbook by Mcdonnell-Douglas. [10] Which, at this time, focused more on metal isogrid rather than composites, meaning that not all the method mentioned might be applicable for composite structures. Most of the researches focused on optimizing, manufacturing, or testing of grid-stiffened structures and comparing their performance to existing structures, for which they used Finite Element Modelling (FEM) software programs. Few worked on developing an analytical model for grid-stiffened structures, such work can be found in [42, 23]. It was found that most of the work done focused on the buckling analysis of grid-stiffened structures, where they used smeared stiffness theory to predict global buckling of the structure.

Another study worked on a generalized analytical model to predict the static behavior without smearing, which was developed based on the classical laminate theory by treating the cell area as an inclusion and introduction of stiffness distribution function. Such a model, however, was not found to be used much in literature and still under development. Even though some researches proved the capability of such a modelling approach, they are very computationally expensive and not feasible for large structures. [42] Since this project focus on the evaluation of grid-stiffened structures for aeronautical application rather than modelling, FEM software will be used to predict test results, and no emphasis will be put in developing or verifying the model.

## 2.5. Failure modes of Grid-stiffened structures

Failure modes are always the main concern when coming up with a new design, since different design parameters and/or loading conditions can result in different failure modes. For example, if the specimen is loaded under axial compression, skin buckling is always expected to occur earlier than ultimate load of the structure; by increasing the skin thickness and/or reducing the cell size one can delay local buckling. While local buckling of the skin might not decrease the load carrying capability of the entirety of the structure, if the ribs are thin, they might be expected to buckle or cripple before failure, in which case global buckling will be considered the critical failure load. [42] In this section, the failure modes

under the most common loading conditions are discussed.

A study was done on the Minotaur launch vehicle payload fairing, which also looked into the failure criteria of the structure, of which skin-rib separation was selected as the critical failure criteria.[17] Local skin buckling occurred first, which increases the bending moment causing the skin to peel-off from the rib, which compromises the structural integrity of the structure. It was found that increasing the skin thickness increases the overall strength of the structure. The greater the skin thickness, the less the bending deflection and the lower the peel stress. The same behavior was noticed in another research, after skin buckling in the cells, matrix cracking occurs in the skin near the vicinity of the grid and propagates leading to ultimate failure by grid-skin separation. [38]

It is expected that a full-scale model, however, may behave differently. Grid-stiffened structures are proven to have a natural tendency to be used in cylindrical designs or closed sections; while local buckling of cells is still expected, using of cylindrical structures might result in different result since the structure itself is self-stabilizing in that case. [24]

Another research had a more profound look at the effect of design parameters on the expected failure modes, the rib angle and ribs separation were fixed for this study, the rest of the parameters were varied including the length of the cylinder, which results in more or less cells in the structure. [26] They noticed five different failure modes (1) End delamination, (2) Material failure, (3) Local buckling, (4) Rib buckling, and (5) Global buckling; from which they created four failure maps covering the last four modes shown in Figure 2.8. The parameters are named as the following:

- $d_r$: Rib height
- $D$: Cylinder diameter
- $t_s$: Skin thickness
- $N$: Number of cells
- $t_r$: Rib thickness

A few conclusions can be made from this figure, some of which are intuitive. For example, for the same rib spacing, the wider the ribs, the later they buckle. Similarly, the thicker the skin, the later it buckles. As the diameter of the cylinder increases, failure mode transitions from skin buckling to rib buckling, and global buckling occurs only for large diameters or thin rib height. While these findings can be indeed correct, it is not clear whether rib-skin separation occurs or not and if it's even considered a failure mode. An argument can be made that this failure mode might be covered in the strength failure, since both ribs and skin are co-cured.

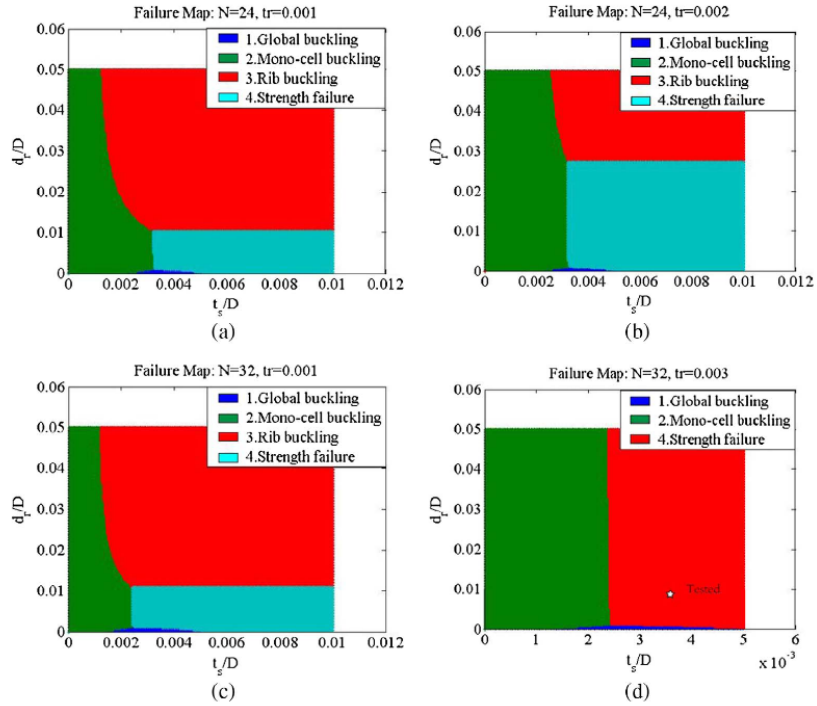


Figure 2.8: Failure maps of grid-stiffened cylinders

In addition, other researchers tested isogrid under different loading conditions and noticed similar failure modes, with the only difference being the sequence in which the modes occur and which are considered critical. For example, isogrid panels were tested under three-point bending, in one test the load was applied on the skin side and in the other it was applied on the ribs side. [20] In the test where the load was applied on the skin side, the specimen failed earlier where the skin-rib separation occurred earlier, followed by fiber breakage in the ribs. In the other test, the ribs failed first, followed by the skin-rib separation.

Finally, it was found that a limited number of researches were done to determine the strength of grid-stiffened structure after impact, out of which two are deemed relevant and discussed here. The first one, [37] had a limited number of specimens and impacted the specimen only at the cell area, which raises some doubts about the expected damage upon impacting the node. However, this research showed that impacting the grid-stiffened structure at the cell area does cause damage, but does not degrade the strength of the structure. Another one was found, [5] which had only one impacted specimen. For that one, the impacted specimen failed at around 60% of the ultimate load and away from the impact location, apart from the number of specimen, another limiting factor here is the way the specimen was impacted. Three impacts were done at different locations and different energy levels, this makes it difficult to determine which location and/or energy level had the most influence on the reduction in strength. For example, the node was impacted at a higher energy level than the skin, what will happen if it is the other way around? For specimens with cell skin, such an energy level might penetrate, in that case how would the grid-stiffened panel tolerate the damage? To best answer these question, it might be better to isolate the impacted specimens and test identical specimens with different impacting energies, in such case the results can be more conclusive.

## 2.6. Airworthiness Regulations

Safety of aviation is a vital concern since the very first flight; with the vast expansion in the aeronautics industry, many certification requirements were introduced by the airworthiness authorities to ensure the safety of any new aircraft. These requirements are often material-specific, meaning that a new set of rules needs to be introduced with the introduction of a new material, and so was the case with composites. The use of composites in aircraft has been increasing over the last few years, for new

aircraft types like Boeing 787 and Airbus A350, composites make up more than 50% of the materials used in the airplane.

Airplanes should have a damage-tolerant design, meaning that they should be able to tolerate damage by providing different load paths. This makes one of the most important regulations, which concerns the load carrying capacity of the structure after impact. During the operational life of any aircraft, random impacts are expected, these can vary from tool dropping during manufacturing or maintenance, to bird strikes and runway debris, which of course have different probabilities of occurrence and different severity. The different types of damages are categorized by EASA into five categories, as shown in Figure 2.9. [14]

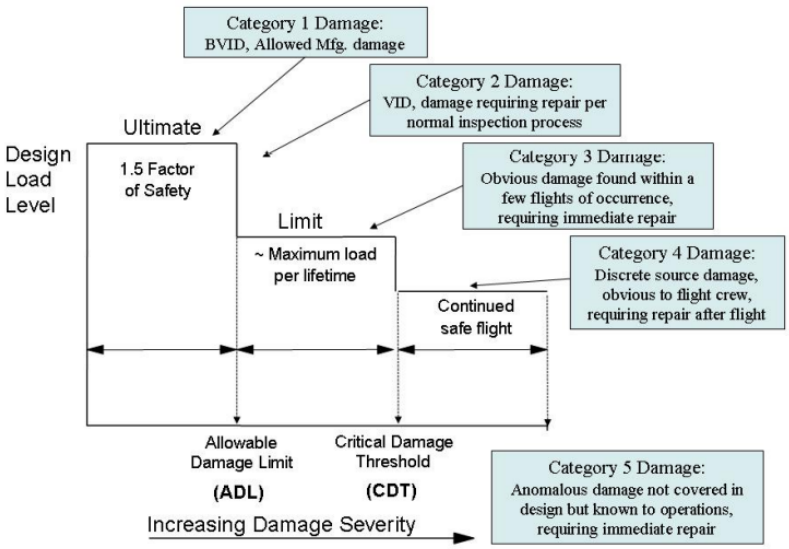


Figure 2.9: Schematic diagram showing design load levels versus categories of damage severity

The severity of the impact is described in terms of the amount of energy of the impactor and measured in Joules, hence, affected by both weight and velocity of it. Velocities, however, have a greater effect on the impact severity. [11] Consequently, based on the operational limits, the severity of the probable impacts can be expected. For example, small airplanes requiring low take-off speed will face less severe bird strike than airplanes requiring high take-off speed, and so on. As seen in Figure 2.9, categories three to five require immediate repair, they often caused by strong impacts such as bird strike. Consequently, categories one and two, barely visible impact damage and visible impact damage, are often the main concern when designing an aircraft. There is no one specific energy level at which Barely Visible Impact Damage (BVID) or Visible Impact Damage (VID) occur, it is rather material- and structure-specific. However, when a certain structure is designed, the energy level at which these damages occur should correspond to realistic scenarios expected during the operational life of the aircraft. Manufactures always determine threshold values for the impact energies based on the operational limits, from which they determine the cut-off energy level for this aircraft. For example, the cut-off value set by airbus for the A320 program is 50J. [12] For this project, a cut-off value of 30J is set by the manufacturer. That being said, very little to nothing was found in the literature about the performance of grid-stiffened structure after impact.

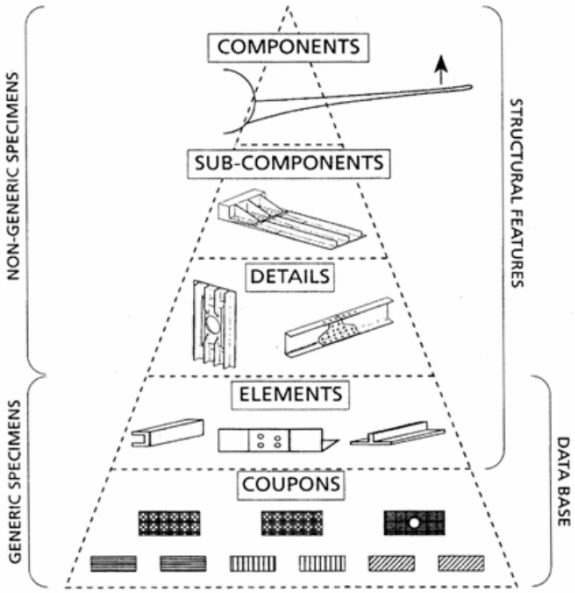


Figure 2.10: Schematic diagram of building block tests for fixed wing

That being said, aircraft manufacturers often follow the building block approach when designing a new aircraft, Figure 2.10. [14] Where they have to show the airworthiness authorities that their design complies with the regulations. Testing is often accompanied by analysis in such programs, where testing results have to comply with the analysis. That is particularly important for non-generic specimens, where testing gets expensive. On the other hand, testing coupons are generally cheaper to produce and test, and they could also be representative to the aircraft structure, the manufacturer should, however, show how these coupons correlate to the global structure. For impact testing, one does not always expect that all impacts at the same energy level result in the same damage. Hence, statistical distribution is sometimes necessary, meaning that many specimens are required. This makes coupons very handy for damage tolerance investigation of any new structure, where it becomes possible to produce large number of coupons and impact them at a relatively low cost.

By looking at the two figures presented in this section and the aforementioned discussion, a conclusion can be made regarding the necessary work to be done to show compliance of Nuuva V300 with regulations. Some specimens with the same design grid parameters should be impacted, both at BVID and VID, and loaded. It is important to have pristine specimen as well to calculate the drop in strength after impact. The exact type of loading will follow from the modelling, firstly, a global model with the provided loading conditions should be made. Then sub-models representing the testing specimens, which are used to validate the global model when validated with the test results. The selection of the BVID and VID for Nuuva V300 should be representative of real-life threat scenarios and comparable to the cut-off value set by the manufacturer. The test results should be as follows: the BVID specimen should be able to withstand the ultimate load, which is 1.5 times the limit load, and the VID should be able to withstand the limit load. It is important to note that such a testing program is very extensive. Hence, a simplified testing program might be followed for this thesis project.

## 2.7. Applicability of the results

Lastly, it is worth investigating whether the research output is applicable to other aircraft models or not. The decisive factor is whether there are other aircraft models that share the same specification and design requirements or not. These requirements can be summarized into the stiffness and strength requirements, and damage tolerance requirements, which can be concluded from the specifications of the aircraft. For example, two aircraft with different designs but have the same wing configuration, similar dimensions, same weight class, and perform similar operations (example regional jet), are likely to be facing the same loading conditions since they perform similar maneuvers; which will directly affect

the stiffness and strength requirements of the aircraft. And if their operational limits are similar, similar impact threats will be expected for both. One concern that arises in this comparison, however, is the failure mode. Depending on the design of the aircraft, the design failure mode might be stiffness-driven, or strength-driven. For the current fixed wing airplanes, however, this is not expected to be an issue due to most of the aircraft having similar design, a fixed main wing, tail wing, and vertical tail, which result in the same loading conditions, and consequently, it is highly likely that the same failure mode is designed for, as will be discussed below.

Hence, looking at the aircraft with similar specification can be a good start to investigate the applicability of the results. The specifications shall include the following: dimensions (length and wingspan), operational limits (this covers take-off speed, maximum speed, service ceiling, range, etc.), and masses (maximum takeoff weight and landing weight). With this information together with the aircraft configuration, one can draw a conclusion about how similar the loading conditions are. The configuration of the Nuuva V300 is different from conventional aircraft, with the two rods/beams connecting the front and rear wing, Figure 1.1, which should not affect much the loading conditions of the fuselage. For example, the fuselage upper section near the wing will still face compressive loading during flights due to lift force, and the lower part faces compressive loading on the ground due to the weight of the wings. Since the focus of this project will be on the aircraft fuselage, this claim can be deemed acceptable. It should be noted that for other unconventional designs, this claim might not be applicable, for example V-wing aircraft [15].

By looking at the dimensions and the weight of Nuuva V300, one can deduce that it is close to small or light aircraft weight categories, according to the FAA and ICAO, respectively. With the MTOW being 1700 kg, a length of 11.3 m, and average cruise speed of approximately 190 km/h. [35] An attempt was made to find a source gathering the database of all aircraft from the same category, which was difficult to find. Only a list with a limited number of aircraft was found, [1] Going through the list, many aircraft with similar properties could be found, which comes in the favor of this research, that the results can be generalized on a larger scale and not just applied to the reference aircraft. In the next phase of the project, a more detailed sample can be gathered, with the exact loading conditions obtained from the manufacturers' manuals.

## 2.8. Conclusion

In conclusion, grid-stiffened structures are proven to be a viable alternative to existing structures within the space industry, and a few researches briefly investigated using them for aircraft as well. But none of them studied in detail the design, manufacturing, and certification of a grid-stiffened structures for aeronautics applications.

To deem this structural concept feasible for aeronautics applications, it should be able to withstand the ultimate load after the occurrence of a BVID, and the limit load after VID, as per the aircraft certification regulations. The expected failure modes of the aircraft vary depending on the combination of grid parameters and loading cases. Hence, one can tailor the design to get the desired failure mode if needed. In addition, modelling of grid-stiffened structure is found to be very challenging, currently, most of the analytical models developed focus on predicting global buckling, and most researches focusing on manufacturing and testing just used existing FEM software programs. In addition, they used tape laying for manufacturing. Researches which went for automated manufacturing often used either filament winding or tow placement, with expandable rubber tooling. That being said, the following research question is formulated and broken down in to sub-questions:

- Are composite grid-stiffened structures a suitable alternative for current fuselage structures?
  - Are grid-stiffened structures able to provide a damage-tolerant design?
  - Will using grid-stiffened structures result in lighter aircraft structure?

To answer these questions, the project will include, design, modelling, manufacturing, and testing of a grid-stiffened structure. The detailed thesis planning is explained in the next subsection.

# 3

# Methodology

After formulating the research question, the first step was to refine the approach to followed to answer this research question. In this chapter, the method used, with its intermediate steps, are explained. In the first section, section 3.1, the approach is generally explained and the main work packages are listed. This is then followed by explaining the different work packages, modelling, manufacturing and testing, and results and conclusion, in section 3.2, section 3.3, and section 3.4, respectively. The last section discussed the project management and the timeline of the project, section 3.5.

## 3.1. Approach

In this chapter, the method followed to answer the aforementioned research question is explained. The first step towards evaluating the feasibility of using the GS structures for the drone application is to use an existing aircraft/drone model and replicate it using a grid-stiffened structure instead of the existing one. Then check whether the aircraft can still withstand the same loads. To deem the structural concept better than the existing one, it should not only be able to withstand the load, but it should be lighter as well. In the aerospace industry, mass saving translates to money. I.e., a weight saving of one kilogram should not cost more than a certain amount of money. Hence, a lighter structure should not cost more than the allocated budget per kilogram weight saving, neither the manufacturing nor the running cost. There are specific numbers for such trade-offs, but they are often confidential and difficult to get.

## 3.2. Modelling

A cost-effective way of doing so is by modelling the structure, then validating the model. This is done by manufacturing the structure and testing it, the test results should match the analysis results with a certain error margin. These errors should be explained by the model assumptions, known manufacturing defects, etc. For large structures, such as the drone fuselage in this study, it is not feasible to manufacture the entire structure to evaluate the structural concept. Hence, small test coupons are manufactured and tested; which should be representative to the global structure model. The first step is then to model the entire fuselage. The design parameters can be either chosen arbitrarily, and using trial and error one can reach to a lighter structure than the existing one. This approach, however, requires a very knowledgeable engineer with a good experience in the grid-stiffened structures.

Another approach is to start by sensitivity analysis, followed by an optimization, then the design parameters are selected. While this can result in a much better result, it is an intensive process which would take a long time to execute. One first starts with the sensitivity analysis, where for the given structure, the design parameters are varied. An assessment on how much the mechanical properties of the structure and its weight are affected by varying every design parameter is made. Based on which, one proceeds with an optimization process, where some iterations are done to select the optimal combination of parameters. This approach can be quite long. Hence, it is important to set certain limits when working, for example, time limit, select a limited design space based on the sensitivity analysis, etc. For this project, it was decided to go with the first approach, explained in the previous paragraph,

where the global model is made by one of the engineers in the team with proven record of experience, and further work is carried by the author. Hence, there are no plans for a full optimization process in this thesis, however, the approach to be followed in possible future developments is researched and presented in the thesis.

The other part of the modelling involves modelling of the test specimens. The test specimens are to have the same design parameters as the global model. However, to simplify the manufacturing process, flat specimens are made, which introduces error in the results, further discussion to follow on this point.

## 3.3. Manufacturing and testing

Once the design parameters are selected, the manufacturing of the test coupons can be started. This could start before having the specimens finite element models (FEM) ready, since there was enough time between the start of manufacturing and actually testing of specimens, example during curing cycles, material lead time, etc. The manufacturing is done in accordance with the techniques followed at ATG. First, two large panels are manufactured, out of which the specimens are cut. The specimens are then impacted. For the impact, fixtures had to be manufactured. It was intended to have the different types of damage, BVID and VID. The specimens with BVID should withstand the same ultimate load as the pristine specimens, which is 1.5 times the limit load. And the specimens with VID should withstand the limit load. After the impact, specimens were prepared for compression testing. Preparation included, potting, strain gauges, and DIC speckle application, this will be discussed in detail in chapter 5. Compression testing is then executed, the choice of the testing type was decided based on the global model.

## 3.4. Results and conclusion

To deem the use of grid-stiffened structure better for this application, different results should be achieved. First, the structure has to be lighter than the existing one. It should be able to withstand ultimate load with BVID and limit load with VID. Finally, the cost has to be comparable and within the allocated budget of the savings per kilogram set by the company. It should be noted, however, that the thesis focuses on the technical side of the project. Hence, cost analysis is not part of the work done.

These results conclude the thesis work, but they are preceded with a set of verification and validation activities. Verification is done throughout the process, for example, checking the dimensions are as intended, non-destructive testing, etc. Validation is done through comparing the model to the test results. The results should be closely compared, these results include the buckling load modes, buckling load, and failure load.

## 3.5. Project Management

### 3.5.1. Research plan for thesis project

The thesis work is done as part of a larger project within ATG Europe involving other team members and other external stakeholders, the thesis supervisor, industrial partner, and the European Space Agency (ESA). This means that part of the work in this thesis is either completed by other team members or a continuation of others' work, this was essential to have a reasonable amount of work to be done during the thesis period.

The project started by getting the technical information mentioned in chapter 1, understanding them, and analyzing them when required. This knowledge was then transferred to me upon joining the team, and the next step is to have a clear and well-defined approach. While this was done mainly by me, the other team members and supervisor have to be involved in the process. This means regular meetings took place with them. Following the definition of the research approach, the actual work starts. As mentioned earlier, it does involve modeling, manufacturing, and testing. Following that, a conclusion

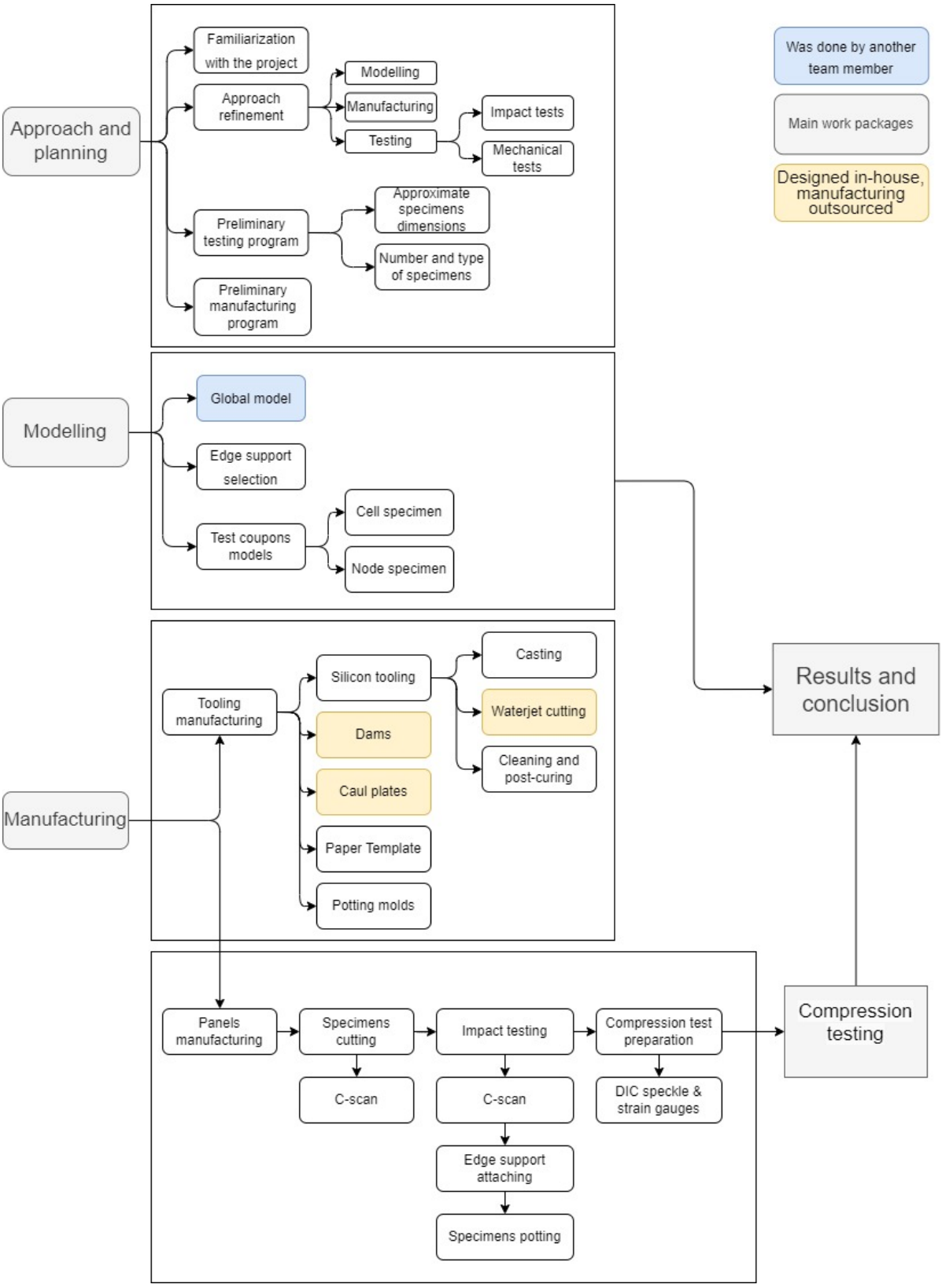


Figure 3.1: Methodology block diagram

can be drawn. Since the company uses a FEM software that I am not familiar with, some modelling work is expected to be done by another team member, where I was involved, giving inputs, requesting modifications, getting results and updates, etc. After the modelling part is done, the manufacturing took place. Manufacturing and testing was done at the TU Delft facilities, where I was the main responsible person. It is expected, however, that the existing manufacturing process method which was developed by ATG was used; hence, guidance was often provided by them. Afterward, testing was done. The testing program, including planning, instrumentation, and execution, was done by me in accordance with the work done previously by the different stakeholders. Furthermore, modelling of the test coupons were also be done by me. Then comes the conclusion and writing of the thesis. It should also be noted that technical reports and ESA deliverables were done by ATG and not part of the thesis work.

The thesis work can then be divided into work packages as follows:

**WP1 [February]**: The thesis work officially started in February. It started with familiarizing with the project, with the previous project work and with the project objectives. The kick-off meeting was done mid-February. It should also be noted that the literature study is to be worked on alongside the thesis and was not be submitted before starting working on the thesis. This was decided upon a discussion with the supervisor.

**WP2 [March-April]:** In March, the actual project work started. During March, the modeling approach was refined, that was done upon discussing it with the fellow engineers and with the thesis supervisor in a way that aligns with all the different stakeholders interests. Based on this, the following work packages can be started. It should also be noted that familiarizing with the software programs used by the company resulted in a slow-paced work in the beginning.

**WP3 [May-July]:** In these two months, the modeling part was done, together with the manufacturing and testing plan, which followed in the next work package. Thus, the plan was created in parallel with the modeling. The plan included the dates, the machines to be used, specimens sizes, list of required materials, ordering material, tooling manufacturing, etc. The midterm review is also planned after this work package.

**WP4 [August-November]:** During this period, the manufacturing, and testing were executed as planned earlier. This includes transporting the material to the lab, manufacturing, machining, non-destructive testing, specimen preparation (e.g., DIC paint and strain gauges bonding), testing preparation (e.g., machine reservation and fixtures manufacturing), and testing. This period might also be a good time to start documenting the previous findings, e.g., modeling results and approach.

**WP5 [November-December]:** November involved processing of the test data and the data from the numerical model and comparing them. This should result in answering the research question and concluding the thesis work. Alongside, the documentation of the thesis started as well. It should be noted that the green-light is planned somewhere during this work package period, this implies that the literature study was submitted and graded somewhere before the green-light followed by the first draft of the thesis.

**WP6 [December-January]:** During December, the final version of the thesis was submitted. Followed by the presentation preparation and finally, the defense.

# 4

# Modelling

In this chapter, the modeling work done throughout the project is explained. The discussion starts by briefly explaining the modeling approach in section 4.1, which will be followed by subsections explaining the respective work packages that took place. This starts with the global model in section 4.2, and test specimens models for both cell and node specimens, as explained in Figure 3.1, section 2.3.

## 4.1. Introduction

Throughout the thesis, Femap was the main modelling software used. It was used with Catia, which was used to create the CAD models. The CAD model for the current fuselage structure was provided by the manufacturer. This model included Bulkheads, stiffeners, and skin. The outer geometry of the fuselage of Nuuva V300 was obtained from that CAD model and used to create the new model. This was done by one of the fellow engineers in the team. A replica of the current structure, retaining the same geometry, was created using grid-stiffened structures. The model created was a parameterized model, which allows for easily changing the grid parameters. These parameters are: helical ribs angle, helical ribs separation, hoop ribs separation, rib height and width, and skin thickness, Figure 4.1. [40] Skin could also be omitted completely to have just a lattice structure if needed.

Then the next step was importing the new CAD file into Femap and starting the analysis preparation. The first step was to mesh the fuselage first, where a problem arises, since creating such a structure would be very tricky and time-consuming. The fuselage had only one plane of symmetry, meaning that one half of the fuselage had to be meshed manually completely. I.e., the mesh size along every single curve has to be defined, then the elements can be created for the different structural components separately since different layup and material properties are used; then this mesh can be mirrored around the plane of symmetry, and the coincident nodes are merged to have a continuous model. For a structure with more planes of symmetry, e.g., a cylinder, that is an easier process, where just one cell of the structure can be meshed, and then patterned to the entire cylinder. Hence, a solution for this

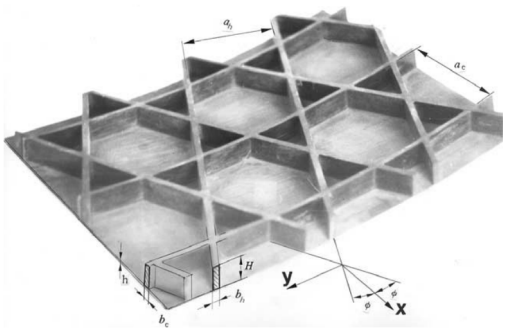


Figure 4.1: Variable design parameters in the CAD model

problem was proposed by one of the engineers in the team, which was a mesh projection script. This was a python script that projects a meshed cylinder to any closed-section structure of the same length and different cross-section. This saved much more time in the analysis, specially for the global and optimization models. And the modeling of the fuselage then started by meshing a cylinder. Meshing a cylinder could be done by meshing one two cells of the cylinder and then patterning them all around, and merging the coincidence nodes. The next step was then to run the script and get the mesh projected to the fuselage cross-section. This was then followed by defining the set of loads and constraints as provided by the industrial partner, setting up the analysis, and running the analysis. Shell elements were used for all the models created and explained below. Finally, it should be noted that, apart from the projection script and the global model, the rest of the work in this report was done by the author.

## 4.2. Global model

Next to using the CAD model provided by the manufacturer, other data was used in setting up the model. The most important was the loading conditions, the manufacturer provided different load cases. Only one was used in the analysis, which deemed to be the worst-case loading condition by the manufacturer. This loading condition occurs when the rear wing reaches the critical positive bending during the flight. No more information was provided regarding which maneuver causes the wing to reach the critical bending. Raw data was provided, for example, the aerodynamic loading as a function of the wing span. Since only the fuselage had to be modelled, this loading had to be integrated and the resultant load at the wing root was obtained. This was then applied at wing attachment points on the fuselage, this was the case for the front and rear wings. Other loads were also included in the model as per the worst case loading condition provided by the industrial partner, for example, the payload masses, which are on the floor attached to the fuselage. The floor itself was not included in the model, and the corresponding masses were applied on the floor attachments to the fuselage. The inputs provided included the payload masses with their corresponding centers of gravity (CG) and the attachment points of the floor to the fuselage. There were three main attachment points, and three payloads which happened to be of equal masses and equally distant. Hence, it was decided to apply these loads through three central nodes at the prescribed CG locations and transfer the load to the corresponding attachment location through RBE. A picture of the global model is shown in Figure 4.2.

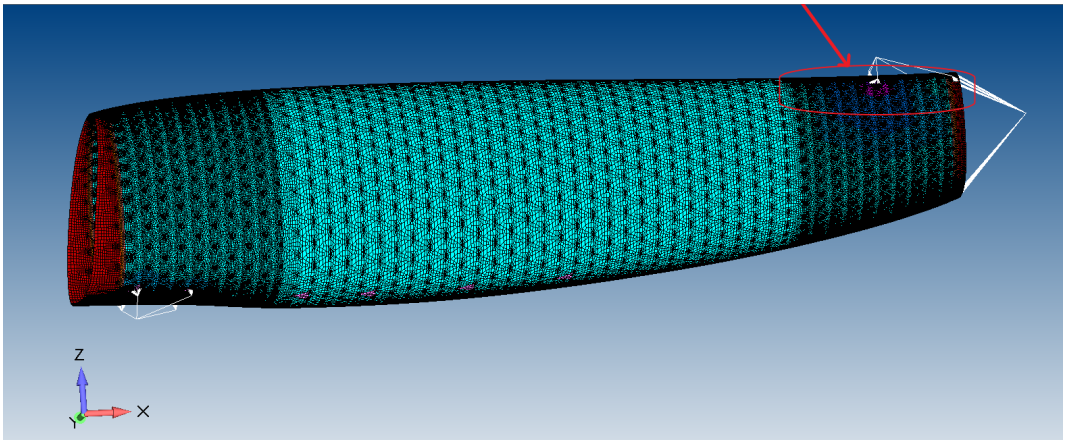


Figure 4.2: Global model

The darker sides of the model indicate a finer mesh, which were used in areas of attachments and/or high stresses. For the mid-section of the fuselage, that was not the case, and hence, it was decided to use a more coarse mesh for a faster analysis. The loads were applied using RBE2 elements, (Rigid Body Elements, type 2), where it is possible to specify independent degrees of freedom at a single point only, and their dependent degrees of freedom are specified at arbitrary points. This made it possible to have a single load application point, and get it transferred to the structure through RBEs. It was also possible to apply the load at the same locations as specified in the provided inputs. The red ends in

the model indicate the end laminates, pointed to in Figure 4.3, where the ribs terminate, and a thicker end of approximately the same thickness as the ribs is built. This part is important for connecting the fuselage to the rest of the structure. By looking at the design of the Nuuva V300, it can be seen that this is particularly needed due to the loading door in the front, and the propeller attachment at the end. These attachments can be done differently, and further optimization might yield in a lighter design. [25]

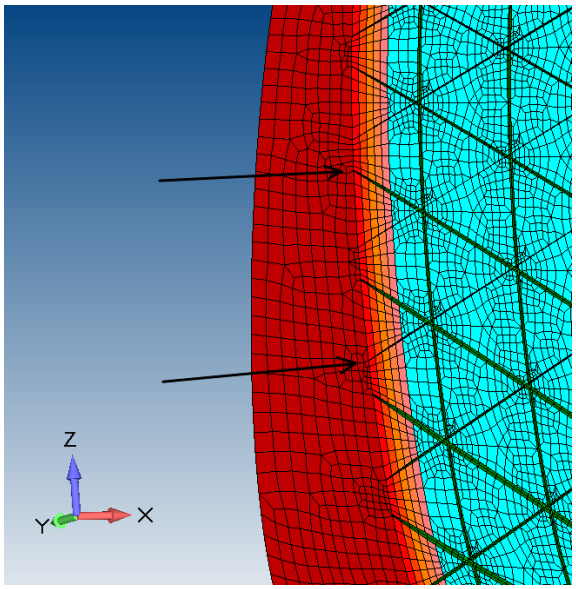


Figure 4.3: End laminates

The area with the courser mesh in the middle experienced the lowest failure indices, specially, the top part where no attachments or loads were applied directly. This area formed the largest part of the fuselage, which increases the probability of this area getting impacted compared to the probability of impact for the rest of the structure. In addition, due to the low stresses seen in this area and the absence of direct load application and attachments, no reinforcements were needed, and the skin thickness was minimum, only 3 plies. In the front and the rear, where the wings are attached, thick reinforcements in the attachments regions were added. This made these areas stronger compared to the middle part of the structure. Consequently, the expected resultant damage of the same impact is expected to be more severe in the mid-section of the fuselage, and the probability of damage impact is higher as well. Thus, the grid parameters in the mid-section of the fuselage were used for the test specimens. The highest failure index seen in this area was 0.6. In the testing, the ultimate strength of the specimen is considered, and hence, specimens reaching 0.6 of specimen strength already pass the test. In the later discussions, however, only the specimens' strength seen in the specimens models was considered. This implies that further optimization can be done, and lighter structure can be achieved, an optimization approach is presented in Appendix D. The mass of the fuselage using grid-stiffened structure added up to 75 kg, the achieved mass is competitive compared to the current solution.

The grid parameters in the mid-section, which were the ones used for the specimens and the rest of the models, were as follows:

Table 4.1: Design parameters

| Parameter | Value |
|---|---|
| Skin thickness | 0.84 mm |
| Skin layup | [70/-70/90] |
| Rib width | 3.5 mm |
| Rib height | 8 mm (16 UD plies) |
| Hoop ribs separation | 120.8 |
| Helical ribs separation | 117.3 |
| Helical ribs angle | 25.9 |

Finally, the critical loading condition occurred when the rear wings reached their maximum positive (upward) bending. This caused high compressive stress along the hoop direction in the rear wing vicinity. Hence, it was decided to perform compression tests for the test coupons.

## 4.3. Test specimens

In this section, the test-related modelling is explained. This starts with the explanation of the specimens' sizing, followed by the edge support design. The models for both cell and node specimens are then explained, and the predictions from the model are listed.

### 4.3.1. Specimens selection

The starting point of the manufacturing and testing campaign was to select the number of specimens and the size of specimens. As mentioned in chapter 2, for the aircraft to be certified, the structure should be able to withstand the ultimate load after the occurrence of BVID, and the limit load after the occurrence of VID. Hence, two types of specimens had to be tested, specimens with BVID and specimens with VID. In addition, pristine specimens had to be tested to obtain a reference specimen strength experimentally, and compare the impacted strength to it. This makes a total of three sets of specimens, BVID specimens, VID specimens, and Pristine specimen.

Secondly, the impact location had to be selected. It was decided to impact the specimens at two different locations, the middle of a cell, and the node. The main load carrying elements of grid-stiffened structures are the ribs. Hence, the cells can often be thin; which was the case for this structure as well, where the skin consisted of three plies only. This increases the probability of occurrence of visible damage upon impact. Thus, it was important to investigate what load could cause the intended damage and whether it comply with the probable real-life damage scenarios or not. The node is the location at which the ribs from three different directions meet, this makes it the stiffest part of the specimen. Damage occurring in the node will therefore result in damaging at least on rib, if not more. Hence, even though nodes form a much smaller percentage of the total surface area of the entire structure than cells, damage in a node could be much more critical than a cell.

To assess the effect of a single impact on the strength of the specimen, multiple impacts on one specimen should be avoided. This implies that, different two types of specimens had to be designed, cell specimens, where one impact targeting a cell in the specimen is performed, and node specimens, where one impact targeting a node in the specimen is performed. To account for manufacturing imperfections and possible difference between specimens, more than one specimen of each type had to be manufactured, e.g., multiple node specimens with BVID, multiple cell specimens with VID, etc. Three specimens of each type were tested, and one spare node specimen and spare cell specimens were manufactured. This made a total of 20 specimens, as shown in Table 4.2.

Table 4.2: Type and number of specimens manufactured

| Specimen type | Damage type | Number of specimens |
|---|---|---|
| Cell | Pristine | 3 |
| Cell | BVID | 3 |
| Cell | VID | 3 |
| Cell | Spare | 1 |
| Node | Pristine | 3 |
| Node | BVID | 3 |
| Node | VID | 3 |
| Node | Spare | 1 |
| | | **Total = 20** |

Finally, the dimensions of the specimens had to be selected. The first factor was the selected grid parameters, for example, for cell specimens, the cell has to include at least one complete cell; hence, changing the rib separation results in different specimen dimensions. Ideally, specimen shape has to be selected to minimize material waste during manufacturing, and in the case of this project; this was achievable only if the specimens are nested just next to each other as will be explained in subsection 5.1.1.

### 4.3.2. Selection of edge support

For the test coupons to be representative of the actual structure, they should properly mimic the behavior of the global structure upon applying a similar load. The test coupons used in this project are shown in Figure 4.4, further details about the sizing are explained in section 5.1. To limit the size of the test coupons, the skin at the edges is not supported, i.e., no ribs along the edges. The size of the cut cells at the edges is not negligible, and it was expected that the skin in these cells will buckle immaturely, which could affect the overall strength of the specimens. Hence, edge supports had to be used during the test.

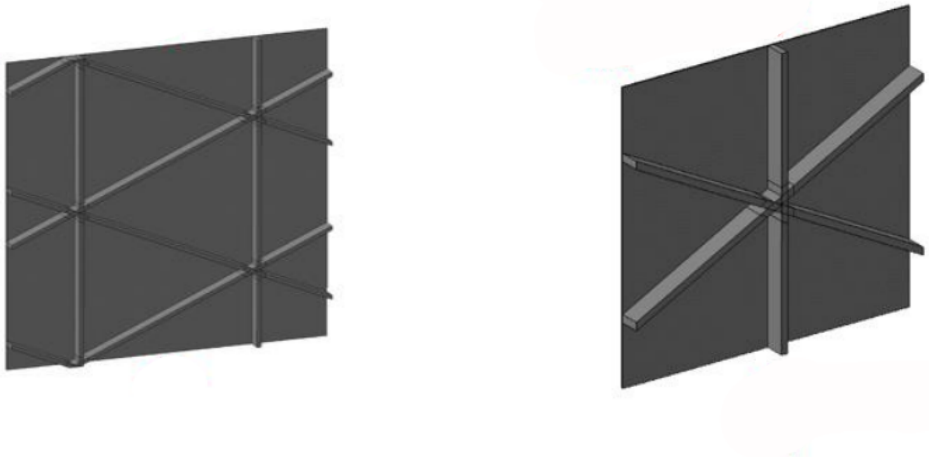

(a) Cell specimen (b) Node specimen

Figure 4.4: Test coupons

There were two ways of edges supports, either using a permanent support or a temporary support. The first one gets permanently fixed to all the specimens before the test, and depends on the way they are fixed, they might take up part of the applied load. This could be for example using an I-profile and attaching it to the edge. The other way is to use a frame on both sides of the specimen during the test to support the edge and prevent it from buckling. The frame is placed between the bottom and top plates with anti-buckling knives holding both edges, Figure 4.5 [36].

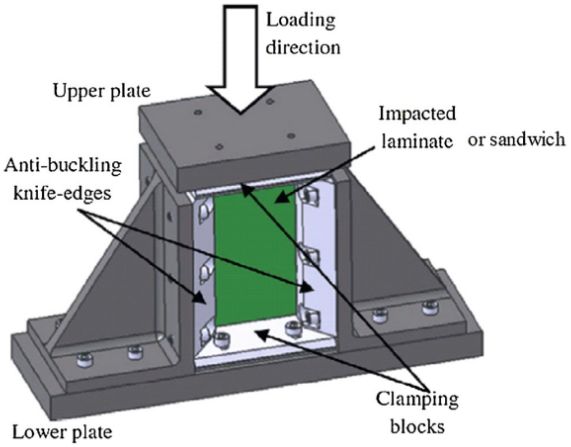


Figure 4.5: Support frame with anti-buckling knifes

One of the advantages of using the frame over the permanent edge supports is that, it does not take load, which in return affects the test results. The knives are straight, which means that they will be in contact with the skin side, and from the other side, they will be in contact with the ribs only. Leaving a space which is equal to the rib height between the knives and the skin, which would be enough for the skin to buckle near the edge. To use such a setup, a modified design has to be created. In addition, using such a setup means that the frame has to be assembled and disassembled with every single test. Since there were 20 test coupons for this project, this would have been time-consuming.

It was decided to go for the other option, which is to have permanent edge supports glued to the edges. This included some modelling to select the proper dimensions. In addition, they had to be bought off-shelf, cut into size, machined and glued. While this was also time-consuming, it allowed for much quicker testing, which was important due to the limited availability of the testing machine. The approach was to select an I-profile that is readily available in the market to save manufacturing time. Hence, the first step was to have a list of the available profiles in the nearby shops. A few iterations were to be done to choose the support dimensions and how they are glued to the specimens. Three approaches were selected to choose from, the first one is to have the profiles running along the entire length of the specimen, hence going through the potting from both sides (approach 1). Secondly, is to have them going through the potting from one side and terminating before the start of the potting block on the other side (approach 2). The third was to have the support running between the two potting blocks and terminated just before the blocks (approach 3).

The goal was to have the support preventing the edge from buckling and not increasing the strength and stiffness of the specimen by a large percentage. Hence, a preliminary analysis was done to select the most suitable approach out of the three presented ones. To simplify the analysis, the potting was not included, only the area of the specimen between the two potting blocks. The potting was assumed to be rigid and transfers the applied load to the specimen. Hence, the load was applied on the top edge of the specimen through a RBE to all the nodes on the interface, the nodes on the interface were connected to a center node where the load was applied. The top and bottom edges were pinned, and the top edges were only allowed to translate vertically. That was done to mimic the test situation, since the machine applies load on the top edge only and the bottom is fixed, Figure 4.6.

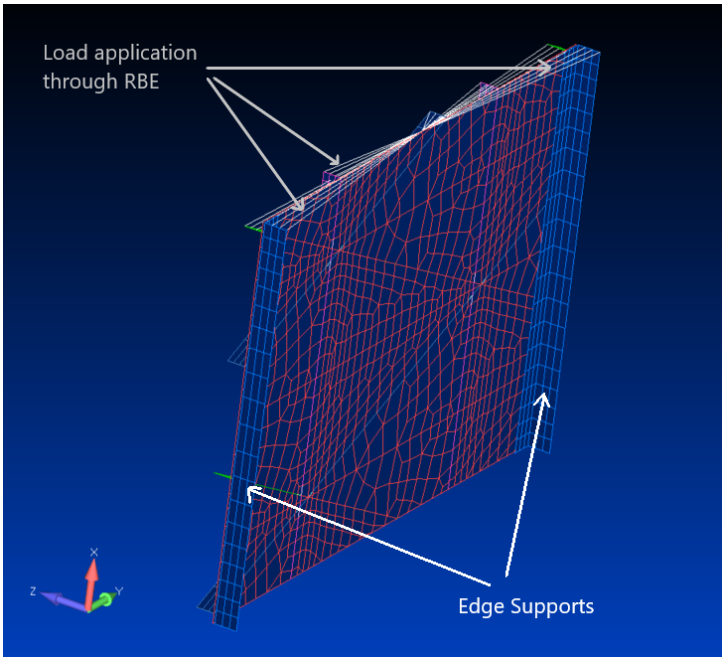


Figure 4.6: Edge support analysis

To save time on the analysis, the three approaches were tried using the same model. This was done by changing the load application region and the constraints as follows for the three approaches respectively:

1. The nodes of the top side of the support were connected to the load application node through RBE, and the nodes on the bottom side had the same constraints as the specimen edge.
2. The nodes of the top side of the support were connected to the load application node through RBE, and the nodes on the bottom side were not constrained. It should be noted that this approach was tried in two different ways, first, as explained, and second by not applying loads on the top side and constraining the bottom side instead.
3. Neither the nodes on the top side of the edges were connected to the RBE, nor the bottom nodes were constrained.

The edges were connected to the specimens using glue connection with the adhesive properties, with the specimen elements being the master elements and the profile elements being the slave elements. To compare between the three different approaches, the same profile was used, same load applied, and same analysis setup. In terms of buckling prevention, they all worked as intended, and the next step was the sizing of the profile itself, hence, the main goal of the comparison was to see how much does the approach affect the strength. It was found that the first one affect the strength the most, where approximately 60% of the laminate failure index without the support was reached for a linear static analysis, and the third option had the least effect with around 97% of the laminate failure index was reached. Hence, it was decided to proceed with the sizing for the third approach. However, it had the risk of the profiles flying off during the test in case of large out-of-plane deformations, for which a non-linear analysis was done later after sizing to see likelihood of this happening.

The approach was to start by the smaller to the larger profile, focusing on the ones with the simplest geometry. Different geometries were available off-shelf, which included closed sections, c-profiles, z-profiles, and l-profiles. They all had a minimum thickness of 1 mm. It was decided to start with the l-profile because it had the simplest geometry among the existing ones. The l-profiles had minimum dimensions of 10 mm x 10 mm x 1 mm, and next bigger one had dimensions of 15 mm x 15 mm x 1.5 mm, etc. The smallest one was first used in the analysis.

Using the 10 mm profile did not affect the strength of the specimen, but the buckling was sufficiently shifted towards the center of the cell and the buckling load increased by at the edge cell by 12%. The highest out-of-plane deformation occurred at the first buckling mode in the edge cell was also lower by approximately 25%. While the buckling load was not really of high importance, it was important to have local buckling within the cell rather than global buckling and minimize the magnitude of the out-of-plane deformation. That was further validated after the test due to the failure mode seen, more details will follow in chapter 6. Using the support, both of the goals were achieved. However, due to the thin skin and relatively large cell area, buckling still occurred at approximately 20% of the failure load.

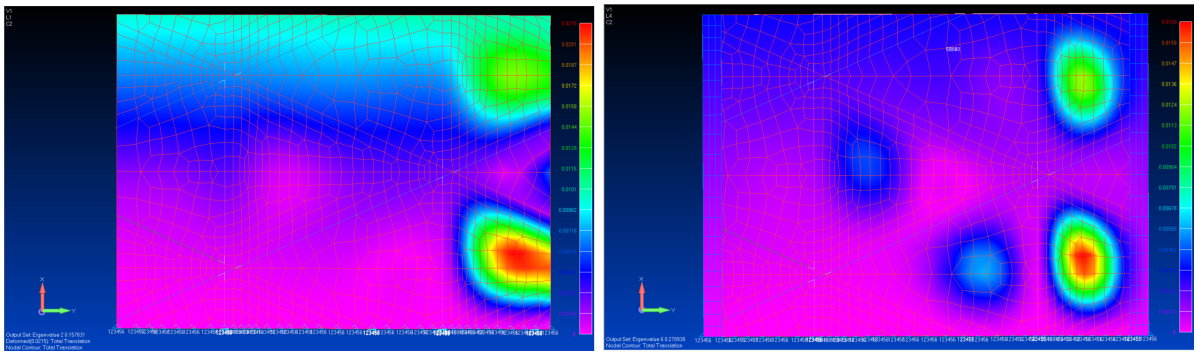

(a) No edge support (b) 10 mm edge support

Figure 4.7: Buckling analysis with and without edge support

The same analysis was done for the 15 mm profile, but it was noticed that the strength of the specimen increased by 5%. The buckling of the outer cell was again pushed away from the edge, and it occurred at a higher load than for the 10 mm, approximately 4% higher. Hence, it was decided to not proceed with the rest of the profiles and the 10 mm profile was selected. In addition, to avoid high stresses in the region where the profile terminates, the end of the profile was tapered, Figure 4.8. Finally, the analysis to select the edge support was done only for the cell specimen and upon the choice, a similar analysis was run for the node specimen with the selected profile. The reason was that the cell specimens had larger cell areas near the edge, which means buckling would be expected earlier and more critical in the cell specimens. That was deemed indeed true after running the analysis with the node specimen and from the test results.

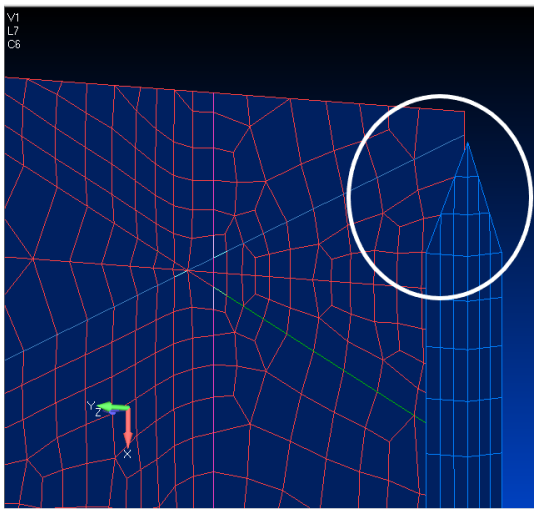


Figure 4.8: Tapered end of the support profile

### 4.3.3. Cell specimens

The setup of the specimens models was done similarly as explained in the previous two sections. The effective area of the specimen was only included in the model, that is the area between the two potting blocks. The load was applied on a central node connected to the nodes on the top side of the specimen through rigid body elements. The nodes on the bottom side of the specimen were fixed, and the nodes on the top side were allowed to move vertically only. This assumes that potting compound to be rigid. In reality, this would not be the case, and the nodes would be expected to rotate. However, this would not be a free rotation but small rotations; hence, it is not also possible to use pin constraints for these nodes. A workaround was done in order to more accurately model the effective area of the specimen, which is to extend the length by five millimeters. This value can be validated through sensitivity analysis, i.e., how do results change with changing this value. That way, the fixed nodes correspond to nodes inside the potting, and approximately near the actual interface, nodes were able to rotate. This comes with the fact that these nodes are not fully pinned, but can also slightly translate. A more accurate way to model the specimen would be to include the potting compound, but this will require either a full solid model, or have an interface between the solid resin blocks and the shell elements of the specimen, which add to the complexity of the model. To account for the bending in the specimen that occurred during curing, a thermal analysis was first done, and the deformation of the nodes from this analysis was used to deform the existing model to have a bent pre-deformed shape, the specimen model is shown in Figure 4.9 and the top view showing the bending in Figure 4.10.

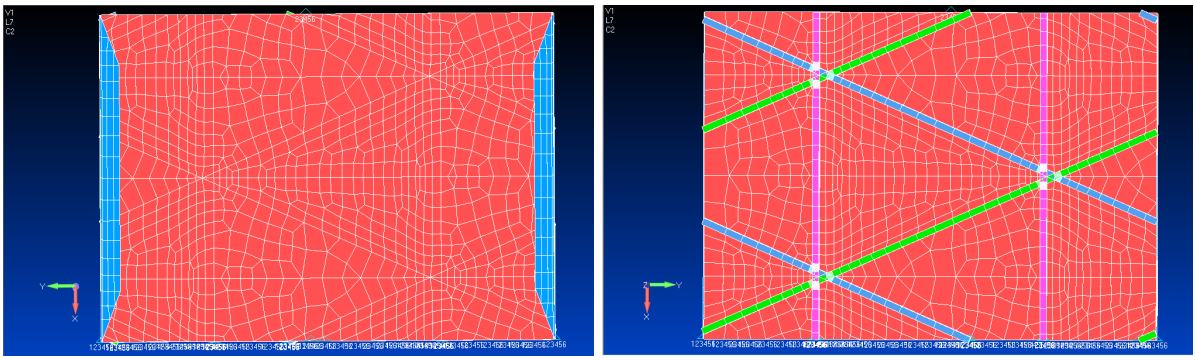

(a) Skin side (b) Grid side

Figure 4.9: Cell specimen model

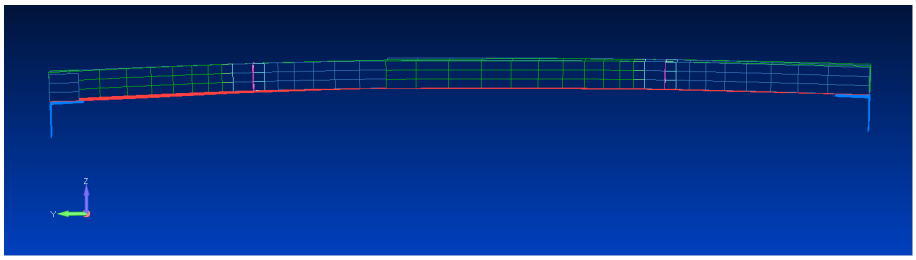

Figure 4.10: Modelled bending in the cell specimen model

Although solid elements would have been more accurate, shell elements were used. This is due to the added complexity of setting up a solid model for grid-stiffened structures. Hence, it was decided to use shell elements for this project due to the time constraints. The Aluminum profiles were added to the model by defining connections between the two corresponding faces of the profile and the skin, respectively.

The specimen models were intended to predict the actual specimen behavior during the testing. Hence, extra attention was paid for the setup of the analysis. Different types of analysis were run in this model.

Linear static analysis, buckling analysis, and non-linear static analysis. Initially, the static analysis and buckling analysis were run. From the buckling analysis, it was seen that buckling occurred quite early resulting in relatively large out-of-plane deformations, which can be considered a type of geometric non-linearity. It was then decided to set and run a non-linear static analysis in order to better predict the failure loads. For this analysis, the Full Newton-Raphson method was used by the solved. A couple of failure criteria were available to use in FEMAP, this included both non-interactive criteria such as maximum strain, and interactive criteria such as Tsai-Wu. For the level of complexity of the grid-stiffened structure, it is more common to use interactive failure criteria, due to the higher chance of different stress types interacting. [38, 37, 22]. Hence, it was decided to use Tsai-Wu failure theory. A major disadvantage of this criterion, however, is that it cannot identify the failure mode despite it is ability to accurately predict the failure load in numerous instances. Other failure criteria such as Puck's and Hashin's can do so, however, they are more difficult to implement and were not available to use in FEMAP.

### 4.3.4. Node specimens

The model of the node specimen and the analysis were set up in the same manner as the cell specimen model. With the only difference being the specimen geometry, the specimen model is shown in Figure 4.11 and the top view showing the bending in Figure 4.12.

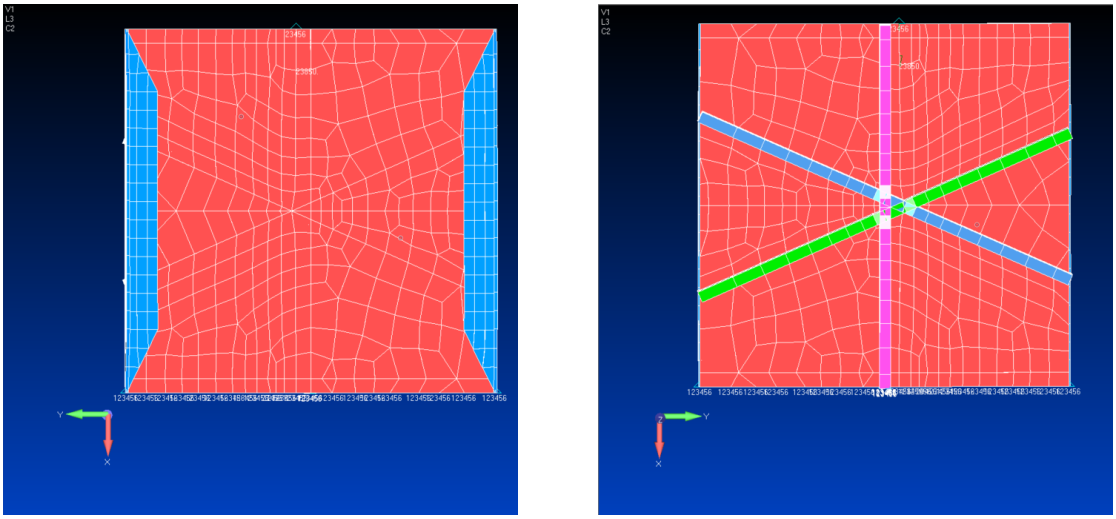

(a) Skin side (b) Grid side

Figure 4.11: Cell specimen model

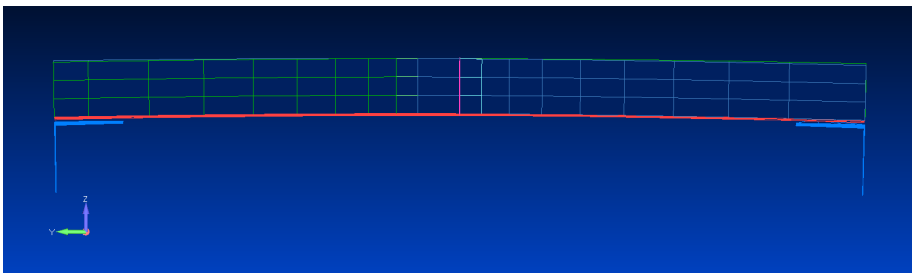

Figure 4.12: Modelled bending in the node specimen model

### 4.3.5. Predictions

From the buckling analysis, the first eigenvalue was used to determine the load at which the specimen starts buckling. This was later compared to the DIC images, and the load at which buckling was firstly

noticed is compared to the buckling load of the first eigenvalue. The model predictions are listed in Table 4.3 for both cell and node specimens. The failure loads listed in the table are the loads at which the failure index of 1 was observed in the model. In reality, once this is reached, the specimen does not necessarily fail completely, it might be able to still carry load. Hence, to compare the experimental results with the model, the ultimate strength of the specimens is defined to be the maximum load reached by the specimen. This is determined by the failure mode of the specimen; for example, if after reaching the ultimate strength the ribs break, the specimen will likely not be able to carry any further load, or a small percentage of the ultimate load. Another mode found in the literature is skin-rib separation, in which case, the rib and skin separate after the specimen reaches the ultimate load, but the ribs still can carry considerable amount of load compared to the maximum strength. In this case, to compare experimental results to the model, the load at which the skin and ribs separate is considered to be the failure load.

Table 4.3: Model predictions

| Specimen | Buckling load [kN] | Failure load [kN] |
|---|---|---|
| **Cell** | 9.9 | 41.0 |
| **Node** | 13.7 | 23.8 |

# 5

# Manufacturing and Testing

In this chapter, the manufacturing and testing procedure are explained. The first section, section 5.1 describes all the manufacturing steps, this includes tooling manufacturing, material used, curing cycles. After manufacturing, the specimens are impacted, the impact test setup is discussed in section 5.2. Specimens are then prepared for compression testing, the test preparation is discussed in section 5.3. The testing program and setup is then explained in section 5.4.

## 5.1. Manufacturing

As previously mentioned in section 4.3, the testing program includes manufacturing of 20 test coupons, which are divided into 10 Node specimens and 10 Cell specimens. There are two ways of manufacturing these specimens, either to manufacture 20 separate specimens, or to manufacture a large panel and cut it into small specimens with the required specimens sizes. The first option implies that either 20 sets of tooling are required to manufacture all the specimen, or one set that is used repeatedly to manufacture all the specimen, which would have been very time-consuming and inefficient; since for every specimen numerous steps are involved including using the autoclave, which consumes a lot of energy. For the second option, manufacturing of large panel(s), size constraints need to be considered. I.e. One large panel including all the 20 specimens can be too large for hand layup by one person, or might have larger dimensions than the manufacturing facilities, e.g., layup tables, autoclave, cutting machine, etc. A trade-off can result in an intermediate solution between the two proposed options, for instance, manufacturing of multiple large panels and cut them into the specimen's size.

A problem that might arise from cutting the panel is, the damage to the fibers along the cutting line or the possibility of delamination near the edge if too much force is applied by the cutting blade, or the blade is not sharp enough. For the hand layup of the GS structures, the edges are often of low quality, meaning that, even if the specimens are manufactured separately, a strip will need to be cut near the edge from the four edges of the specimen. Hence, the possibilities of machining defects are omitted as a trade-off criterion, since it would be expected in either methods.

### 5.1.1. Specimens nesting

Based on this comparison of the two methods proposed, it was decided to manufacture a large panel(s) and cut them into size, considering the manufacturability of the panel and the size constraints from the machines used. There are, however, infinite ways of nesting the specimens into one or more large panels. For instance, should there be one panel for Node specimens and Cell specimens? Should they be mixed into identical panels? What should be the size of the panels? And so on. To arrive to the final dimensions, a few decisions had to be made. Firstly, it was decided that the maximum panel dimensions to be handled by one person should be approximately 1 m by 1 m. This estimate is not precise, it is rather based on rationale and a few trials in the lab to see what would be the maximum layup area that can be done by one person without hindering the layup quality anywhere in the panel. This means that a few centimeters more or less can be acceptable as well. The machine size constraint

came next, the decisive factor in this was the autoclave size. The maximum baseplate size that can fit in the autoclave at the university laboratory is 1020 mm by 1700 mm. Considering the space needed on the plate edges for tooling, e.g., vacuum bag seal, steel dams, etc., the maximum GS panel width is actually less than 1020 mm. The space needed on the edges is estimated by a minimum of 50 mm on each edge. For the other dimension, the 1700 mm is way more than the previously set maximum anyway. Hence, the maximum panel size is approximately 900 mm by 1000 mm.

Finally, the specimens should not be cut from the edges of the panel, meaning the area near the edge of the panel is scrapped; which should be accounted for in the nesting. Based on this and on the specimen sizes, the first iteration showed that it is not possible to have just one panel for all the specimens. A second iteration showed that it is not possible to have one panel for all the Cell specimens. Thus, some cell specimens will have to be cut from the other panel. After a couple of iterations, it was decided to manufacture two identical square panels with identical nesting pattern. This makes it easier in terms of tooling design and manufacturing. In addition, the learning curve helps with the second panel, meaning that less time is expected for the manufacturing and the cutting of the second panel. The size of each panel is 856 mm by 856 mm, the nesting is shown in Figure 5.1, where the rectangles correspond to cell specimens and the white specimens correspond to the node specimens. The gray areas on the edges are the silicone tooling and the dams, and the red lines represent the cutting lines and the areas enclosed by these lines represent the specimens.

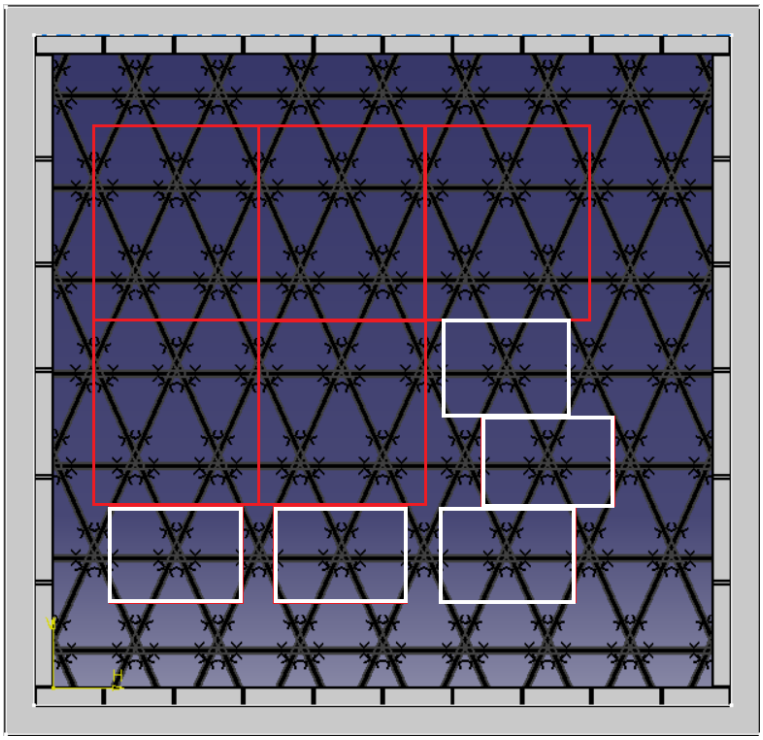

Figure 5.1: Specimens nesting

### 5.1.2. Manufacturing technique

Among the different methods of manufacturing CFRP panels are wet layup, resin infusion and prepreg hand layup. For this project, prepregs are used. This omits the steps involved with mixing resin, pouring it, using infusion mesh, etc. It also ensures an optimal fiber volume fraction and reduces the chance of dry spots and/or inconsistent volume fraction along the panel. In addition, the use of prepreg is very convenient when it comes to tape laying, which is how the ribs are manufactured. If wet layup is used, one has to either impregnate the fibers then cut them, or cut them then impregnate them. Either way, cutting the ribs' width which is 6.3 mm when uncured is very tricky with loose fibers and increases the chance of error a lot. Hence, prepreg was ideal for this application. That being said, the manufacturing steps will be explained in this subsection.

#### 5.1.2.1. Tooling preparation

In this section, the tooling used is explained. This includes both, technique-specific tooling and general tooling required.

- **Baseplate:** The first step is to prepare the baseplate, on which the laying up process will be done. The plate used had larger dimensions than the panel to be manufactured to allow for all the tooling to be placed. To minimize flexures during curing cycles and while moving the panel, the plate has to be fully flat and as rigid as possible within the reasonable mass constraints. Hence, a thick aluminum plate is used with dimensions of 1000 mm by 1500 mm, Figure 5.4. This plate was not custom-made or bought for the project, but off-the-shelf plate from the lab. Thus, it was used previously and proper cleaning of the plate is required. Acetone was used to clean it and remove excess resin from the previous curing cycle. Then a layer of release film was taped to the plate. It should be noted that the material used during the manufacturing process were able to withstand the maximum curing temperatures, which will be discussed later.
- **Paper template:** After the release film is added, a paper template is used as a guidance for tape laying. The pattern, angles, and dimensions of the drawing on the template correspond to those of the ribs. Small triangular vertices are added near the nodes to guide when placing the prepreg tape, as shown in Figure 5.2. The rectangular blocks on the edges represent the silicone tooling to be added. The paper is taped on the first release film layer and another layer is then added on the top of the template. The panel is then ready to start the layup.

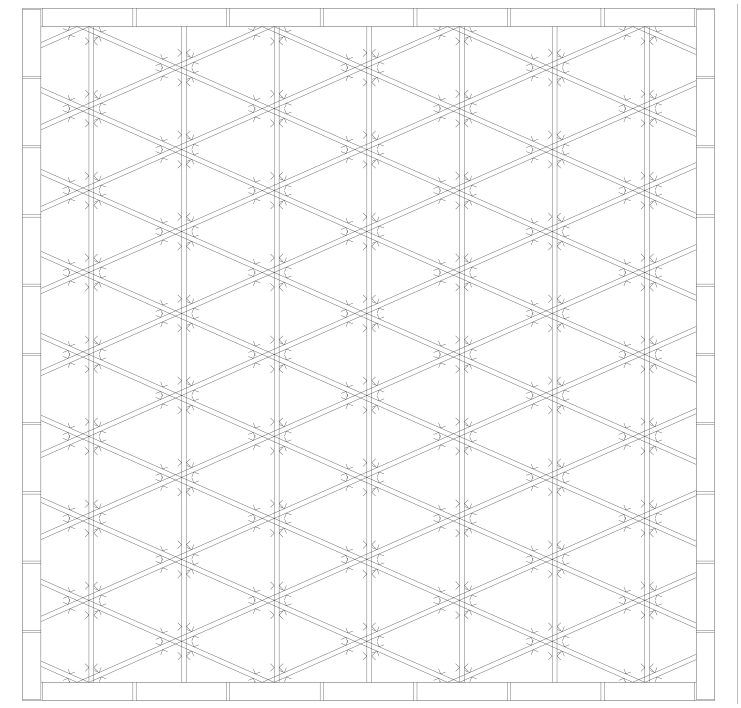

Figure 5.2: Paper template

- **Dams:** The dams are steel rods with rectangular cross-section. They are bolted together to form the edges of the panel. They act as rigid walls during de-bulking and curing to prevent the silicone tooling from unnecessary expansion, consequently preventing distorting the shape or the dimensions of the panel, dams are shown in Figure 5.7 and Figure 5.4.
- **silicone tooling:** During the de-bulking and curing cycles, the fibers face high pressure, which will easily distort the ribs and flatten them. Hence, something needs to fill in the cells areas to prevent this from happening. For this purpose, silicone blocks are manufactured with a slightly smaller

dimensions to the pre-cured dimensions of the cells. During curing, these blocks expand exerting pressure on the ribs resulting in different dimensions. The sizing was based on a thermal model that was previously done at ATG; however, it is not part of this thesis and will not be discussed further. The number of blocks was equal to the total number of cells in the two panels, including the incomplete blocks along the edges, plus 10% margin to account for possible waste. The process of manufacturing these blocks is as following:

1. Mold preparation and cleaning. The mold consisted of two halves made of aluminum plates which are closed after pouring of the silicone material. These halves were fully flat rectangular plates, with plastic edges attached on one of them in which the liquid silicone is poured. The thickness of the silicone panel is determined by these edges. They can be 3D-printed with the required thickness. In the top side of the plastic edges, a groove is made for excess silicone material that comes out after closing the mold, Figure 5.3 [1]. Two-components silicone material is mixed in a large bucket, then put in a degassing chamber to get out trapped air.
2. The silicone is then poured into a mold and the mold is closed. The mold is left until the silicone is cured.
3. The silicone panels are then brought to a water-jet cutting company to cut them into the right size.
4. The blocks come out of the cleaning process dirty and full of dust. They are then cleaned with Ethanol and dried.
5. For the material to reach the properties listed by the manufacturer, it has to go to a post-curing cycle. The blocks are put in the oven at $180^oC$ for three hours. The silicone blocks are then ready to be used for the GS panel manufacturing process.

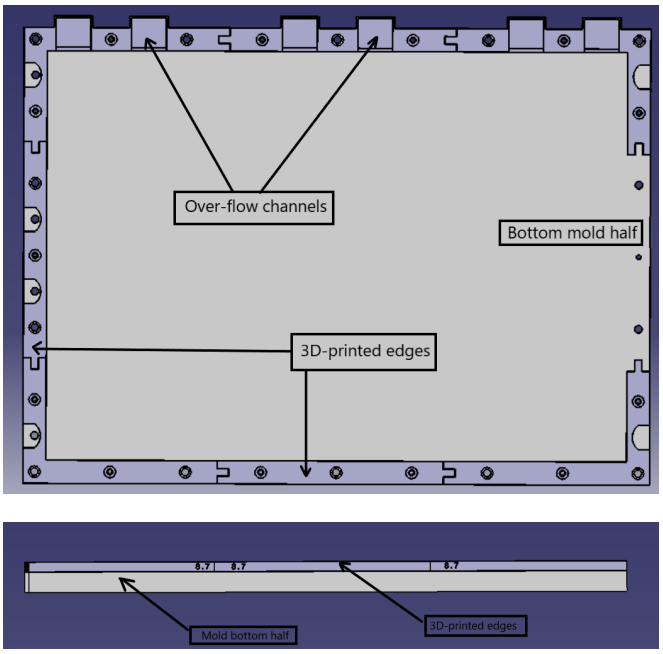


Figure 5.3: Silicone mold, top and front views

- **Caul plate:** These are aluminum plates with a thickness of 5 mm, they are added on the top of the skin during curing and on the top of the ribs during de-bulking, Figure 5.4. This ensures a flat surface when the panel is under high pressure. The dimensions of the Caul plate are determined by the dimensions of the GS panel and the rectangular silicone blocks on the edge, such that the

[1] Mold is designed and manufactured by ATG

plate fits exactly in between the dams. The plate is made slightly smaller to allow for easy adding and removal.

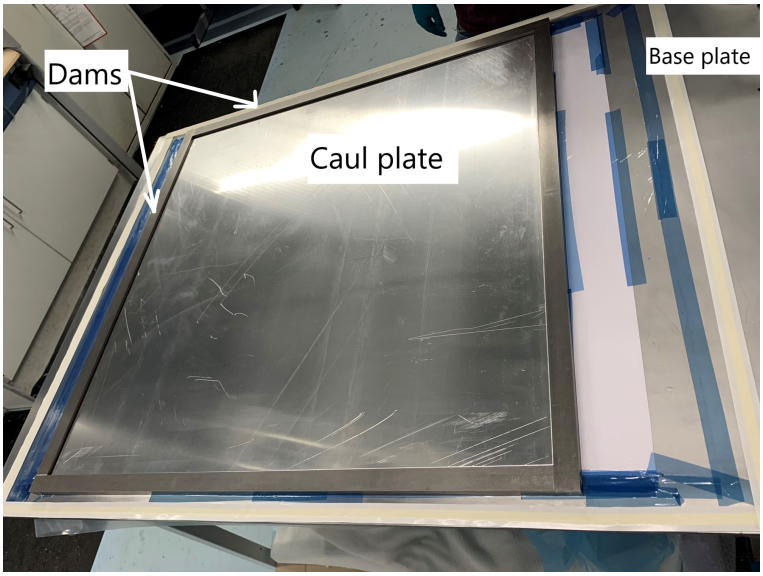


Figure 5.4: Manufacturing tooling: Caul plate, dams, and baseplate

- **CFRP general tooling**:
  - Tape
  - Breeder
  - Vacuum bag
  - Tacky tape
  - Vacuum pump
  - Vacuum valve
  - Release film

#### 5.1.2.2. Layup process

The layup process starts by getting the prepreg rolls out of the freezer and leaving them until they defrost. It was split into two steps, first layup of the ribs, i.e., tape laying, then skin layup. To reach the required thickness of the ribs, 16 layers of tape had to be added. It was not always possible to add all the 16 layers in one day. Hence, the layup took more than one day most of the time. That was acceptable, since the out-of-freezer curing time was more than this, meaning that the prepreg still has some of its tackiness over the layup period. During the tape laying, the following rules were important to follow:

- The tape has to go precisely over the allocated region for it.
- One layer is added at a time for all the three ribs dimensions and same order follows for all the layer. I.e., if one started by the positive helical, the negative helical, then the hoop rib, for the first ply, the same order should be followed in the subsequent plies.
- The tape is stretched between the nodes to minimize waviness of the fibers, see Figure 5.5.
- A maximum of two overlapping directions is allowed at the node, which prevents overly dense regions at the node. This results in all the three fibers directions round a center point in the node.

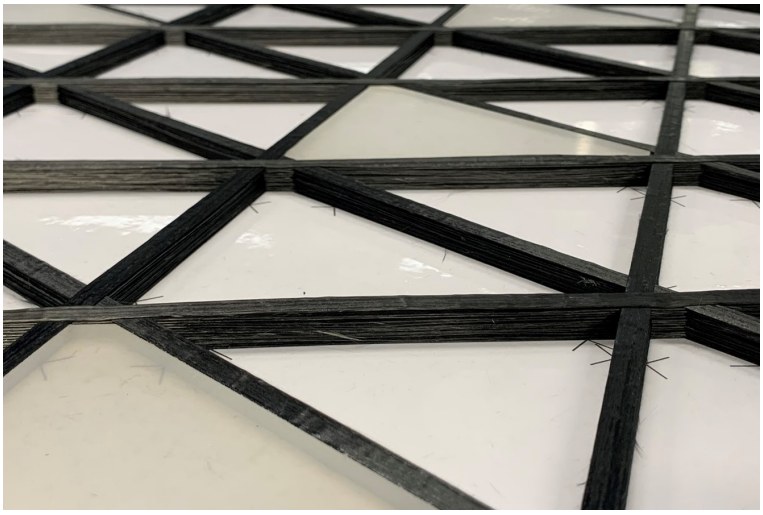

Figure 5.5: Stretched tape between nodes

In case the layup has not yet been completed, a layer of release film is placed on the fibers until the next day to prevent contamination and dust inclusions. When all the 16 layers of the ribs are added, the silicone blocks are added in place. Next to the blocks in the cells, a set of rectangular blocks are also added between the GS panel and the dams, Figure 5.6. The next step is de-bulking which is essential for the compaction of the plies. A layer of release film is added, the Caul plate is placed, a layer of breeder is placed over the panel and the dams, the tacky tape is used to seal the vacuum bag over the panel, and the pump is connected to this setup. The pump is then turned on and left overnight. The skin plies are cut into the right dimensions from a large prepreg roll, the pump is turned off, and the vacuum bag is removed. First, before adding the skin, the set of rectangular blocks on the edge is changed with a thicker set of blocks. That is because of the increment of the total thickness of the panel after adding the skin. Hence, the new set of blocks equals the thickness of the old set of blocks plus the thickness of the skin. After changing the silicone blocks on the edge, the skin plies are added. The skin is three layers only, this does not require a long time to add, meaning that the skin layup was always done in one go.

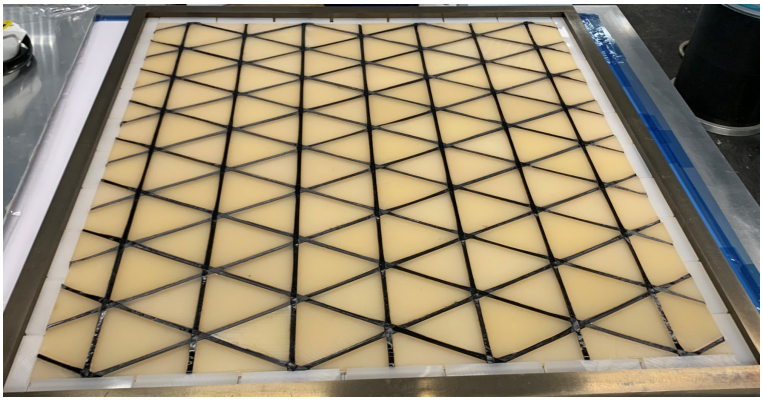

Figure 5.6: Complete ribs layup plus silicone tooling

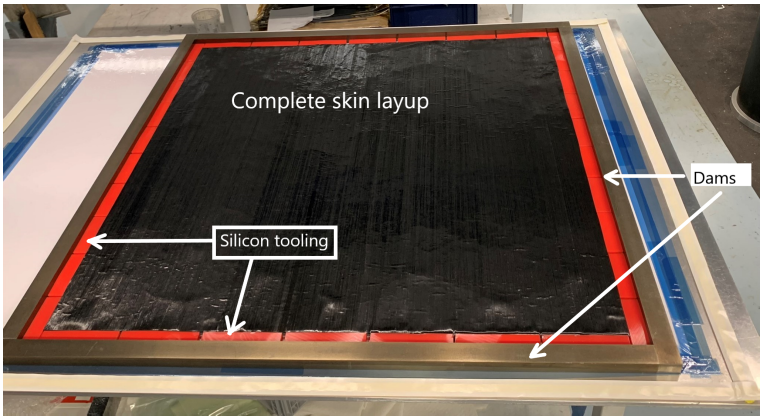


Figure 5.7: Complete layup

The next step is then preparing the panel for curing. This starts by adding three layers of release agent on the Caul plate. Release agent is also added on the dams just in case resin overflowing to them during the curing cycles. The vacuum bag is added again, and the setup is left for de-bulking for a couple of hours before the start of the curing cycle.

#### 5.1.2.3. Curing

Following de-bulking, a leak test is done to ensure that the bag is sealed properly and no pressure drops will occur while moving the panel to the autoclave and during curing. If the test succeeded, the pump is disconnected, and the panel is taken to the autoclave. The complete setup with vacuum bag in the autoclave is shown in Figure 5.8.

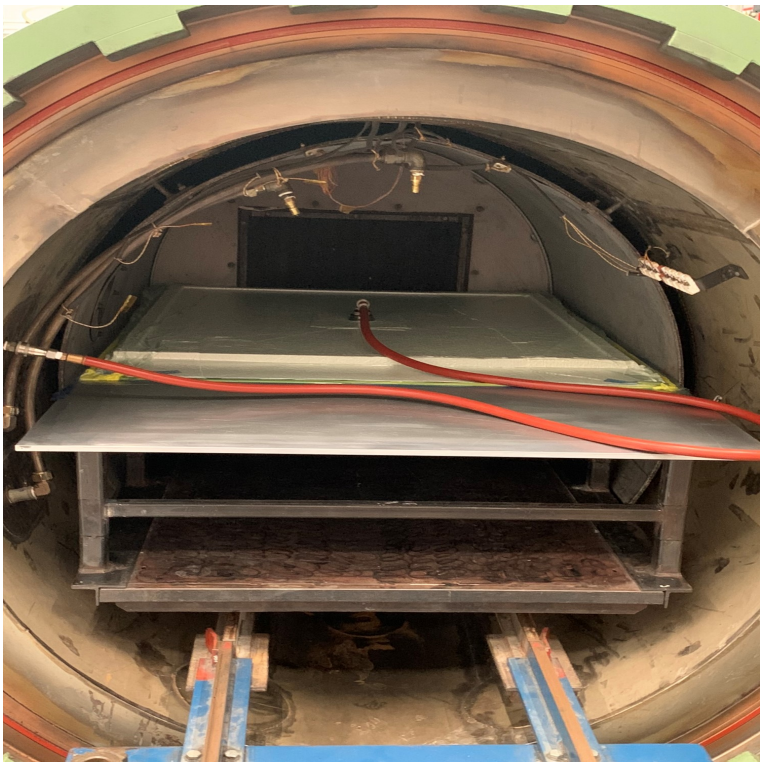

Figure 5.8: Panel ready for curing in the autoclave

The autoclave is then closed, and the following curing cycle is programmed to its system, started. The curing cycle takes approximately 6 hours.

- Apply a vacuum of 800 mbar (gauge) and leave part under this vacuum for several hours to draw out all the air, do not vent vacuum bag
- Pressurize autoclave to 6 bar (gauge)
- Heat at 2 °C per minute until temperature reaches 107±5 °C
- Hold at 107±5 °C for 60 minutes
- Heat at 2 °C per minute until temperature reaches 177±3 °C
- Hold at 177±3 °C for 10 minutes
- Vent vacuum to atmosphere, maintain autoclave pressure at 6 bar (gauge)
- Hold at 177±3°C for 140 minutes (time starts when vacuum is vented)
- Reduce autoclave pressure to 0.5 bar (gauge) while maintaining 177±3 °C (for flat parts this can be skipped if the autoclave can't do this)
- Cool down at <2.5 °C per minute until the part has reached a temperature below 60 °C
- Release remaining pressure
- Remove part from the autoclave
- Allow to cool to room temperature before de-molding

It should also be noted that, the curing cycle is designed by ATG and not part of this thesis project. Once the part is fully cured, the autoclave is opened and the part is left to cool down to room temperature. The vacuum bag, the silicone blocks, and the rest of the tooling are removed. Due to the layup being asymmetric, with ribs only on one side, the panel came out bent after the curing cycle. The final cured panel can be seen in Figure 5.9.

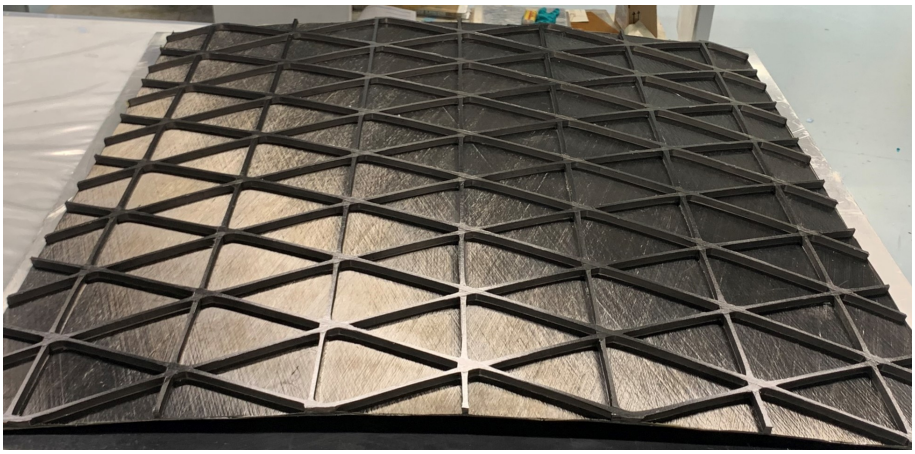

Figure 5.9: Cured panel

#### 5.1.2.4. Specimens cutting

The specimens are then cut into size from the panel. Due to the panel being large, it was only possible to use one cutting machines from the available ones in the lab; which happened to be less accurate. A diamond cutting blade is used, the diameter of the blade was 350 mm and the thickness was approximately 4 mm. The feed of the machine was controlled manually using a hand wheel. Hence, it was not possible to accurately set the feed rate to a certain value. The machine had a maximum rotational speed of 3450 RPM. Secondly, the specimens had to be held by hand during the cutting and not clamped by any means due to its large size. This resulted in a less accurate cut and a small variation in their dimensions. The variations in the specimen size are listed in Table 5.1.

Table 5.1: Variation in specimen dimensions

| Specimen (cell) | length [mm] | width [mm] | Specimen (node) | length [mm] | width[mm] |
|---|---|---|---|---|---|
| **C1** | 239 | 211 | **N1** | 118 | 148 |
| **C2** | 239 | 211 | **N2** | 117 | 148 |
| **C3** | 239 | 209 | **N3** | 123 | 143 |
| **C4** | 239 | 211 | **N4** | 115 | 149 |
| **C5** | 239 | 211 | **N5** | 118 | 148 |
| **C6** | 239 | 211 | **N6** | 117 | 147 |
| **C7** | 239 | 211 | **N7** | 118 | 147 |
| **C8** | 239 | 212 | **N8** | 117 | 149 |
| **C9** | 239 | 209 | **N9** | 117 | 147 |
| **C10** | 239 | 211 | **N10** | 118 | 145 |
| **Average** | 239 | 210.7 | **Average** | 117.8 | 147.1 |
| **Maximum** | 239 | 212 | **Maximum** | 123 | 149 |
| **Minimum** | 239 | 209 | **Minimum** | 115 | 143 |
| **Target value** | 239 | 211 | **Target value** | 117 | 148 |

#### 5.1.2.5. Naming convention

The first step after cutting the specimens was to name them. Different parameters had to be considered when naming them, the intention was to include the following information in the names: (1) Panel number, (2) Specimen number, and (3) Impact type. While naming, specimens of the same type were selected from both panels, e.g., two pristine cell specimens selected from the first panel and one from the second panel. This was done to minimize the effect of possible manufacturing defects in one of the panels on the test results. Apart from this, the specimens were selected and named randomly.

The names consisted of three parts: the first part tells the panel number, the second part tells the specimen type and the specimen number, N for node specimens and C for cell specimens, and the third part tells the intended damage type, BV for BVID, VD for VID, and UN for pristine damages. E.g. P1-N5-BV: Node specimen number 5, cut from panel number 1, with the intended damage being BVID.

It should be noted, however, that after the impact tests, the last part of the names became unrepresentative to the actual damage type. The reason is that the impact energy levels did not result in the intended damaged, this will be further discussed in chapter 6. It was decided to not change the names to keep them consistent with the project data that was created earlier, e.g., the c-scan images.

## 5.2. Specimens impacting

Before testing preparation, specimens had to be impacted to have the required damage as discussed earlier, BVID and VID. The impact was done using the drop tower at Delft Aerospace Structures and Manufacturing Laboratory.

The tower, shown in Figure 5.10, consists of: (1) a trolley with a release mechanism, where the impactor is attached, (2) a catcher that used to catch the impactor right after the first impact to prevent re-bouncing of the impactor and avoid multiple impacts. The impactor head can be changed, different impactor heads were available at the lab, pointed heads or rounded heads with different diameters. The trolley could go as high as six meters, and extra weights could be added to the impactor. That was more than enough to reach any impact energy needed for that project.

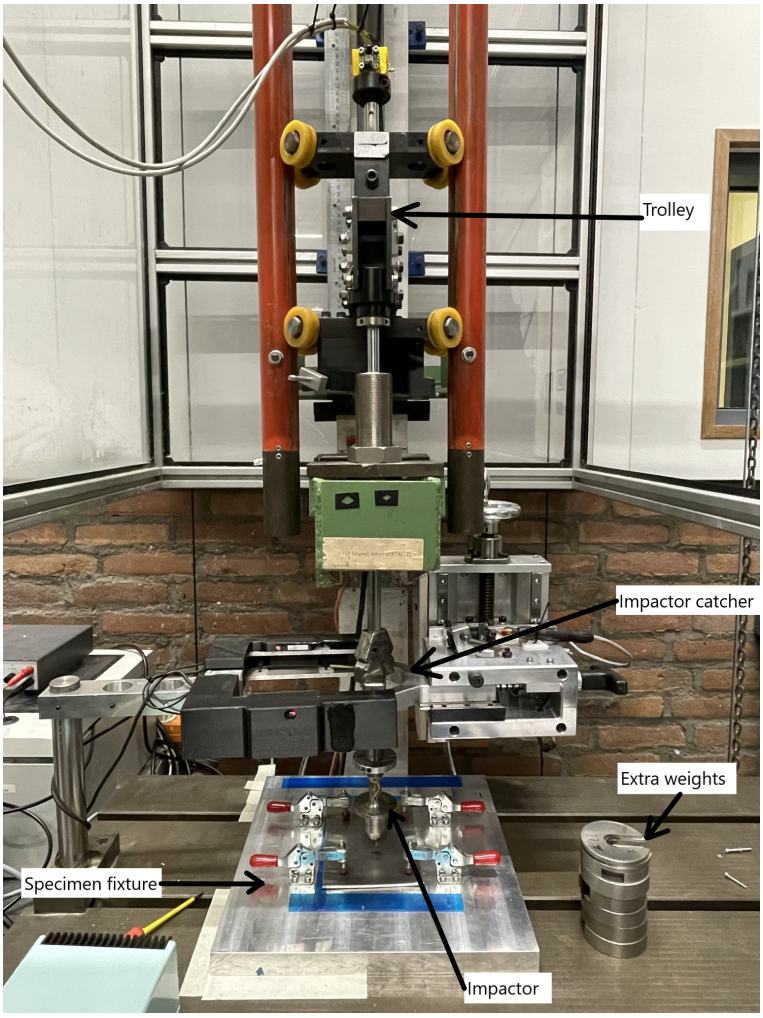


Figure 5.10: Drop tower

The tower was equipped with a load cell and connected to a special software to control it and get some measurements. The software could output the force versus time for every impact. In addition, a high-speed camera was used during the test. The first reason is that the footage and pictures can be used to ensure that the test went well, and the impactor was not stuck or hit by anything before impact. Secondly, the records of the high-speed camera provide access to more information if needed. For example, how much energy went into the re-bounce of the impactor. Figure 5.11 shows pictures from the impactor, approaching the specimen, hitting the specimen, and bouncing. An impact video can be seen in [9].

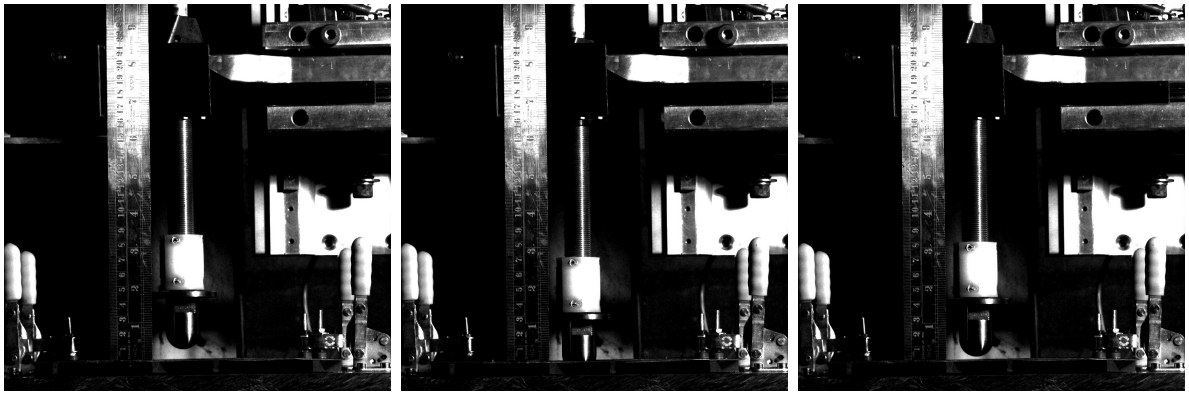

(a) Impactor approaching (b) Impact moment (c) Impactor bouncing

Figure 5.11: Impactor approaching and hitting a specimen

Finally, it was decided to use a simply supported fixture. The fixture was manufactured at the DASML as well. There are currently no testing standards for grid-stiffened structures, and hence, it was difficult to decide on what type of fixture to use. However, small specimens are tested, which in real life will be part of the larger structure. If an area in the larger structure is impacted, causing a certain deformation during impact, the imaginary edges of this area will rotate. This being said, a simply supported fixture is deemed to be more representative to real life scenarios. Obtained from ASTM standards of composite laminate, the design of the fixture was as shown in Figure 5.12.

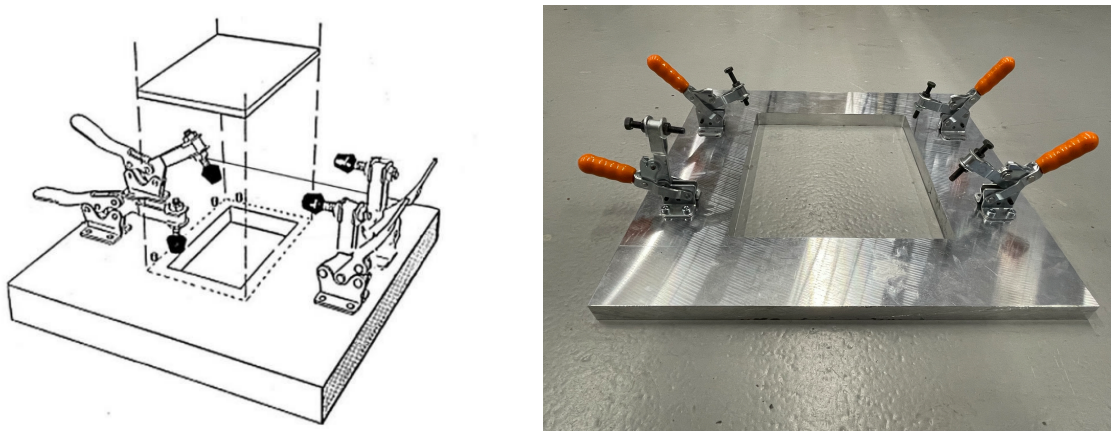

(a) Fixture as per ASTM D7136 (b) Impact fixture for cell specimens

Figure 5.12: Specimen impact fixture

Two different fixtures were used for the node and cell specimens due to the difference in dimensions. The fixture was designed such that the impact point is exactly in the center. Once the setup is ready, several demo tests were done using scrap material. The reason for that is: (1) to ensure the tower is working properly, (2) to validate the selection of the impact energies. Initially, it was planned to use two different energies, 10 J and 25 J, that are supposed to correspond to BVID and VID, respectively. However, upon the tests done with the scrap material, it was found that these energy levels are too low to cause the intended damage for this structure, and hence, it was decided to raise the impacting energy. During the pre-testing, it was very noticeable that the energy needed to cause damage to the cell specimens is much lower than the energy needed to cause damage to the node specimens, and hence, different energy levels were picked for both. The initial energy levels selected for both versus the actual impacting levels are listed in Table 5.2 and Table 5.3 for the node and cell specimens, respectively.

Table 5.2: Cell specimens impact energy, planned versus actual

| Specimen ID | Planned impact energy | Impact energy [J] | Damage type |
|---|---|---|---|
| P1-C1-UN | pristine | not impacted | none visible |
| P1-C2-UN | pristine | not impacted | none visible |
| P1-C3-BV | pristine | 15 | none visible |
| P1-C4-VD | 10 J (VID) | 20 | none visible |
| P1-C5-VD | 10 J (VID) | 27 | BVID |
| P2-C9-VD | 10 J (VID) | 30 | BVID |
| P2-C10-SP | 25 J (obvious) | 33 | BVID |
| P2-C8-BV | 25 J (obvious) | 36 | BVID |
| P2-C6-UN | 25 J (obvious) | 36 | BVID |
| P2-C7-BV | spare | 36 | BVID/VID |

Table 5.3: Node specimens impact energy, planned versus actual

| Specimen ID | Planned impact energy | Impact energy [J] | Damage type |
|---|---|---|---|
| P1-N4-UN | pristine | not impacted | none visible |
| P2-N6-UN | pristine | not impacted | none visible |
| P1-N3-BV | pristine | 30 | none visible |
| P2-N8-VD | 10 J (BVID) | 37 | none visible |
| P2-N10-SP | 10 J (BVID) | 37 | VID on ribs side |
| P1-N1-UN | 10 J (BVID) | 37 | VID on ribs side |
| P1-N2-VD | 25 J (VID) | 43 | sub BVID |
| P2-N7-BV | 25 J (VID) | 43 | VID on ribs side |
| P1-N5-BV | 25 J (VID) | 43 | VID on ribs side |
| P2-N9-VD | spare | 55 | VID on ribs side |

## 5.3. Specimen preparation

After the impact testing was done, it was time to prepare the specimens for the compression test. The preparation included potting of the specimens, adhesion of edge supports, and instrumentation.

### 5.3.1. Potting

The first step was to do the potting for all the specimens, which is necessary to support the specimen during compression testing. This was done by using molds manufactured at the DASML. Two different molds were manufactured, one for the cell specimens and one for the node specimens, that was due to the difference in dimensions between the two types. The mold consisted of a groove where the resin is poured and a specimen holder, and it was a two-sided symmetric mold, Figure 5.13. The holder was at an offset from the middle plane of the mold, such that, when closed the centroid of the specimen is at the center of the groove. Consequently, the specimens' centroid was along the centerline of the potting blocks. It was designed to hold multiple specimens at once because making enough molds for all the specimens would have costed more time and effort. One side is potted and left to cure, then the specimens are flipped as the other side is cured. The curing cycle is cured as per the manufacturer datasheet.

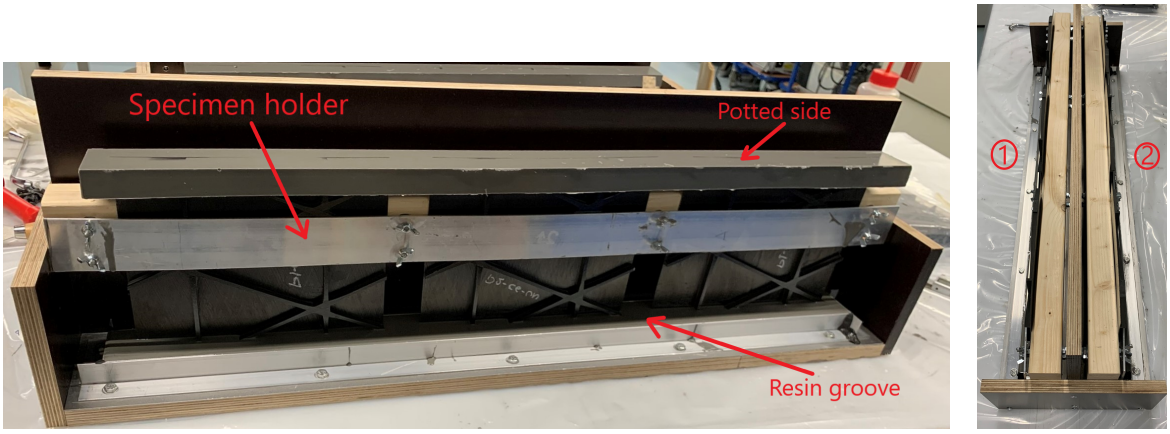


(a) Mould description

(b) Symmetric two-sided mould

Figure 5.13: Potting mould

After the resin blocks are fully cured on both sides of the specimens, Figure 5.14, the specimens are separated. They are then handed to the laboratory technicians to machine the edges. The potted sides are machined to have them as parallel as possible (up to the machining tolerance). That is essential to minimize asymmetric load application.

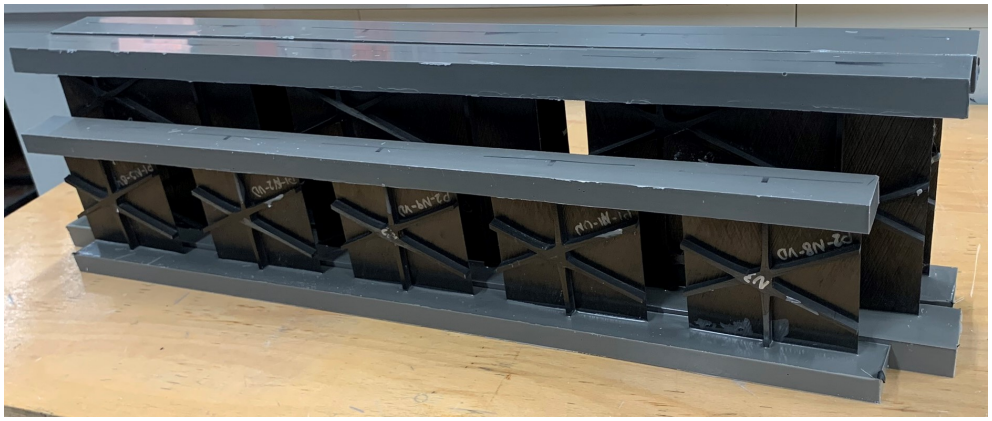

Figure 5.14: Potted specimens

### 5.3.2. Edge supports

To prevent the premature buckling of the open cells near the edges of the specimens, the skin needs to be supported. This can be done either by using a temporary support frame during the test, or by adding a permanent support. This support should prevent buckling but, at the same time, should not affect the load carrying capability of the specimen by diverting load away from the specimen and to the edge support. The detailed information on the selection of the support profiles, including the models, are explained in chapter 4. The support profiles used are 10x10x1 mm aluminum l-profiles, which are common off-the-shelf l-profiles. However, they were bought in different length than the specimen length. Hence, the first step was to cut them into the right dimension. Next, they were machined to create the taper at both ends. This was followed by the surface treatment, which was necessary for both the l-profiles and the specimens before applying the adhesive; the areas where the adhesive was going to be applied were sanded with the proper grit, and cleaned thoroughly with ethanol. The adhesive used was Scotch-weld 9323 B/A, a two compound structural adhesive. It was then applied, and the specimens were clamped until it was fully cured, Figure 5.15. The mixing and curing was done in accordance with the potting compound manufacturer datasheet.

Figure 5.15: Clamped edges support during curing

### 5.3.3. Instrumentation

For the compression testing, Digital Image Correlation (DIC) and strain gauges were used. Those required special preparation, which was the last step before the compression testing. Firstly, the DIC speckle had to be applied, this was done by using white paint as the base, the specimen side facing the camera was fully painted in white. After the paint is dry, a black paint cartridge was used to apply the speckle. There was no special tool for applying it, the nozzle had to be pushed midway to get the paint droplets as intended. A trial was made first using a blank white paper right next to the specimen, once the speckle looked good, the paint was applied on the specimen instead. This process was repeated for every single specimen. Optimally, the area should be 50% white and 50% black paint, with the speckle size to be comparable to the pixel size of the camera used. This, however, was very difficult to obtain manually, and the system could just be calibrated for such errors. A typical specimen with the DIC speckle is shown in Figure 5.16.

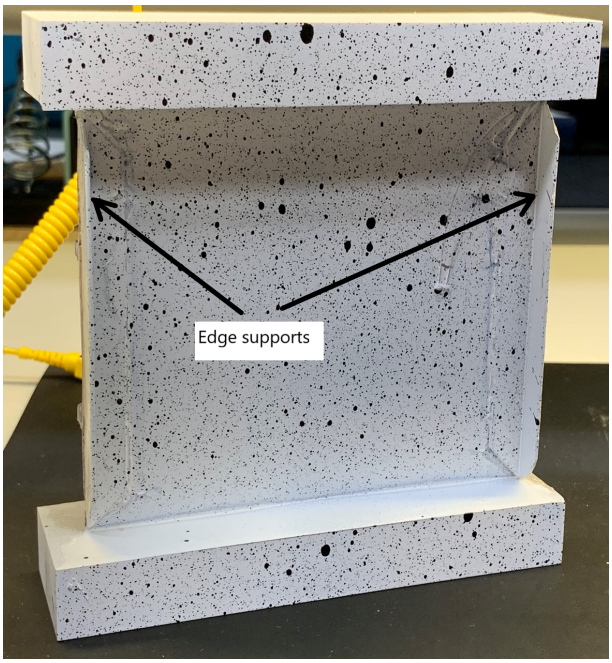


Figure 5.16: Node specimen with DIC speckle

Secondly, strain gauges were added. There were no pre-wired strain gauges available in the laboratory at the time of preparing for the test, the only ones that could be available on a short notice were un-wired gauges. Hence, adding the strain gauges involved a couple of steps. Firstly, sanding of the surface using a fine grit sanding paper, then cleaning the surface with ethanol. Then a drop of adhesive is

added, and the gauge is pushed down for one minute, then left to dry completely. The second step was soldering of the wires to the gauges, which was an intense process to do due to the number of strain gauges used. It was decided to use four strain gauges per specimen, making a total of 80 strain gauges for the 20 specimens., two back-to-back strain gauges on the skin, and two on the ribs on the back of the specimen. For the node specimens, there was only one hoop rib, the two strain gauges on the ribs were then added above and below the node. For the cell specimens, there were two hoop ribs, the strain gauges were added on the same horizontal level on both ribs. The locations for strain gauges are shown in Figure 5.17 for both cell and node specimens. The red dot indicates a location of the strain gauges, the red dots on the skin represent two strain gauges, one on each side. It should be noted that the one stain gauge on the DIC side had to be added and soldered before adding the DIC speckle.

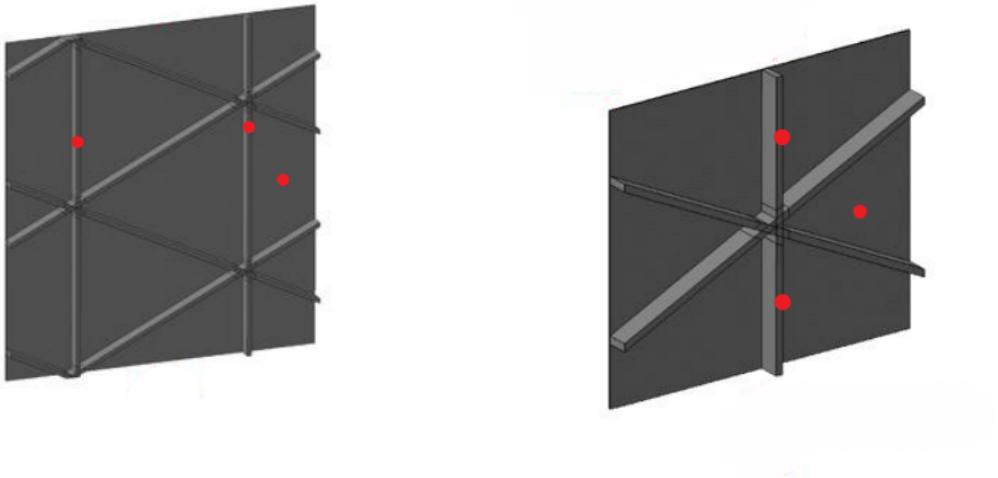

(a) Cell specimen (b) Node specimen

Figure 5.17: Strain gauges locations

## 5.4. Testing

Testing was done using the Zwick 250 kN machine at the DASML. The cell specimens were wider than the standard fixture, for which, the lab technicians had to make some adjustments to the machine. Firstly, the standard fixture was smaller than the width of the cell specimens, and no attachments were available to extend it. They ended up adding two wide metal blocks to the top and bottom fixtures using double face tape. This required them to program the machine accordingly to consider the dimensions of the extra blocks added. No special tools had to be used to attach or hold the specimens during testing, it only had to be placed on the metal base and within the focal length of the DIC camera. To ensure that it is always within the same focal length, a mark was made on the baseplate of the test machine, where the specimen had to be placed exactly for every single test. A picture showing the test setup is shown in Figure 5.18.

The DIC camera was positioned at a certain distance from the specimen and fixed to that position, the settings were then adjusted accordingly to ensure that the entire specimen is in-focus. A two-camera system was used to capture the out of plane deformation. Hence, it has to be ensured that both cameras are in-focus. One could set different setting for both cameras if needed, that is, however, not favorable since it might require different settings for the different cameras in the post-processing software, e.g., different subset size, and in extreme cases, where the settings are too different, the post-processing tool might not be able to use both set of pictures in the same analysis, consequently, will not be able to calculate the out-of-plane deformations. Fortunately, for this test setup, both cameras worked with the same setup. In addition, the DIC system came with a separate PC, which had the software through

which it could be controlled. The camera system was connected to the machine as well, to retrieve the force and displacement data, hence, for every single picture, the force applied at this time is recorded, in addition to the total displacement of the machine.

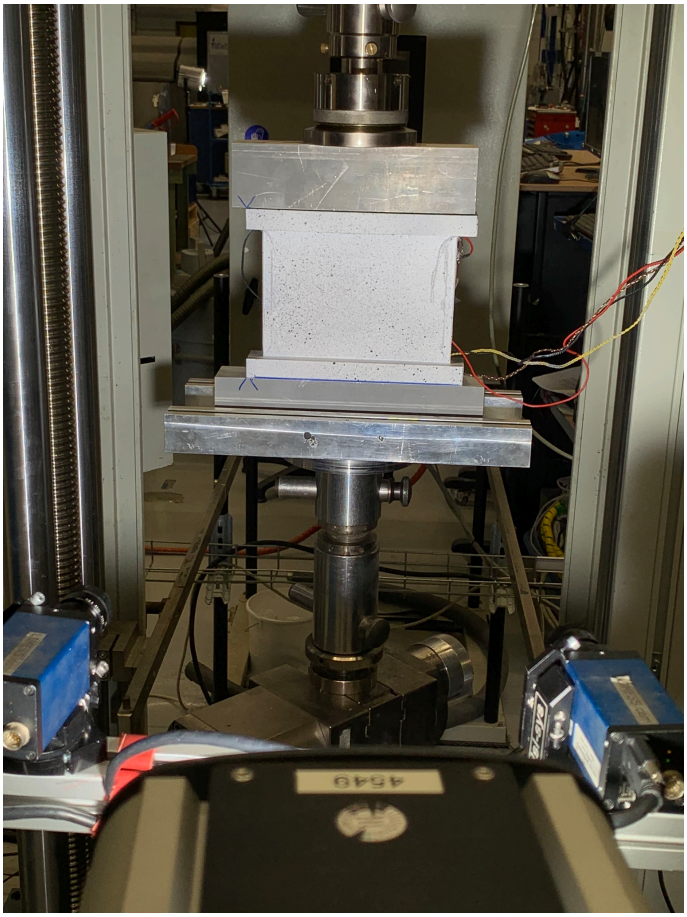

Figure 5.18: Test setup

# 6

# Results and Discussion

After each work package, a set of results and/or data is gathered. In this chapter, the results from each work package are listed and discussed. This starts with manufacturing discussion in section 6.1. Followed by the discussion on the NDT results pre- and post-impact in section 6.2 and section 6.3, respectively. Results from compression tests for both cell and node specimens are then discussed in section 6.4. Finally, based on these results, the model is revisited to reflect on the accuracy in predicting the test results, and possible improvements in section 6.5

## 6.1. Manufacturing

During the manufacturing process, the manufactured panel and the specimens were visually inspected. Similarly, after the manufacturing was completed, non-destructive testing was done for all the specimens. This was done before and after impacting the specimens. In this section, the findings from the pre-impacting inspection are discussed.

Starting with the large panels, it was apparent before demoulding the panels after the curing cycle was complete that they are bent. The bending was symmetric with a maximum height of 37 mm at the middle of the panel, which was 856 mm wide, Figure 6.1. Hence, the panel was bent at an angle of approximately $4.9^o$ at the edges. This caused the helical ribs in both directions to be loaded in tension. A quick thermo-elastic analysis was done by one of the engineers in the team showed the same deflection, which resulted from the skin layup being asymmetric [70,-70,90]. The analysis showed some non-zero failure indices in the helical ribs already even when the panel is mechanically unloaded. It was expected, however, that the preload will not affect the compression testing a lot, since it is only in the helical ribs. The curvature, however, added to the stiffness of the tested specimens, since the specimens tested in compression along the hoop ribs direction, and the bending was along the other direction. The same bending occurred in both panels and similar NDT results were obtained, which validated the model results, and showed good manufacturing quality. The NDT results are discussed in section 6.2 and section 6.3, and the complete results are listed in Appendix A. The bending remained noticeable as long as the panel was not cut, and it did relax over time. The reason and the effect of the relaxation were not investigated further during this project.

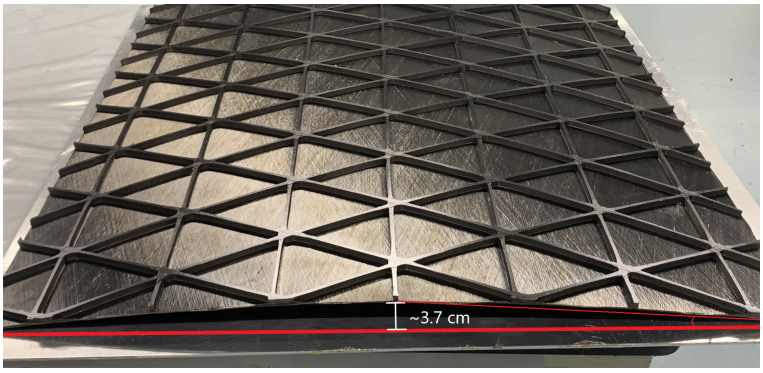


Figure 6.1: Specimen bending measurement

After the manufacturing of the two panels was completed, the specimens were cut out of the panels following the nesting shown earlier in this report. For some specimens, a delamination and/or splitting between the helical ribs and the skin were noticed. An example from two different specimens is shown in Figure 6.2, the delamination extended for 6.5 mm and 10.5 approximately along the rib for the left and right specimens, respectively. The reason for this could be related directly to the preload in the panel with the cutting machine. Various reasons could result in such defects during cutting, firstly, the blade not being sharp enough, not using the proper RPM, not using the proper feed rate, etc. Due to the panel size, it was not possible to cut the specimens using the automated machine. Hence, the panel had to be held by hand during the cutting process, which required two persons, one to hold it and one to operate the machine. It was not possible to let the cutting blade move automatically, an old-fashioned wheel had to be rotated manually to move it. Consequently, it was difficult to cut all the specimens with the same feed rate. Finally, this machine used only a thick blade, approximately 4-5 mm thick, which might have affected the quality of the cut edge if any of the other operating parameters are varied. Finally, it was also clear that the preload contributed to such defects, since, it was only noticed in helical ribs rather than the hoop ribs.

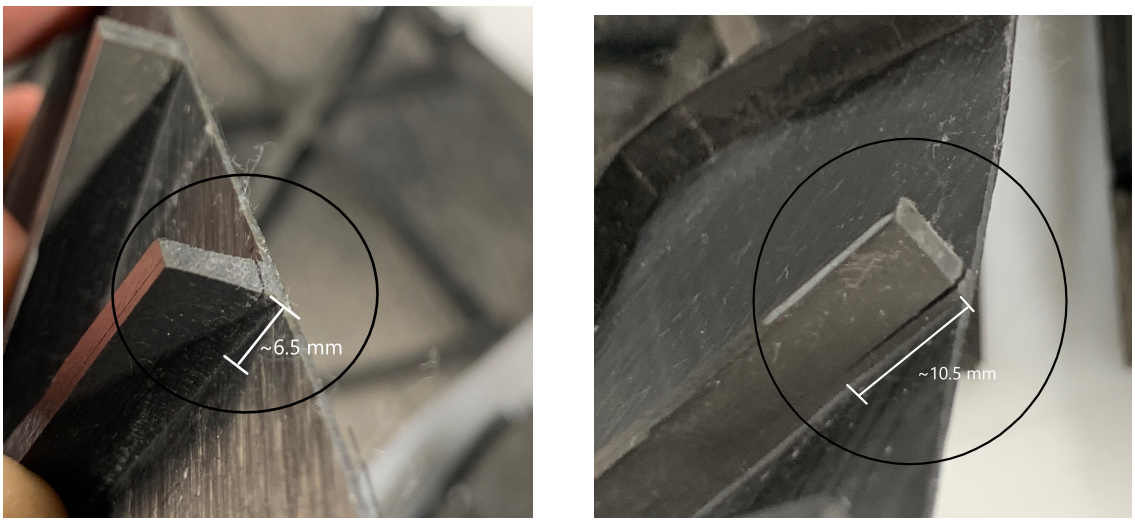


Figure 6.2: Helical ribs delamination

## 6.2. Non-destructive testing

### 6.2.1. Pre-impact

The specimens were inspected using C-scan before and after impact. In this section, the results from the NDT are explained. A 5 MHz sensor was used for all the C-scan pictures obtained, both before and after impact, same scanning speed and resolutions as well. A typical C-scan image is shown in

Figure 6.3. The x- and y-axes are represented the length and width of the specimen, respectively, in the machine coordinates. The origin was set to be the left bottom corner of the specimens. The color map represents the signal intensity measured in decibels. The intensity represents the thickness of the specimen. Hence, in this figure, the darker the color gets, the thicker the specimen is (moving top down along the color bar on the side). Dark spots mean that no signal is received. The variation in the green color intensity on the skin shows the different layup orientation. The ribs are clearly shown in the yellow-orange colors. The top sides, left and right, either have no signal received or red signal. These correspond to the clamping location of the specimen, and hence, no data can be retrieved from this region.

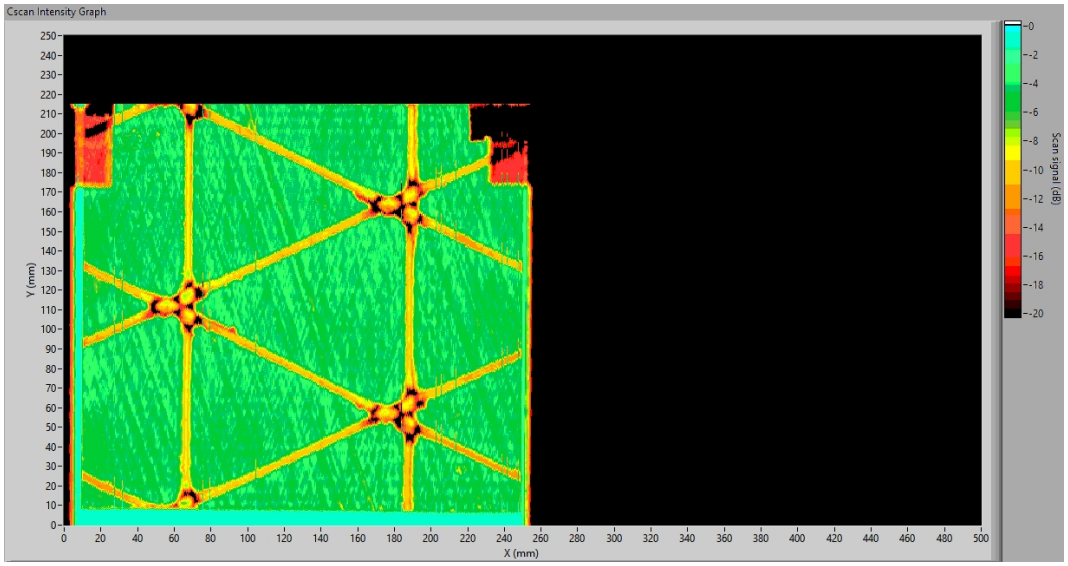


Figure 6.3: Pre-impact C-scan of $P2 - C9 - VD$ specimen

For the nodes, there are always dark spots, and there are multiple explanations for this. Firstly, ply drops occur in multiple regions in the node, due to the transition from two ribs layup overlap (32 plies) in the node area, to the rib region where only one set of layup exists (16 plies). This means that resin pockets exist in this region more than any other places, which are likely to reflect the signal when it hits one pocket. Since there are 16 plies in the ribs, the existence of multiple pockets (between every two plies) can cause a complete distraction of the signal. To further validate this, microscopy images were taken for the nodes from untested specimens.

### 6.2.2. Microscopy

The results from the microscopy are shown in Figure 6.4. The cut was done at the vertex of the node from the intersection of the two helical ribs, as illustrated on the right picture. The microscopy can, shown on the left, showed the presence of resin pockets at the location of all the ply drops, which happen at the transition from the node intersection to the rib. The resin pockets are visible in dark gray color in the figure, a few examples are highlighted in the blue circles. In addition, as expected earlier, a couple of air voids were noticed in the scan, the dark spots highlighted in the red circles. These voids together with the resin multiple resin pockets above each other caused the dark spots in the c-scan, Figure 6.3. It was also noticeable from the c-scan pictures that the dark areas are included within the ribs always, meaning that the resin pockets and/or voids do not extend all the way to the edge of the rib. This could also be noticed in the microscopy image, highlighted in the green rectangles on both sides.

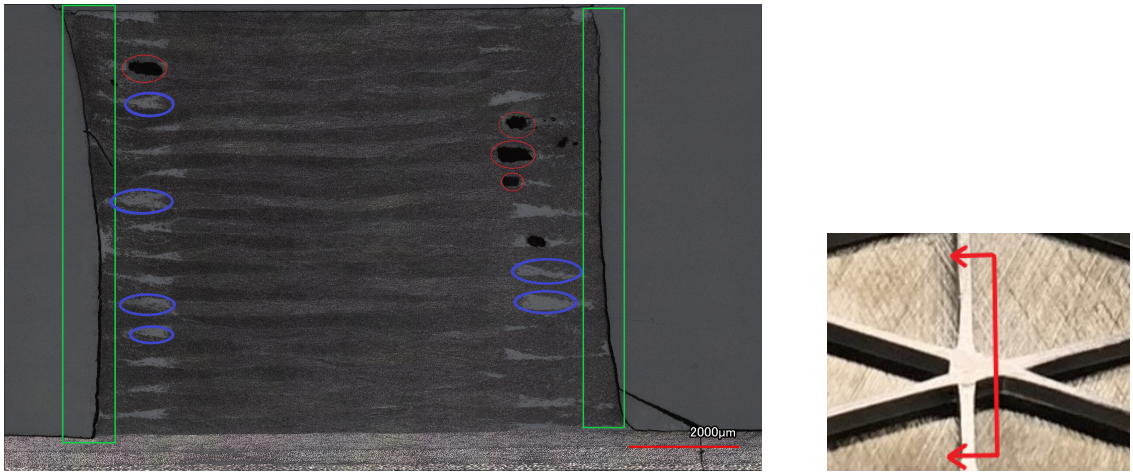


(a) Microscopy image (b) Cut location

Figure 6.4: Node microscopy image

## 6.3. Post-impact, visual inspection and NDT

All the impacted specimens were C-scanned again after impact to investigate the actual damage that happened to the specimen. This was particularly important for the specimens where no actual damage or small damage was seen. In this section, the damage resulted from the different impacts is discussed and compared to the pre-impact state of the specimen. For the C-scan images, only the color maps are shown without the color bar, the range and the color gradient was the same for all the specimens and is shown in Figure 6.3. As explained earlier, the impact testing did not go as planned even after raising the BVID and VID energy levels, hence, the results section will also explain the progression of the test, and it will be divided to two subsections covering the cell and node specimens respectively. It should be noted that further discussion will follow on the progression of the impact testing in the discussion and the recommendations chapters, respectively.

### 6.3.1. Cell specimen

The impact energy levels were set to 15 J for BVID of the cell specimens after the initial trials. The actual specimens were then impacted/ The first one was impacted at 15 J using an impactor with a 25 mm diameter. There was no damage noticed after the impact. the energy level was then raised to 20 J, and no damage was noticed as well. The scan of these specimens, however, showed a small delamination in the skin. An example is shown in Figure 6.5. The image on the left is for the same specimen before impact, and on the right is after impact. The delamination in the impact location is highlighted in the picture.

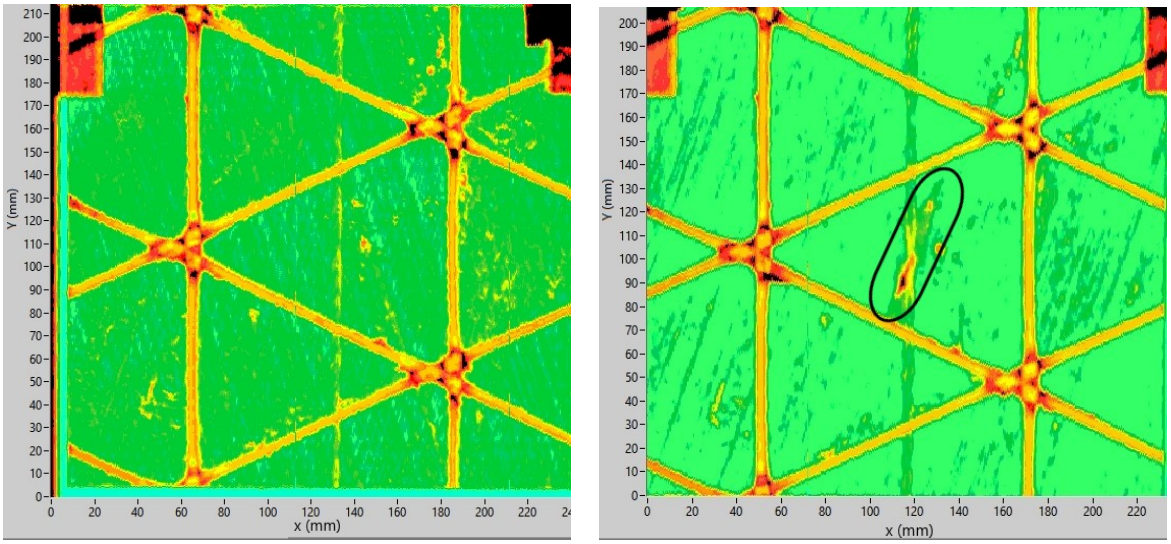


(a) Pre-impact (b) Post-impact

Figure 6.5: Invisible damage, specimen P1-C4-VD, 20J

The energy level was then raised to reach the BVID, an impact energy of 27 J was tried. A larger dent was noticed this time, it can be considered BVID or sub-BVID, since depending on the lighting one might or might not see it clearly, for that reason, the impact damage corresponding to the BVID was increased gradually, first to 30J then to 33J. However, the damage resulted from these impacts could definitely be noticed during regular inspection of the aircraft. The picture of the dent resulting from this impact is shown in Figure 6.6. In addition, a larger delamination was seen in the c-scan images, as shown in Figure 6.7.

Figure 6.6: BVID, specimen P1-C5-VD, 27J

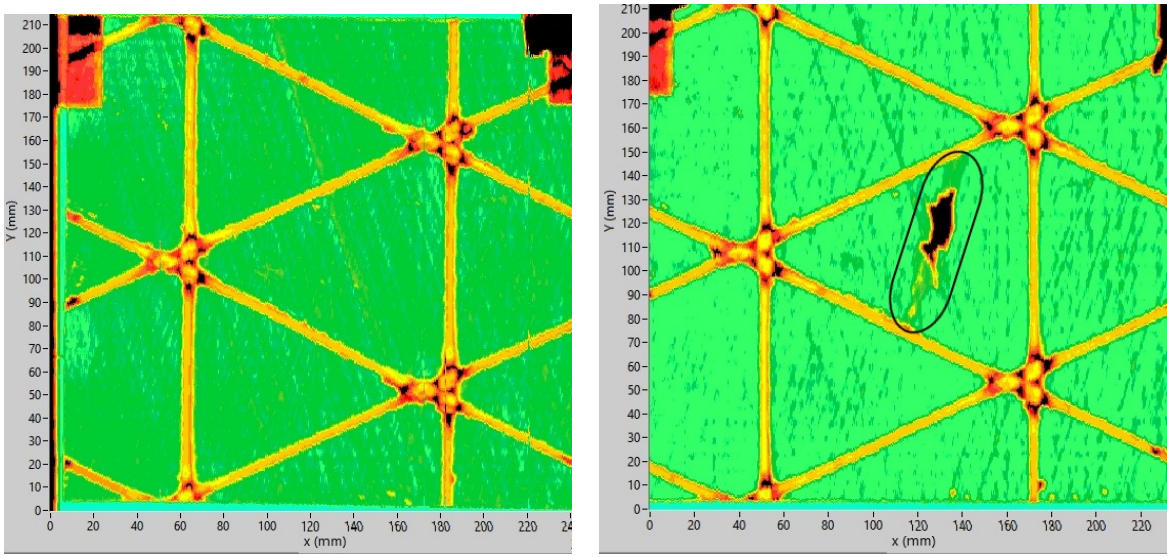


(a) Pre-impact (b) Post-impact

Figure 6.7: BVID, specimen P1-C5-VD, 27J

The impact energy was then increased further to 36J. It was then decided to not increase it further and impact another two specimens with that energy level, hoping for a VID. The reason for that is, the cut-off energy was set by the manufacturer for that project to be 30J anyway, and it was apparent from the c-scans that delamination occurs in the skin of the impacted cells upon impacting it with 36J. Since the skin was very thin, only 0.84 mm, it was expected that further increasing the impact energy might just result in a full penetration of the skin. The damage on the impact side (skin side) of the specimens impacted at 36J was not very different from the preceding tests, a noticeable difference, however, was that the damage was more local resulting in a slightly deeper dent, as shown in Figure 6.8. A very similar damage pattern to the rest of the impacted specimens was seen in the C-scan images. It was noticed that as the energy level increases, the delamination area extends along the $-70^o$ more towards the ribs. For the specimens impacted at 36J, the damage area was from one helical rib to the other, as seen in Figure 6.9. This was noticed regardless of how the external damage looks.

Figure 6.8: Specimen P2-C8-BV, 36J

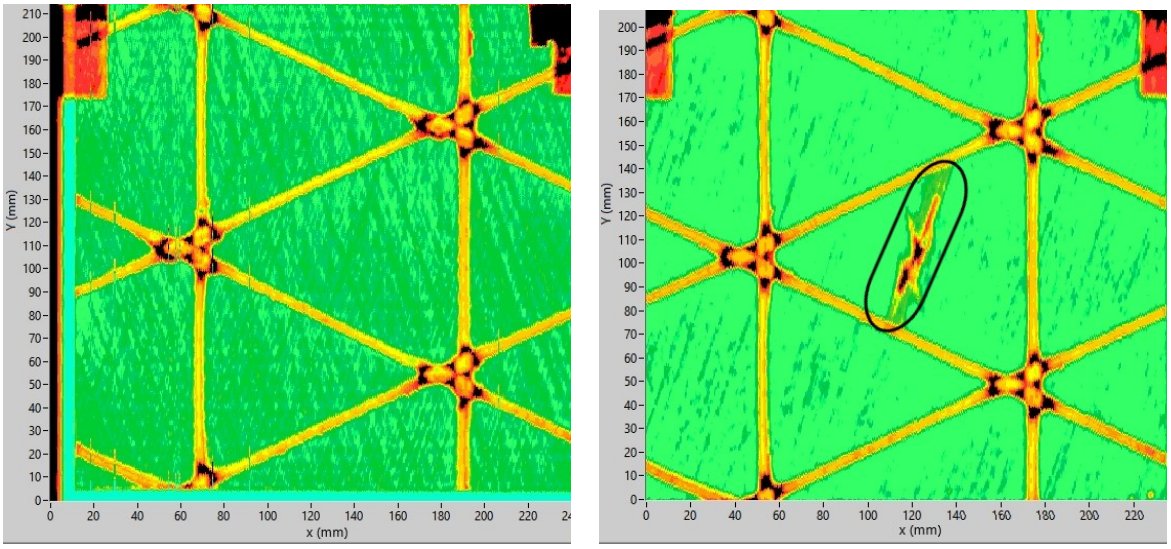


(a) Pre-impact (b) Post-impact

Figure 6.9: BVID, Specimen P1-C8-BV, 36J

The delamination resulted from impacting cell specimens was measure from the c-scan images, and was plotted as a function of the impact energy, Figure 6.10. From the c-scan images, it can be seen that delamination occurred resulted in full separation between the different plies near the impact location, the dark spots in Figure 6.9, as you move farther, the severity of the delamination reduces. Only the dark spot were used to measure the delamination and create the best-fit curve. The skin of the impacted specimens had a thickness of 0.84 mm, and consisted of 3 plies [70,-70,90]. For all the specimens, it was noticed that the delamination grows along the $-70^o$ direction. Hence, the delamination was measured along that direction.

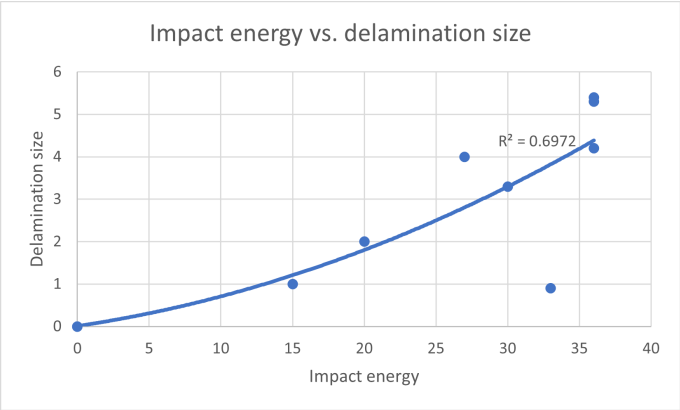


Figure 6.10: Impact energy vs. resultant delamination, cell specimens

### 6.3.2. Node specimens

For the node specimens, the impact tests proceeded differently, and the resultant damage was inconsistent for the same impact level. For example, different resultant damage was noticed for two specimens that were impacted with the same energy. During the testing of the scrap specimens, the specimen could withstand impact damage to up to 60J without visible damage. However, there were a few differences between the two sets of specimens and tests. Firstly, when it was noticed that causing visible damage in the node specimens using the 25 mm impactor is very difficult, another impactor was used; which had a pointed head instead, the diameter of the head was approximately 4 mm. Using this impactor, visible damage was seen at lower impact energies during the initial trials. Hence, it was

decided to use this impactor to avoid going to very high-energy impacts. The difference between both heads is shown in Figure 6.11.

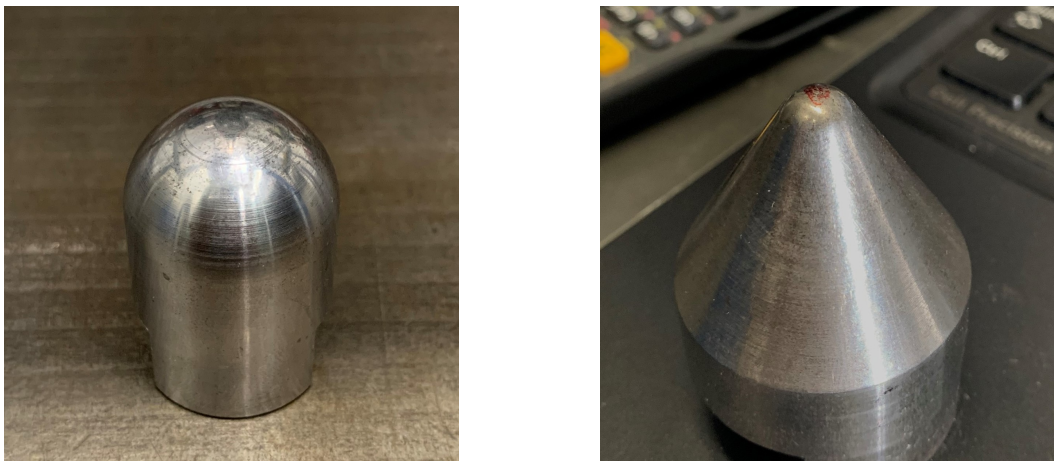

(a) 25mm impactor (b) Pointed impactor

Figure 6.11: The difference between impactors used for cell and node specimens

Based on the initial trials using the pointed impactor, an impact energy of 30J was tried for the BVID test, which did not cause any visible damage on the specimens. No damage was noticed in the C-scan images either. The impact energy was then raised to 37J, and no damage was noticed either. This was followed by 43J and 55J. For the 43J impact, small damaged was noticed in the ribs on the back of the specimen, but it was doubting whether this damage can even be categorized as a BVID, since it was difficult to catch. There was not much difference visible in the c-scan images before and after impact for this specimen, either, Figure 6.12. The approach was then to go to a considerably higher energy level, if only BVID was noticed, then another increase is done, if VID is noticed, then this energy level can be used as the VID energy level and another one between 43 and 55 is used for the BVID specimens. If too much damage, beyond VID or clearly VID, is noticed, then a step back would have been done to reach the correct VID for the node specimens.

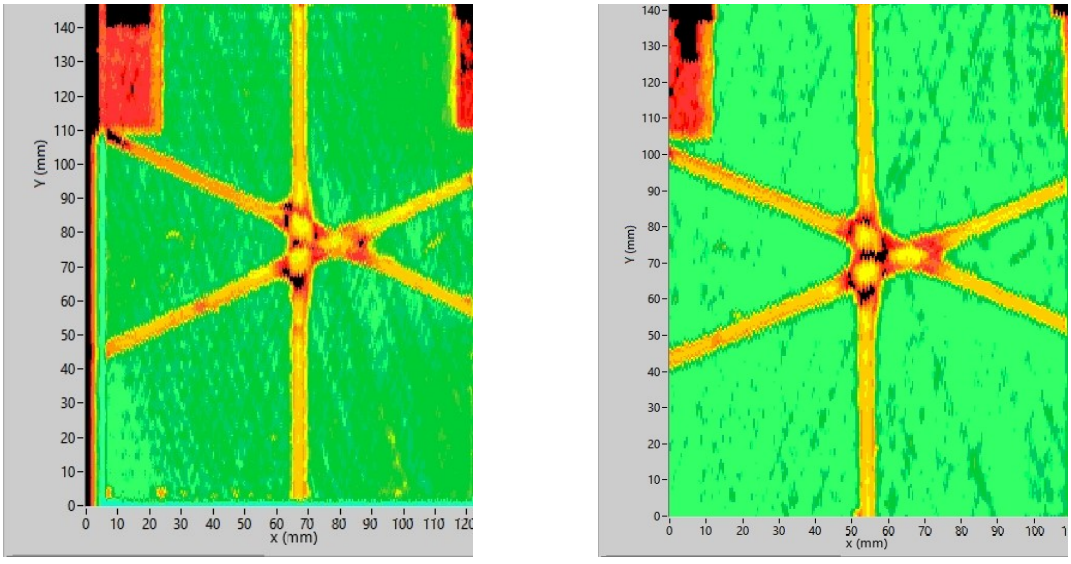


(a) Pre-impact (b) Post-impact

Figure 6.12: Specimen P1-N2-VD, 43J

For the node specimens, constructing a figure similar to Figure 6.10 was not straightforward. The delamination and/or skin-rib separation always occurred in the node area and along helical ribs, and often initiated from the edge of the specimen towards the node and/or from the node towards the edge. There were two helical ribs in the node specimens extending in both sides of the node, and hence, four possible locations of initiation of damage due to impact. The damage did not always start in the same location, for example, for one specimen, it can be seen on one end of one helical rib only, while for other it is seen on two different ribs, an example is shown in Figure 6.13. In addition, for some specimens, inconsistent resultant damage was noticed. Thus, it was not possible to have the damage size as a function of the impact energy.

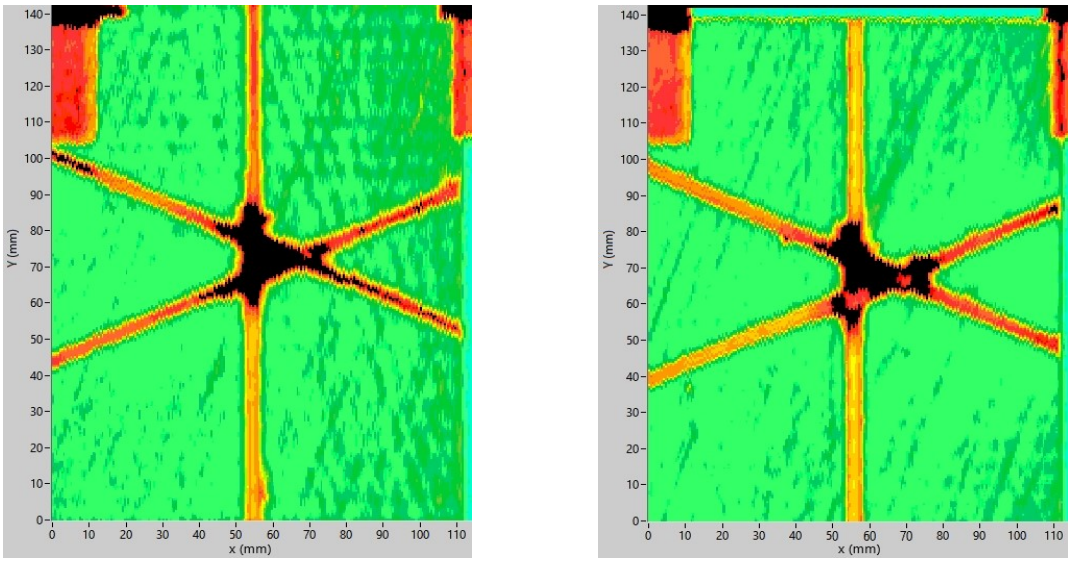


(a) Pre-impact (b) Post-impact

Figure 6.13: Difference in the resultant damage between two different specimens

### 6.3.3. General remarks

- **Cell specimens**
  - For the cell specimens, the damage is always contained within the impacted cell and never propagated beyond the ribs forming this cell.
  - The delamination in the cell specimens is seen in the c-scan to be usually along the $-70^o$ fibers.
  - The difference between the specimen size of the trial and the actual specimens made a large difference in the resultant damage. The specimens used during the pre-testing were often smaller, the same energy level that caused BVID on the actual specimens, caused clearly VID (or even full penetration) on the scrap specimens.
  - For the larger specimens, a considerable flexure was seen in the footage from the high-speed camera, the impact video can be seen in [9]. And a larger amount went into the rebounce of the impactor. This could be seen by the height to which the impactor went after the impact.
- **Node specimens**
  - The damage was often visible on the ribs side of the specimen only, which makes it doubtful whether it can be categorized as a BVID or VID or not, since this side is not regularly checked daily, as part of the pre-flight check for example, only during regular maintenance.

- For all the node specimens with visible damage, the same damage was noticed, which is a visible delamination and/or separation between the ribs and the skin.
- A large difference was seen in the resultant damage between the actual specimens and the scrap ones. Similar to the cell specimens, the main difference in the specimens were the size.
- Due to the variation in the size of the scrap specimens, the impact location was not always in the center of the specimen; which had a noticeable effect on the resultant damage.

## 6.4. Compression testing

The compression tests proceeded as explained in section 5.4, in this section, the test results are explained. The first subsection will discuss results of the cell specimens, followed by the node specimens in the second subsection. Data from test machine and DIC are used. It should be noted that due to a technical problem in the amplifier used to read the strain gauges data, the data from strain gauges corrupted, and it was not possible to use them.

### 6.4.1. Cell specimens

Table 6.1 shows the failure loads of all the tested cell specimens, their impact energy, and the noticed damage type. The lowest achieved failure load was 33.6 kN and the highest was 41.5 kN. The interesting part is that the highest achieved was for one of the impacted specimen, specimen P2-C7-BV, which was impacted with 36 J of energy. The highest achieved by a pristine specimen was 40.4 kN. If we consider either of the previously mentioned ultimate loads to be the ultimate load of this specimen, the limit load will be 26.9-27.7 kN. By looking at the test results, one can immediately see that none of the specimens failed at such a low load.

Table 6.1: Compression test results of cell specimens

| Specimen ID | Fmax [kN] | Impact energy [J] | Damage type |
|---|---|---|---|
| P1-C1-UN | 33.6 | not impacted | none visible |
| P1-C2-UN | 40.4 | not impacted | none visible |
| P1-C3-BV | 41.2 | 15 | none visible |
| P1-C4-VD | 39.1 | 20 | none visible |
| P1-C5-VD | 38.7 | 27 | BVID |
| P2-C6-UN | 38.7 | 36 | BVID |
| P2-C7-BV | 41.5 | 36 | BVID/VID |
| P2-C8-BV | 35.2 | 36 | BVID |
| P2-C9-VD | 40.3 | 30 | BVID |
| P2-C10-SP | 34.2 | 33 | BVID |

During potting of the test specimens, there was not enough potting compound at the lab to get the last four specimens to have blocks with the same thickness at both sides. Consequently, for four specimens, one side had a block of 2.5 cm thickness, and the other had a thickness of approximately 1.5 cm, an example is shown in Figure 6.14. Due to time constraints and limited availability of the material at the lab, it was decided to proceed to the test with these specimens. It was expected, however, that this variation will affect the test results. The part of the specimen near the thick potting will experience less rotation than the other part. While would cause higher stress on one side than the other. While it was not certain how that will translate to in the test results, the test results showed indeed an early failure of these four specimens. The largest deviation from the ultimate load achieved could be noticed in these four specimens, P2-C10-SP, P1-C5-VD, P2-C8-BV, and P1-C1-UN. It was noticed for one of these specimens that the ribs broke at the ribs interface, which was not the case for the specimens with equal potting size.

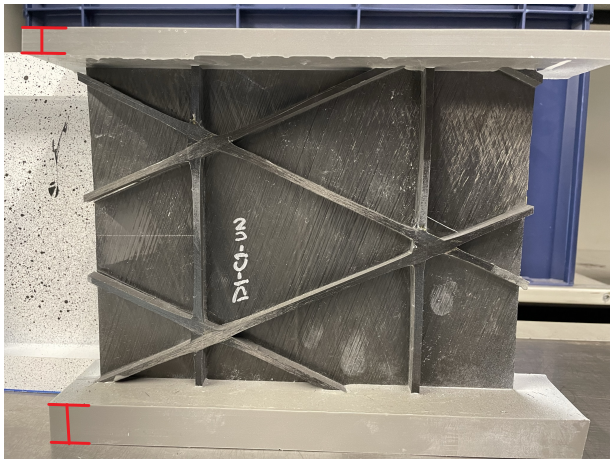

Figure 6.14: Potted specimen with unequal potting thicknesses

Once the machine was on, the load applied detected by the machine load cell was increasing slowly. That was because the machine and/or the specimen are still settling at this stage. After which, the deformation increased linearly with the force applied, Figure 6.15. The skin of the specimens started buckling locally in the cells, and the out of plane deformation at the buckling spots increased with load, a typical pre-failure buckling pattern is shown in Figure 6.16. The local buckling of the skin had no effect on the load carrying capability of the specimen, the buckling was noticed, and no effects were seen on the load-displacement graphs. Until the specimen fails. The typical failure mode that was noticed is skin-rib separation. The load was increasing until a cracking sound was heard, which indicated the skin-rib separation. After which the load dropped significantly, however, the specimen continued to carry approximately half the initially applied load.

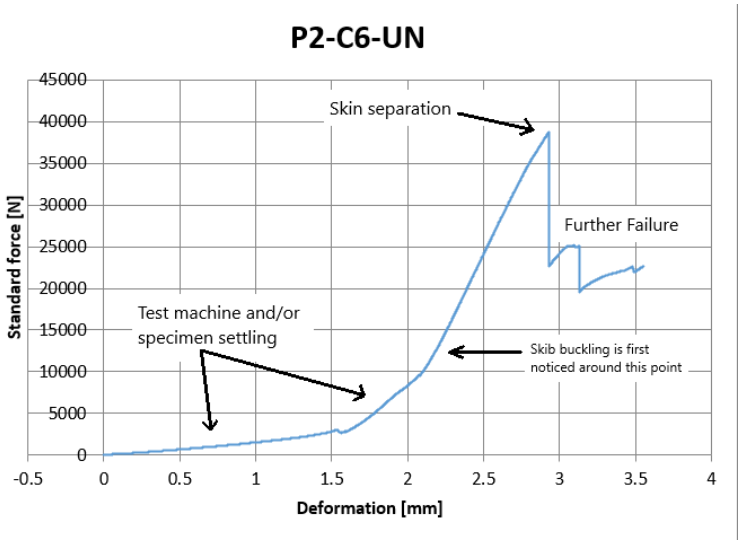


Figure 6.15: Force displacement explanation, specimen P2-C6-UN

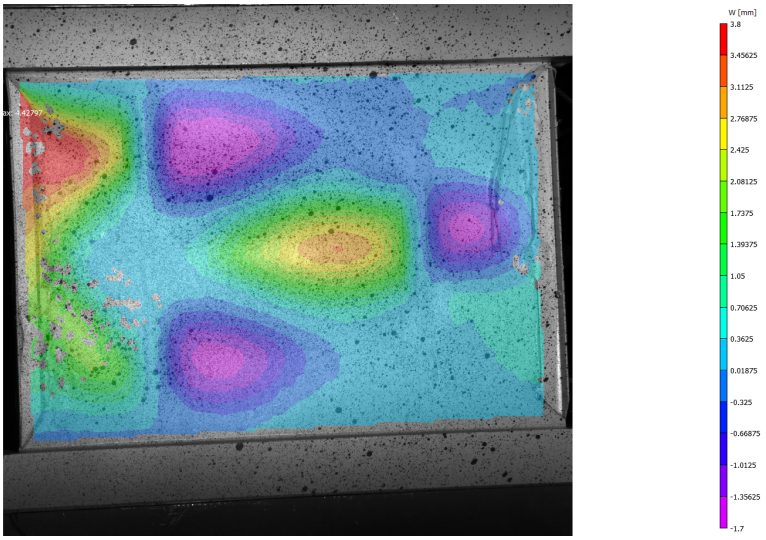


Figure 6.16: Pre-failure buckling of specimen P1-C2-UN

In the first few specimens, regardless of whether they are impacted or pristine specimens, only skin-rib separation was detected as the failure mode. The machine was set to stop at 25% drop from the ultimate load reached. This number was then increased for the subsequent specimens, and material failure in the ribs was noticed. After the skin-rib separation, the skin buckles globally and carries no load, it is believed that the load carried after the separation is only by the ribs. Further analysis can be done to determine how much load goes into the skin and the ribs before separation. The fiber breakage detected in the ribs often occurred in the hoop rib near the node, in the soft region of the node.

### 6.4.2. Node specimens

The node specimens were tested next. before the test, it was expected that there will be a large variation in the test results. The reason for that is: firstly, there was an inconsistency in the impact test results for the node specimens, i.e., the resultant damage from the same impact energy was sometime different. Secondly, because the resultant damage in the node specimens were always delamination in the ribs and/or ribs-skin separation. Hence, since the failure mode expected was the skin-rib separation, the existence of initial separation would result in a much lower strength. As seen in Table 6.2, the results did match the expectations. The specimen with no visible damage achieved the highest ultimate load with only one exception, specimen P1-N4-UN.

Table 6.2: Compression test results of node specimens

| Specimen ID | Fmax [kN] | Impact energy [J] | Damage type |
|---|---|---|---|
| P1-N1-UN | 14.8 | 37 | VID on ribs side |
| P1-N2-VD | 18.7 | 43 | sub BVID |
| P1-N3-BV | 23.6 | 30 | none visible |
| P1-N4-UN | 16.5 | Not impacted | none visible |
| P1-N5-BV | 10.8 | 43 | VID on ribs side |
| P2-N6-UN | 23.5 | Not impacted | none visible |
| P2-N7-BV | 18.7 | 43 | VID on ribs side |
| P2-N8-VD | 22.4 | 37 | none visible |
| P2-N9-VD | 8.3 | 55 | VID on ribs side |
| P2-N10-SP | 17.5 | 37 | VID on ribs side |

This C-scan image of this specimen was checked to look for potential causes of the low failure load. Figure 6.17 shows a delamination and/or separation near the edges, which is considerably greater than the other pristine specimen. This explains the early failure of the specimen, since the dominating failure mode is skin-rib separation, an initial separation would cause an earlier failure.

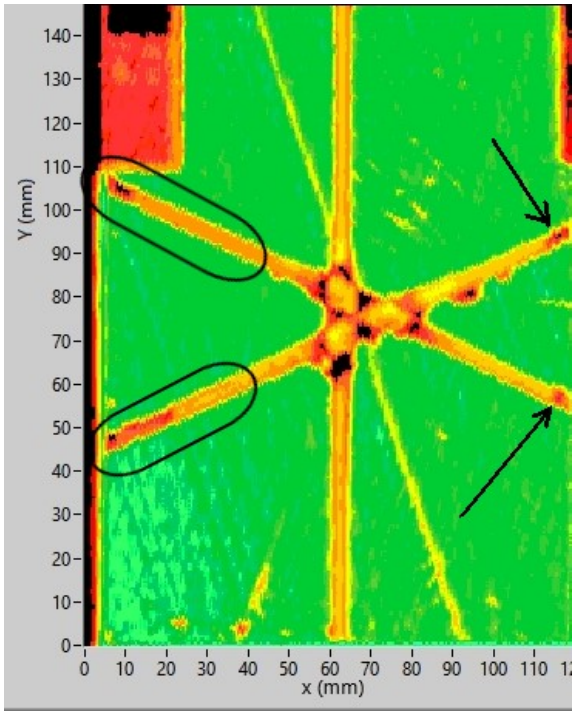


Figure 6.17: C-scan image highlighting rib delamination/separation

The behavior of the node specimen during the test was very similar to the cell specimens, Figure 6.18.In the first part of the test, the specimen and/or the machine settles, followed by a linear behavior. During the linear region, the skin buckles locally until the skin fully separates from the ribs. A typical pre-failure buckling pattern of the node specimens is shown in Figure 6.19. The ribs continue to carry load until failure.

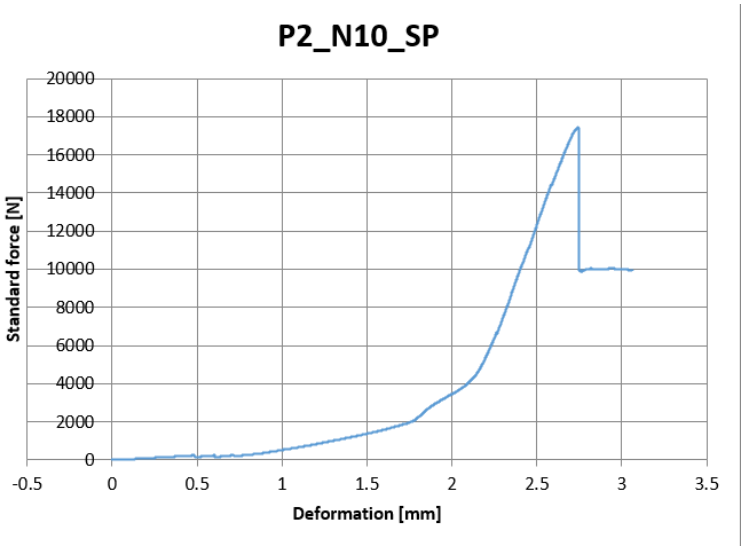


Figure 6.18: Force displacement explanation, specimen P2-N10-SP

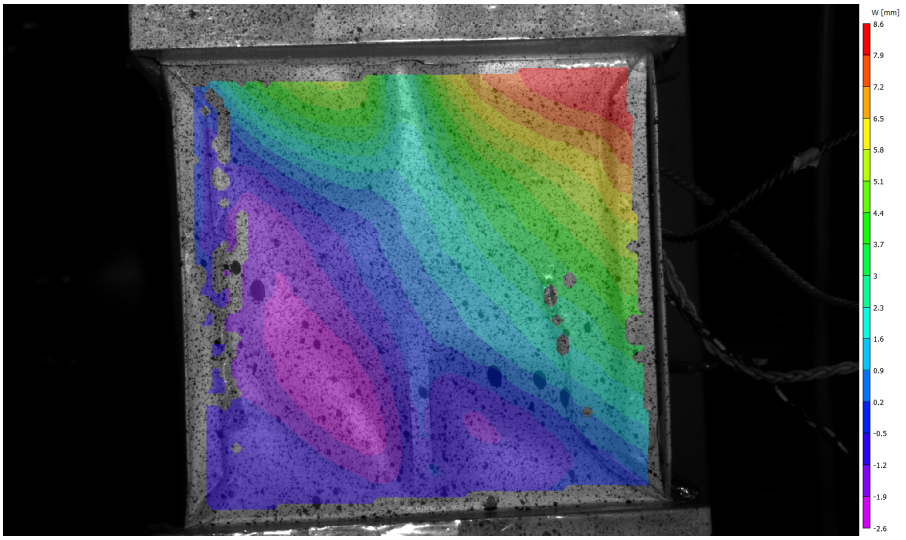


Figure 6.19: Pre-failure buckling of specimen P1-N4-UN

## 6.5. Model revisiting

The first part of the model setup was to run the thermo-elastic analysis to get the post-cure bending of the specimen; the model showed a maximum deflection of 2.93 mm along the center line of the specimen. This was measured using a ruler before the potting and impacting. Initially, the measurement showed a maximum deflection of approximately 3 mm. During compression testing, the same measurement was recorded again, but in a different way. This was taking a DIC picture of the specimen before the test starts and processing it to get the out of plan deformation, which in that case was the initial curvature of the specimen. An example for one of the specimens is shown in Figure 6.20. It should be noted that the model had zero displacement at the edges; hence, the maximum displacement can be read directly from the contour; while for the DIC, the zero reference is set in an arbitrary plane between the edges and the centerline. Hence, the maximum is calculated by subtracting the displacement just before the edge supports from the displacement at the centerline, but not from the middle point exactly, which happened to be a dent from the impact.

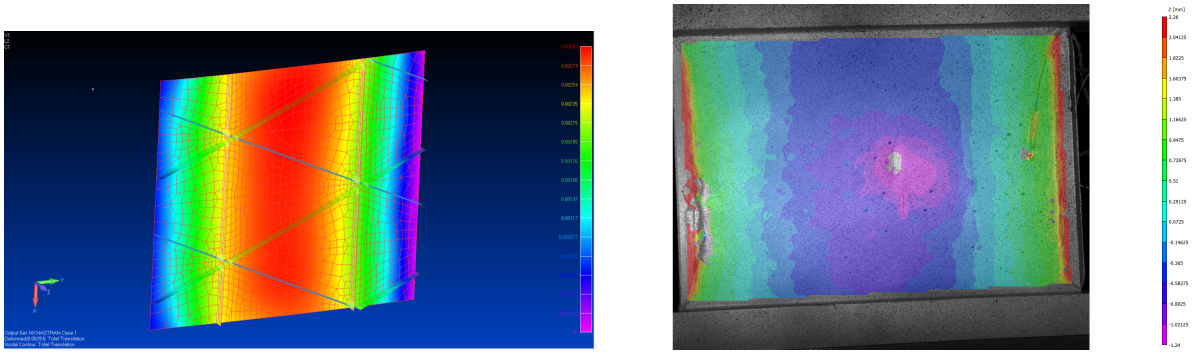

(a) Analysis (b) DIC

Figure 6.20: Bending of the cell specimen

The DIC showed a bending of approximately 2.2 mm along the centerline, which is smaller than the actual measured and the model. This is justified by the fact that the specimens had to be clamped during the potting curing in a way that tends to flatten them, resulting in a smaller curvature after the potting is fully cured. The DIC shows, however, the same symmetry that is shown in the model. These results deemed the thermo-elastic analysis in the model to be accurate enough. Further work can

be done to check the DIC analysis from all the specimens and obtain the average, but this was not necessary for this thesis.

### 6.5.1. Test coupons

The same thermo-elastic analysis was done for both the cell and node specimens, and the resultant displacements were used to deform the nodes, forming their new initial state. The analyses explained in chapter 4 were run, and the results obtained are compared with the experimental results. In this section, the results for both cell and node specimens are discussed.

To validate the model, different approaches can be considered. Firstly, which experimental data out of the 10 specimens are used? The simplest choice would be using the average and compare it to the model predictions, Table 6.3. In this project, average strength underestimates the actual strength of the structure, for example, due to the initial delamination in the node specimens, or the early failure of cell specimens with asymmetric potting sides. The calculation included the outliers as well, e.g., the node specimen failing at 8.3 kN. A more accurate evaluation of the strength of the structure could be obtained by calculating the B-basis and/or the A-basis strength of the structure, depending on the requirements. This would require a larger set of specimen of the same type, e.g., Pristine, or BVID specimens only. One could look at it differently as well, since the model does not consider any imperfections, the model predictions could be compared to the strength of the specimens with the least known imperfections. In which case, the model seems to be predicting the strength quite well, Table 6.4

Table 6.3: Average experimental strength versus model prediction

| Specimen type | Model [kN] | Average strength [kN] | Difference [%] |
|---|---|---|---|
| Cell specimen | 41 | 38.3 | 6.6 |
| Node specimen | 23.8 | 17.5 | 26.6 |

Table 6.4: Maximum experimental strength versus model prediction

| Specimen type | Model [kN] | Average strength [kN] | Difference [%] |
|---|---|---|---|
| Cell specimen | 41 | 41.5 | 1.3 |
| Node specimen | 23.8 | 23.6 | 1.0 |

From the non-linear analysis, the out-of plane deformations could also be obtained. Figure 6.21 shows a comparison between the buckling pattern just before failure from the DIC data and the model. The figure shows good agreement between both DIC and the model. The magnitudes of the deformation are close, for example in the middle of the specimen, 2.5 mm from the DIC and 2.12 mm from the model. The predictions are more accurate away from the edge support, that could be due to imperfections related to the supports, e.g., initial bending in the support, poor adhesion in some places or excess adhesive, etc.

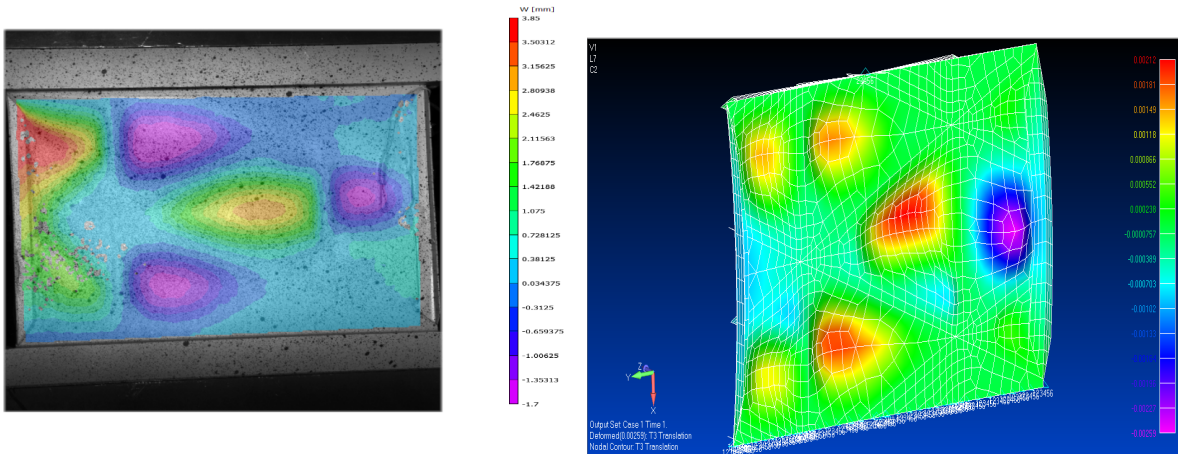


(a) DIC (b) Model

Figure 6.21: DIC versus model

Looking at the node specimens analysis, Figure 6.22, it can be seen that there is a clear variation between the model and the DIC. A few reasons might have caused this. Firstly, it was noticed during the testing of the node specimens that cracks initiated in the potting blocks and grew until the block was broken into two halves along the specimen width. This caused large rotations, specially in the area closer to the support. In addition, for most of the node specimens, there was delamination in the ribs after cutting them, Figure 6.2. For the impacted specimens, this delamination extended along the helical ribs, and in some cases, rib-skin separation occurred near the edge of the specimen. Due to the small size of the node specimen, even for pristine specimens, this delamination could have a noticeable effect on the out-of-plane deformation. The part of the delaminated rib that was in contact with the skin could follow the out-of-plane deformation of the skin easier. Hence, a different buckling pattern was seen in the DIC than that predicted by the model. That is verified by the DIC image, since only the hoop rib can be detected, Figure 6.22.

A set of recommendations are presented later in section 7.2 that could solve these issues. In addition, since most of the load is carried by the hoop ribs, this did not always have a big effect on the failure load of the specimen. Only in the situations where noticeable rib-skin separation existed, that is because rib-skin separation was the failure mode of the specimen, an initial separation led to a faster full-separation, consequently, lower strength. Finally, a finer mesh could also result in better model prediction, it can be seen that the mesh size of the mesh in the deformed cell areas are comparable to the deformations seen.

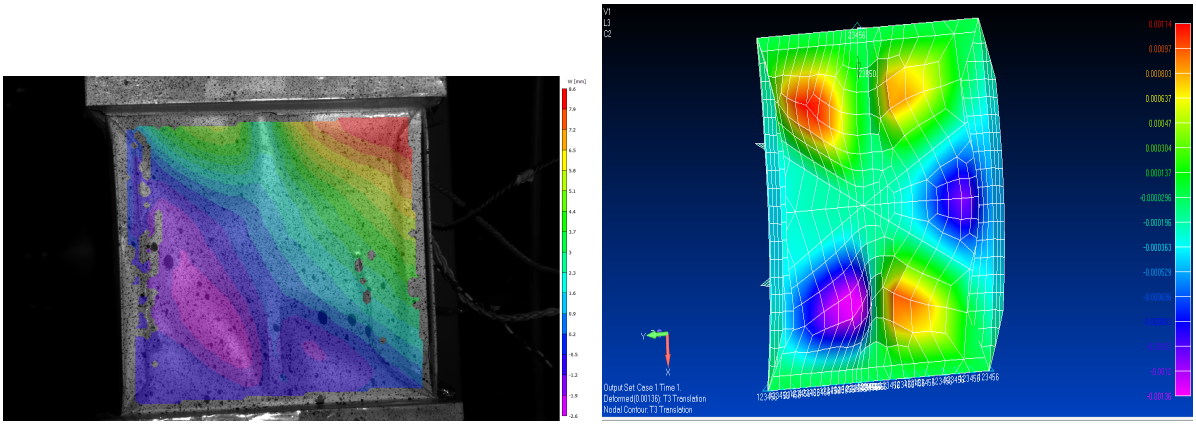

(a) DIC (b) Model

Figure 6.22: DIC versus model

### 6.5.2. Addressing discrepancies

In this section, the variations between the experimental results and the model are addressed.

Firstly, starting with the buckling load, the method by which the buckling of the specimen was determined is by checking the image that shows proper buckling pattern. This could be subjective, specially for the impacted specimens. For example, for the cell specimens, the cell in the center was impacted, which happened to be the cell at which the first buckling mode appears. From the DIC pictures, it can be difficult to tell whether the out-of-plane deformation in this region corresponds to buckling or dent. Hence, one can easily select the image buckling before or after the actual one, which can result in a different load magnitude of a few kilo Newtons. Hence, only pristine images can be deemed reliable to check for buckling. For the cell specimens, buckling was observed at 9.8 kN and 10 kN for the first and second pristine specimens, P1-C1-UN and P1-C2-UN, respectively.

For the node specimens, it was more difficult to check the exact load at which the buckling occurs. Firstly, because a few specimens failed either below or close to the predicted failure load. Secondly, for most of the impacted specimens with visible damage on the ribs side, the skin separated partially from the ribs or delamination occurred in the ribs resulting in more skin bending. Lastly, due to the smaller size of the cells in the node specimens, smaller out-of-plane deformation was expected. This made it more difficult to spot the point at which buckling occurs. However, for the specimen with no visible damage, even the impacted ones, the pre-failure buckling pattern was easily noticed.

In addition to the above-mentioned discussion, the time frame at which the camera records might be too slow to capture the exact image at which the buckling occurs.

Secondly, the failure load of the tested specimens was affected by different occasions. Firstly, for the specimens with different potting thickness, different constraints on both sides existed. This resulted in a different failure load compared to the specimens with equal potting size, and compared to the model predictions as well. Another possible cause of the variation is the flatness of the sides of the specimen. Even though that the specimens were machined such that both surfaces are parallel, small angles were noticed between the machine surface and the specimen surface at the beginning of some tests. This could have resulted in secondary bending for some tests. There might be different causes for these angles, might be that the machining of some specimens or the blocks in the machine fixture was of low quality. Or simply that the top fixture block was loose from one side, resulting in seeing this variation before the start of the test. As the load started to increase linearly, these angles were not noticeable.

Another cause, that had larger effect on the node specimens than the cell specimens, was the initial damage in the specimen. This damage is not necessarily resulting from the impact, but also from the initial bending of the specimens and the delamination noticed after cutting the specimens. Since the

skin-rib separation was the first failure mode observed, specimens with initial delamination failed earlier.

### 6.5.3. Model improvements

In the initial modelling trials, maximum strain failure criterion was used instead of Tsai-Wu. The difference between the actual failure loads and the predictions turned out to be large for maximum strain criterion. Other criteria were also tried which turned to be aligning with the test results better, these included Tsai-Hill, and Hoffman. This concludes that criteria that allow to consider interactions between the different stress types are better in the prediction of failure of grid-stiffened structures. This makes sense due to: firstly, the existence of skin which happens to have different plies in different directions, which introduces couplings, specially in the case of asymmetric layup. Secondly, the ribs run in three different directions and in contact with the first skin ply, which can also result in stress couplings between the skin and the ribs. This being said, in the case of lattice structures, i.e., no skin, non-interactive criteria can be more accurate; because the structure consists mainly of UD plies along the ribs, which meet only at the nodes. In case of the specimen failing outside the node area anyway, the maximum stress and maximum strain criteria can be quite accurate in predicting the failure load.

One disadvantage of all these criteria is their inability of predicting the failure mode. As mentioned in chapter 2, grid-stiffened structures can fail in different ways, while the model can predict the strength quite accurately, and probably the location, it cannot tell what is the failure mode. Other failure criteria such as Hashin's and Puck's can do so, they are, however, less readily available in modelling software programs and more difficult to implement.

Secondly, damage initiation can also be included in the model to increase it is accuracy in predicting strength of the impacted specimens. From the non-destructive testing done on the impacted specimens, one can have an idea about how can the damage be realistically modelled. One could see that delamination often occurs in case of impacting cell specimens, from the c-scan images, this delamination can be measured and implemented in the model. That will require, however, using solid elements. In which case, the delamination can be modelled for example, by separating the elements in this region or creating a gap of a similar dimension to the measured one between the elements representing the different plies. For this study, shell elements, with the other modelling choices, were quite accurate in predicting the failure load.

# 7

# Conclusion and Recommendations

The last step at the end of the project is to check whether the research questions are answered or not, and provide recommendations for future work in the field. section 7.1 reflects on the research questions and concludes the project, followed by a list of recommendations in section 7.2.

## 7.1. Conclusion and discussion

The thesis project was done in collaboration with ATG Europe, and different industrial partners. The objective of the project was to evaluate the feasibility of using grid-stiffened structures on drones. The first step was then to perform a literature review, based on which the research questions were formulated. From the research study, it was found that very limited number of researches looked into using grid-stiffened structures for aeronautics applications. In addition, limited number of sources investigated reduction in the structure strength after impact damage. Hence, the approach was as follows:

- ATG decided to collaborate with an industrial partner, which provided the technical data for one of their new cargo drones. This drone was then used as a reference aircraft.
- The Fuselage was replicated using grid-stiffened structure, the design parameters for the new structure were selected in accordance with the provided loading cases and technical data, such that the new fuselage is able to withstand the loads caused by the worst loading conditions.
- Test coupons are manufactured and tested to check compliance with the damage tolerance requirements set by the airworthiness regulations. This was checked by performing compression after impact tests. These specimens were modelled using FEM software programs, the model setup was the same as the model created for the entire fuselage.
- In addition to the damage tolerance requirements, weight comparison between the current structure and the grid-stiffened structure is made to check whether there will be any weight savings.

After the compression testing was done, the data from the tests were analyzed and conclusion were made. Firstly, impact testing of the specimens proved the test specimens to have good damage tolerance properties. For cell specimens, none of the impacted specimens was unable to withstand the limit load. The requirements initially stated that BVID should be able to withstand the ultimate load, and the VID should be able to withstand the limit load. So was the case for node specimens, however, few outliers occurred for node specimens during impact tests and compression tests. The variations in the compression test results were already expected after the impact test, due to the inconsistency in the resultant damage. Some recommendations are derived from this test campaign for more conclusive test in the future, explained in section 7.2. Most of the outliers and other variations between the test results were justified, for example by manufacturing defects, flawed test setup, or wrong selection of specimen size. Different modelling approaches were tried, i.e., different type of analysis, different failure criteria, etc. The model was revisited after the test and some conclusions were made: (1) For grid-stiffened structures, interactive failure criteria provide more accurate predictions, (2) In case of thin skin and/or large cell sizes, large out-of-plane deformations are expected at an early stage. Hence, linear analysis can be very inaccurate.

### Research questions revisited

**Are grid-stiffened structures able to provide a damage-tolerant design?**
Based on the test results, it was seen that grid-stiffened structures can sustain high-impact energy levels, with either no damage, or small amount of damage. In case of visible damage, the structure was still able to carry loads higher than the limit load. Hence, the answer to this question is yes.

**Will using grid-stiffened structures result in lighter aircraft structure?**
The mass of the fuselage using grid-stiffened structure added up to 75 kg, the achieved mass is within the mass budget set by the manufacturer for this project, and competitive compared to the current solution. In reality, more weight is still expected to be added to the aircraft, for example, paint, attachments, etc. Given that no optimization was done during this project, further optimizations can result in further weight reductions. Hence, the answer to this question is, yes.

## 7.2. Recommendations

From the work done during this project, a list of recommendation for future work within the same research area is formulated. This section discusses them and divided them into different categories.

### 7.2.1. Impact test

A few recommendations can be driven from the results and the progress of the impact testing. The first thing to be discussed is the fixture. While it was discussed earlier that a simply supported fixture is the chosen for this test, a modified version of the fixture is proposed. For the cell specimen, a large deformation was seen during the test and the specimen acted as a trampoline. The same happened for the node specimens, but it was much less due to the smaller specimen size. This is not expected to happen if the fuselage is impacted, for example. A proposed solution would be to add the supporting rods that go over the entire edge instead of the pins used in this fixture. These rods should allow for rotation, this can be by having them connected to a ball-bearing mechanism for example, or by making the width of the contact edge of the specimen small enough to allow for rotation. When fixing the specimen, some pins were fixed against an area with skin only and no ribs underneath. This made it easy to unintentionally deform the skin when adjusting the screws. This also resulted in some parts of the specimens being more firmly fixed than the other. Another alternative way would be to have more pins along the edge, this could be an easier fix.

Secondly, it was noticed that there was a large variation in the resultant damage between the node specimens. It is expected that this happened due to factors, first, the use of an impactor was a small diameter, second, the ply drops in within the nodes. The impactor would constantly try to follow the path of the least resistance, within the nodes, there are regions with fewer plies number of plies as shown earlier in the c-scan images, 32 versus 16 in some spots, the resin pockets (and voids) for weaker spots in the region with fewer plies. Since the resin in the pockets had lower mechanical properties than the regions with fibers, it could be squeezed easier. This made the impactor move slightly in the horizontal plan at the moment of impact for some specimens, consequently, it was almost impossible to hit the same spot in every specimen. One of the reasons is that the impactor wiggles in the horizontal plan, up to a cm. Another reason is that the specimen was placed manually, and the fixture was pulled out to fix the new specimen every single time. The set of the following recommendations could help in minimizing these problems.

- Using an impactor with a diameter that is comparably bigger than the weak spots in the nodes.
- Having hard stops on the test bench where the fixture could be fixed to for all the tests.
- Having a test bed within the fixture itself, or hard stops for the specimen. This, however, requires high cutting precision to get all the specimens to be the same size, which was not possible for the manufactured panel as discussed earlier. Hence, this should be planned for well in advance, taking into consideration the available cutting machines and their precision.
- Make sure to minimize the wiggling in the impactor. However, this could be a difficult task and probably not possible depending on the test setup. A mechanical idea can be proposed. However, they will affect the energy that goes into the impact. A conical structure that guides the impactor to the intended impact spot.

As explained earlier, the energy levels at which certain damage was expected were not correct. Which is indeed a difficult to estimate since these can easily vary with the variation of the design parameters. Even with the same structure and design, things like specimen size can make a large difference in the resultant damage. Hence, it is wise for such project to investigate the expected damage beforehand and select the appropriate energy levels accordingly. Up to the author's knowledge, such expectations cannot be easily made from analyses. However, looking into this problem can be an interesting research topic, predicting the corresponding impact energy that cause BVID and VID depending on the structural design. Another way would be experimental, which is rather costly. Because this implies that more specimens of the same dimensions have to be manufactured and impacted as well, depending on the impact trials, the proper energies are selected. For now, the followed approach in this thesis remains the optimal one, especially if the other recommendations are followed. The approach included trials with specimens from scrap material, e.g., extra parts from the large panel that are not needed. While the conclusions were not very accurate, they did give a good indication about the expected impact levels for this structure.

### 7.2.2. Specimen size

The first set of recommendations are concerning the specimen size. Based on the test done, a few modifications in the specimen size are hereby suggested for future project work:

**Recommendations:**

1. Both node specimens and cell specimens are to have the same size
2. There should be complete cells and not only fractions of cells in the specimen, this was particularly an issue for node specimens.
3. If the specimen is tested along the hoop rib, then it is recommended to have the same number of hoop ribs in both the node and cell specimens.

**Explanation:**

1. During impact testing, cell specimens should much more flexibility due to their size, this was clearly noticed in the high-speed camera footage. This might have had an effect on the impact results, since for cell specimens much more energy went into the rebounce of the impactor, which is clearly noticed by the height reached by the impactor after the impact.
2. For the cell specimens, it was noticed that the damage is always contained within the impacted cells. For the node specimens, it was noticed that the ribs tend to separate from the skin and/or delaminate near the edge supported on the fixture. It is expected that less damage will be caused in the ribs if complete cells were surrounding the impacted node.
3. From the test results, it seemed that the hoop rib had the greatest effect in the load carrying capability of the specimen. That was concluded because the node specimens failed approximately at half the load at which the cell specimens failed. The main difference between both specimens, next to the size, was that the cell specimens had two hoop ribs instead of one, which was the case for the node specimens. To further validate this hypothesis, and to accurately investigate the effect of other factors, for example, number of cells and/or nodes in the tested specimen, the specimen size and the number of hoop ribs have to be the same.

# References


[1] *Aircraft Blue Book*. https://aircraftbluebook.com/Tools/ABB/ShowSpecifications.do. Accessed: 20-11-2022.

[2] Ahmad Alhajahmad and Christian Mittelstedt. “Minimum weight design of curvilinearly grid-stiffened variable-stiffness composite fuselage panels considering buckling and manufacturing constraints”. In: *Thin-Walled Structures* 161 (2021), p. 107526.

[3] “Anisogrid composite lattice structures – Development and aerospace applications”. In: *Composite Structures* 94.3 (2012), pp. 1117–1127.

[4] GOLDSWORTHY W. B. “Thermoplastics technology applied to manufacturing of grid-stiffened structures”. In: *Proc. 44th Intl. SAMPE Symposium, 1999* (1999).

[5] Donald Baker et al. “Optimal Design and Damage Tolerance Verification of an Isogrid Structure for Helicopter Application”. In: *Collection of Technical Papers - AIAA/ASME/ASCE/AHS/ASC Structures, Structural Dynamics and Materials Conference* 2 (Feb. 2003).

[6] S.W. Beckwith. “Filament winding vs. fiber placement manufacturing technologies”. In: 44 (Mar. 2008), pp. 54–55.

[7] M. Buragohain and R. Velmurugan. “Study of filament wound grid-stiffened composite cylindrical structures”. In: *Composite Structures* 93.2 (2011), pp. 1031–1038.

[8] Mridul Buragohain and Velmurugan Ramachandran. “Optimal Design of Filament Wound Grid-stiffened Composite Cylindrical Structures”. In: *Composite Structures* 93 (Jan. 2011), pp. 1031–1038.

[9] *Cell specimen impact video*. https://youtube.com/shorts/9eodAeW-8Kk?feature=share. Accessed: 08/01/2023.

[10] McDonnell Douglas Astronautics Company. *ISOGRID DESIGN HANDBOOK*. 1973.

[11] G. Davies and P. Irving. “9 - Impact, post-impact strength and post-impact fatigue behaviour of polymer composites”. In: *Polymer Composites in the Aerospace Industry*. Ed. by P.E. Irving and C. Soutis. Woodhead Publishing, 2015, pp. 231–259.

[12] USA Department of defense. *Composite material handbook*. Vol. Volume 3. Polymer Matrix Composite Materials Usage, Design, and Analysis.

[13] V. Díaz, E. Olmo, and M. Frovel. “Design & development of advanced composite isogrid structural solutions for primary structures of future reusable launch vehicle”. In: Jan. 2009.

[14] *EASA advisory material AMC 20-29. Composite aircraft structure. Annex II 26/07/2010*.

[15] *Flying-V aircraft*. https://www.tudelft.nl/en/ae/flying-v. Accessed: 03-12-2022.

[16] John Higgins and Barry VanWest. “NDE and repair of damaged Minotaur fairing shell”. In: *Composite Structures* 67.2 (2005). US Air Force Workshop Damage Assessment of Composite Structures, pp. 189–195.

[17] P.E. Higgins et al. “Design and testing of the Minotaur advanced grid-stiffened fairing”. In: *Composite Structures* 66 (Oct. 2004), pp. 339–349.

[18] Steven Huybrechts, Steven E. Hahn, and Troy Edward Meink. “GRID STIFFENED STRUCTURES : A SURVEY OF FABRICATION , ANALYSIS AND DESIGN METHODS”. In.

[19] Steven Huybrechts et al. “Manufacturing theory for advanced grid stiffened structures”. In: *Composites Part A-applied Science and Manufacturing* 33 (2002), pp. 155–161.

[20] Prakash Jadhav, P. Raju Mantena, and Ronald F. Gibson. “Energy absorption and damage evaluation of grid stiffened composite panels under transverse loading”. In: *Composites Part B: Engineering* 37.2 (2005), pp. 191–199.

[21] Benjamin Jenett et al. “Digital Morphing Wing: Active Wing Shaping Concept Using Composite Lattice-Based Cellular Structures”. In: *Soft Robotics* 4 (Oct. 2016).

[22] C. Kassapoglou. *Design and Analysis of Composite Structures*. 2010.

[23] Samuel Kidane. “Buckling analysis of grid stiffened composite structures”. In: 2002.

[24] T.D. Kim and C.A. Rotz. “Warping of flat composite isogrid panels”. In: *1997 IEEE Aerospace Conference*. Vol. 1. 1997, 271–277 vol.1.

[25] Ivar te Kloeze. “Design, Analysis, Manufacturing and Testing of Load Introductions in Grid-Stiffened Composite Structures”. In: 2015.

[26] Ming Li and Hualin Fan. “Multi-failure analysis of composite Isogrid stiffened cylinders”. In: *Composites Part A: Applied Science and Manufacturing* 107 (2018), pp. 248–259.

[27] R. Mackay. *Wellington in action*. Squadron-signal publication, 1986.

[28] Vincent K. Maes. “Design, Analyis, Optimization and Testing of Grid-Stiffened Composite Structures”. In: 2015.

[29] Vincent K. Maes, Leonid Pavlov, and Sahak M. (Samo) Simonian. “An efficient semi-automated optimisation approach for (grid-stiffened) composite structures: Application to Ariane 6 Interstage”. In: *Composite Structures* 209 (2019), pp. 1042–1049.

[30] Reza Mohammadzadeh Gheshlaghi and H. Akbulut. “Modeling and Analysis of Anisogrid Lattice Structures Using an Integrated Algorithmic Modelling Framework”. In: (Oct. 2020).

[31] V Murthy and Soundarapandian Santhanakrishnanan. “Isogrid lattice structure for armouring applications”. In: *Procedia Manufacturing* 48 (Jan. 2020), e1–e11.

[32] Leonid Pavlov, Bart J. Smeets, and Sahak M. Simonian. “Optimization of a Composite Lattice Satellite Central Cylinder Structure Using an Efficient Semi-automated Approach”. In: *57th AIAA/ASCE/AHS/ASC Structures, Structural Dynamics, and Materials Conference*. American Institute of Aeronautics and Astronautics, Jan. 2016.

[33] Leonid Pavlov et al. “DEVELOPMENT LOGIC AND BUILDING BLOCK TESTING APPROACH FOR PREPREG LATTICE SATELLITE CENTRAL CYLINDER APPLICATIONS”. In: ().

[34] Leonid Pavlov et al. “DEVELOPMENT OF MASS AND COST EFFICIENT GRID-STIFFENED AND LATTICE STRUCTURES FOR SPACE APPLICATIONS”. In: (Sept. 2016).

[35] *Pipistrel Nuuva V300 Aircraft*. `https://www.pipistrel-aircraft.com/nuuva-v300/`. Accessed: 20-11-2022.

[36] “Review of composite sandwich structure in aeronautic applications”. In: *Composites Part C: Open Access* 1 (2020), p. 100004.

[37] S. Shroff. “Design, Analysis, Fabrication and Testing of Grid-Stiffened for Fuselage Applications”. PhD thesis. 2014.

[38] Sonell Shroff, Ertan Acar, and Christos Kassapoglou. “Design, analysis, fabrication, and testing of composite grid-stiffened panels for aircraft structures”. In: *Thin-Walled Structures* 119 (2017), pp. 235–246.

[39] G. Totaro and Felice De nicola. “Recent advance on design and manufacturing of composite anisogrid structures for space launchers”. In: *Acta Astronautica* 81 (Dec. 2012), pp. 570–577.

[40] V.V. Vasiliev, V.A. Barynin, and A.F. Rasin. “Anisogrid lattice structures - Survey of development and application”. In: *Composite Structures* 54 (Nov. 2001), pp. 361–370.

[41] V.V. Vasiliev and A.F. Razin. “Anisogrid composite lattice structures for spacecraft and aircraft applications”. In: *Composite Structures* 76.1 (2006). Fifteenth International Conference on Composite Materials, pp. 182–189.

[42] Dan Wang and Mostafa Abdalla. “Buckling Analysis of Grid-Stiffened Composite Shells”. In: July 2014.

[43] Jun Wu, Weiming Wang, and Xifeng Gao. “Design and Optimization of Conforming Lattice Structures”. In: (Oct. 2019).

# A

# NDT results

## A.1. Cell specimens

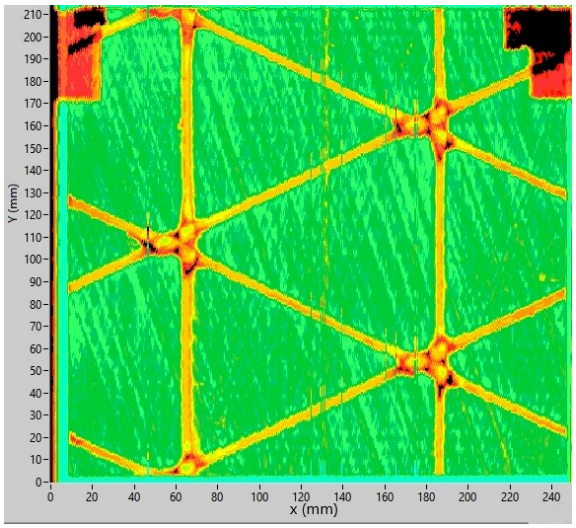


Figure A.1: Specimen P1-C1-UN, PristineJ

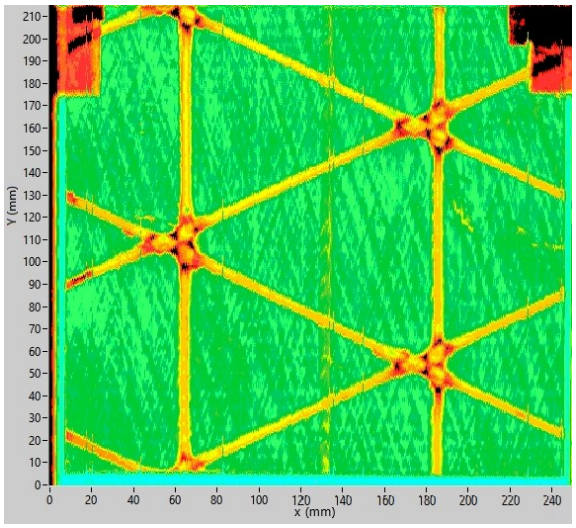


Figure A.2: Specimen P1-C2-UN, Pristine

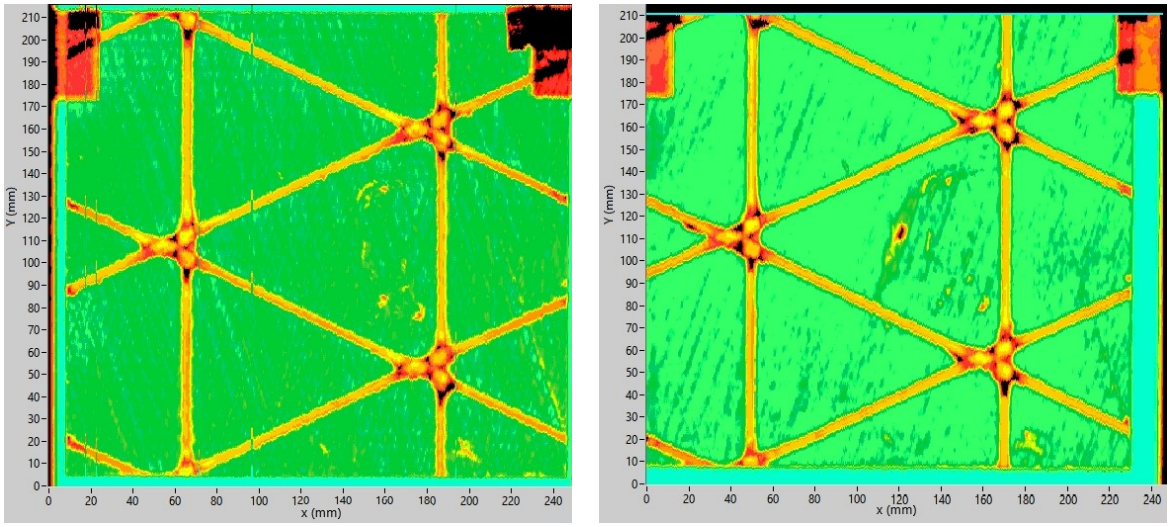


(a) Pre-impact (b) Post-impact

Figure A.3: Specimen P1-C3-BV, 15J

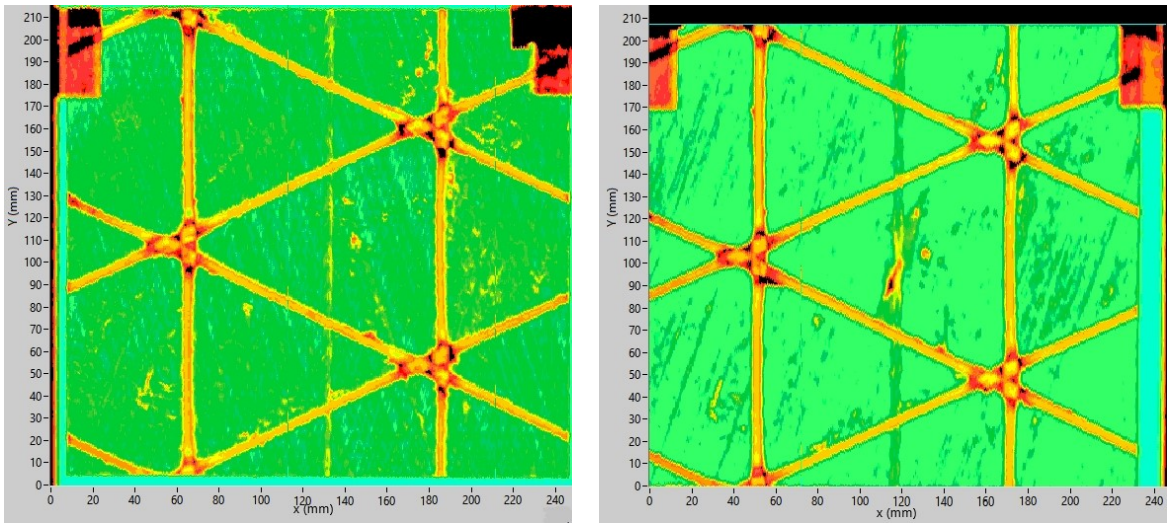


(a) Pre-impact (b) Post-impact

Figure A.4: Specimen P1-C4-VD, 20J

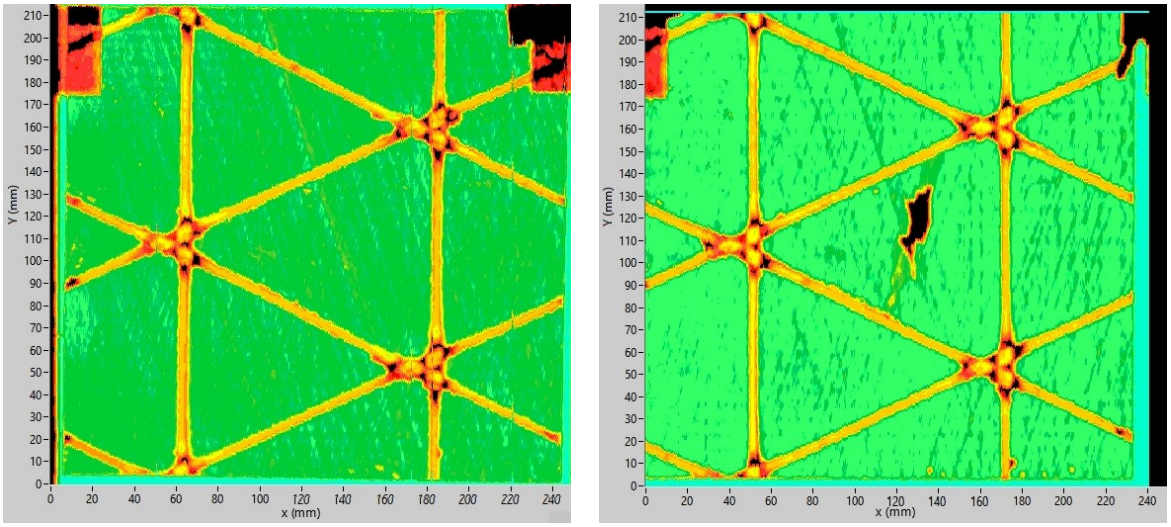


(a) Pre-impact (b) Post-impact

Figure A.5: Specimen P1-C5-VD, 27J

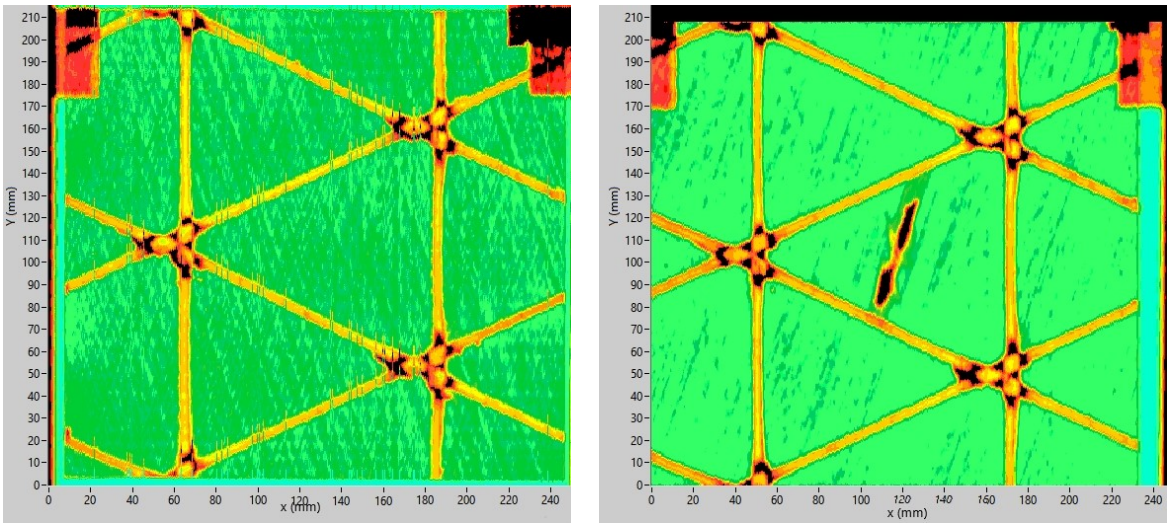


(a) Pre-impact (b) Post-impact

Figure A.6: Specimen P2-C6-UN, 36J

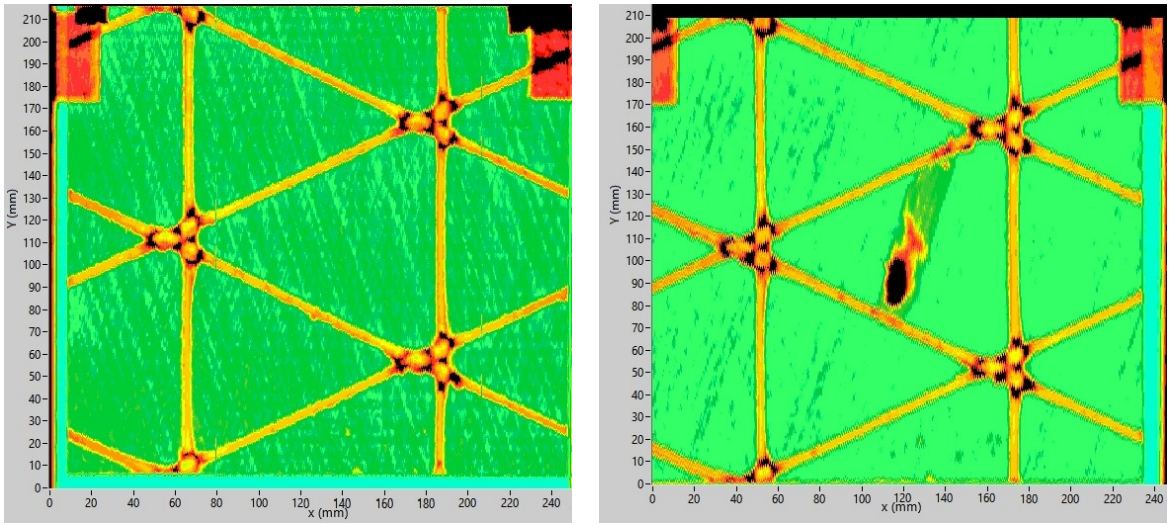


(a) Pre-impact (b) Post-impact

Figure A.7: Specimen P2-C7-BV, 36J

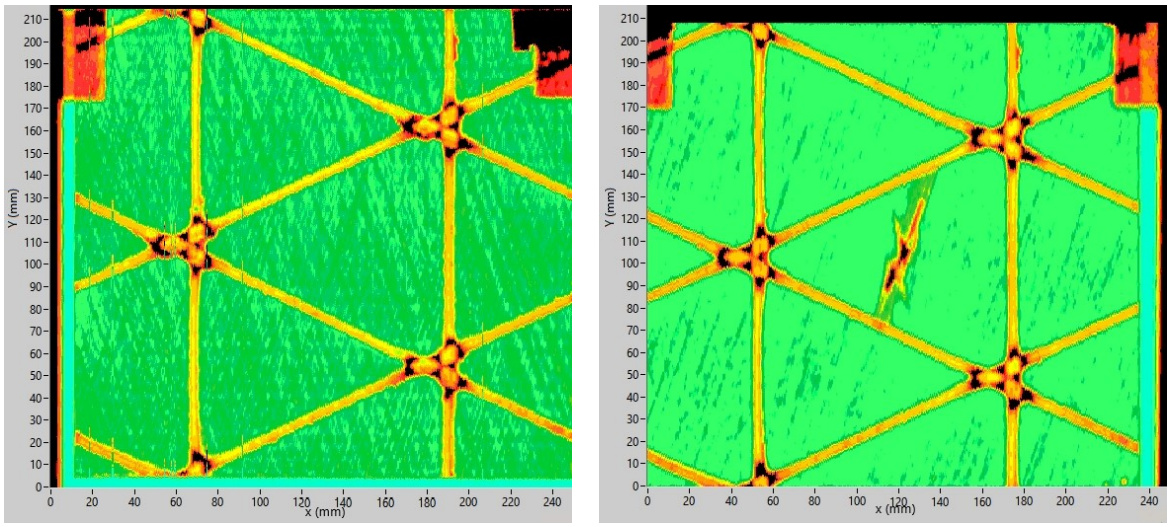


(a) Pre-impact (b) Post-impact

Figure A.8: Specimen P2-C8-BV, 36J

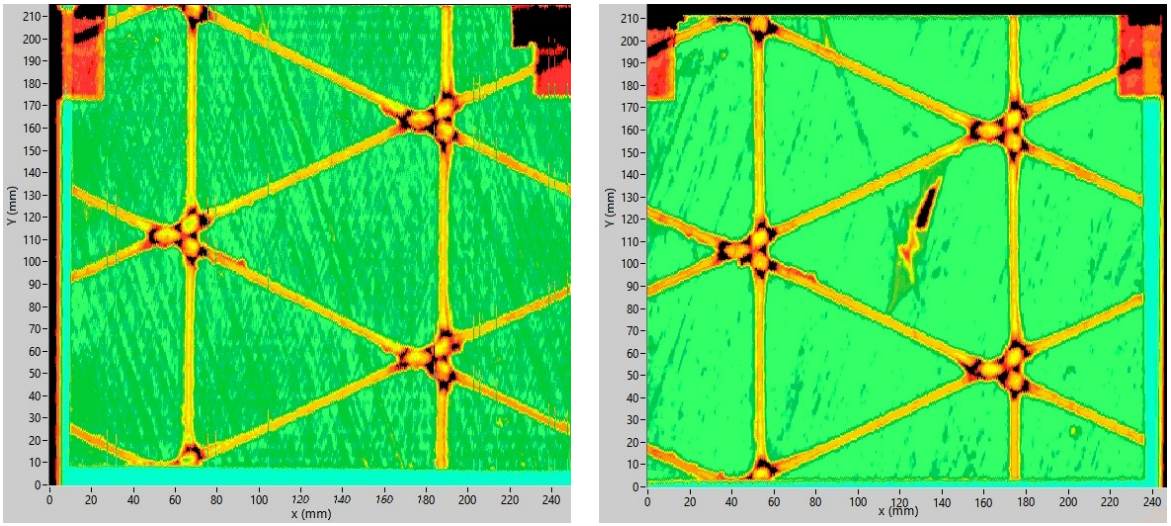


(a) Pre-impact (b) Post-impact

Figure A.9: Specimen P2-C9-VD, 30J

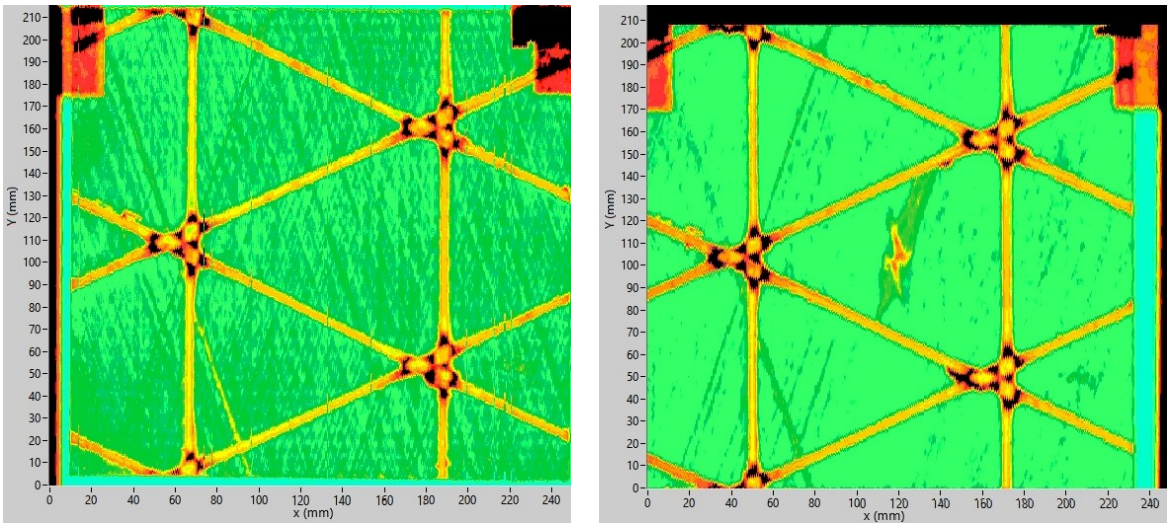


(a) Pre-impact (b) Post-impact

Figure A.10: Specimen P2-C10-SP, 33J

## A.2. Node specimens

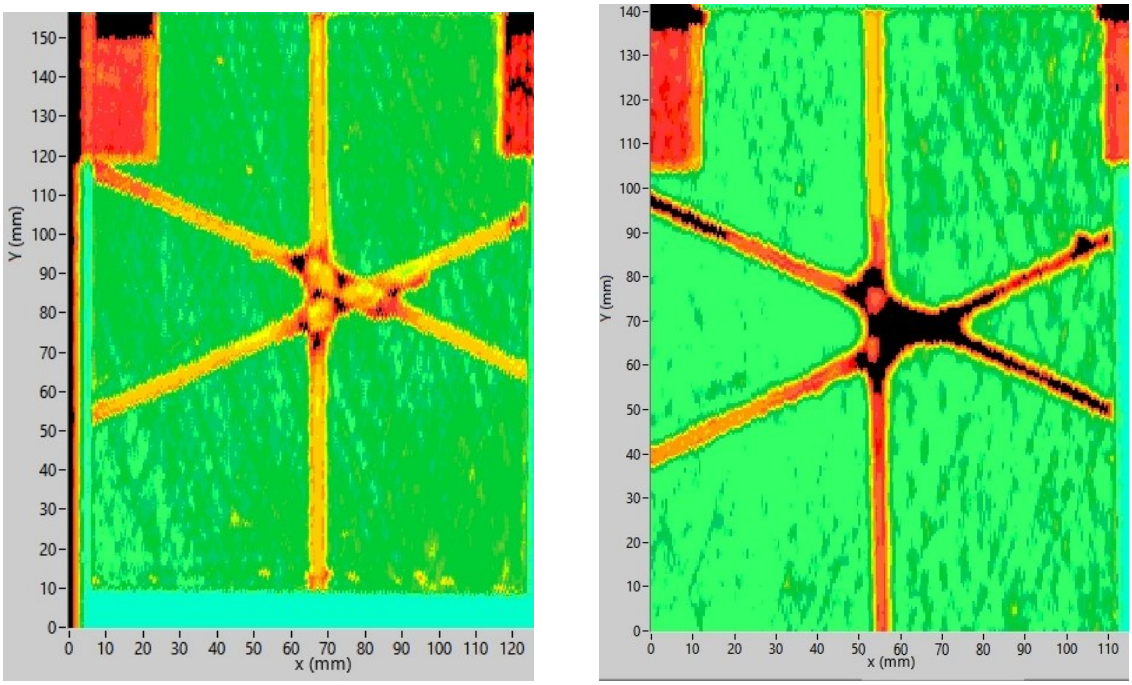


(a) Pre-impact (b) Post-impact

Figure A.11: Specimen P1-N1-UN, 37J

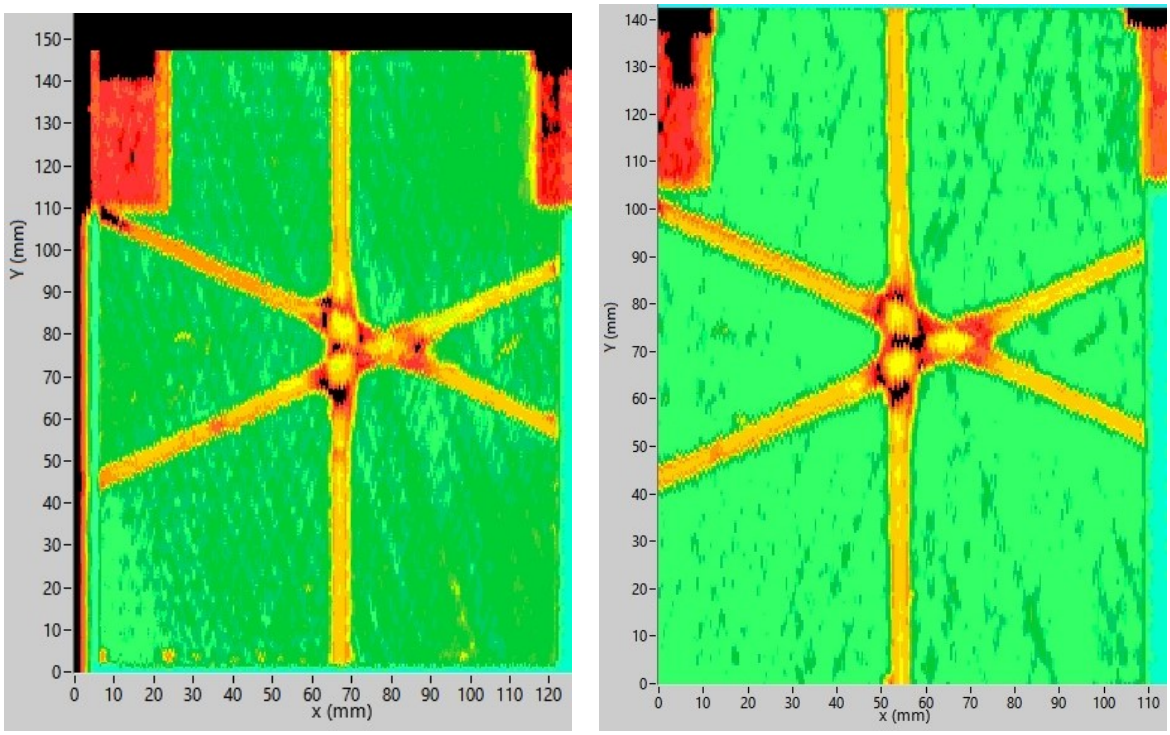


(a) Pre-impact (b) Post-impact

Figure A.12: Specimen P1-N2-VD, 43J

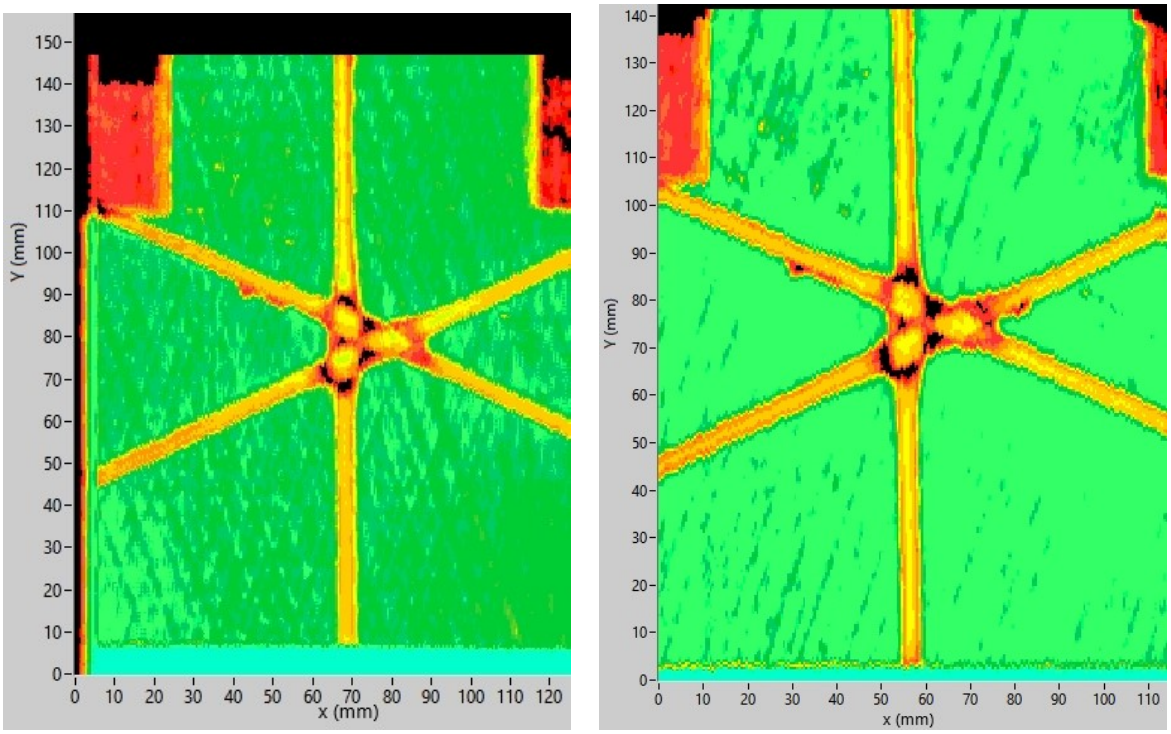


(a) Pre-impact (b) Post-impact

Figure A.13: Specimen P1-N3-BV, 30J

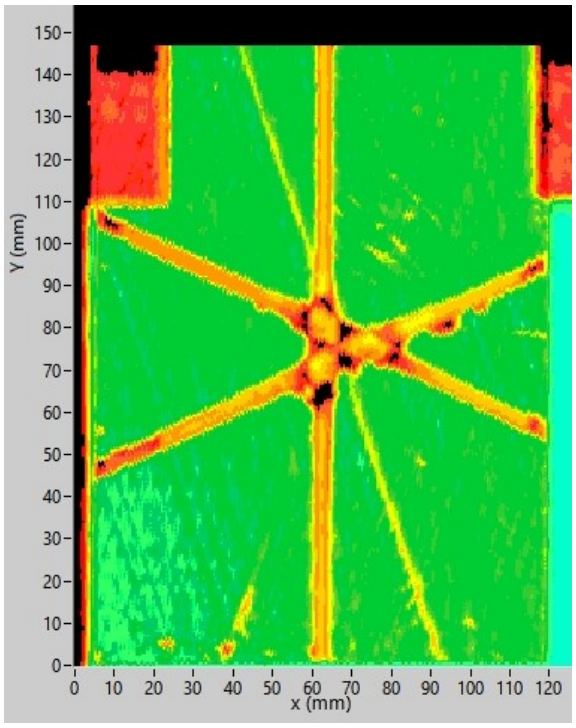


Figure A.14: Specimen P1-N4-UN, Pristine

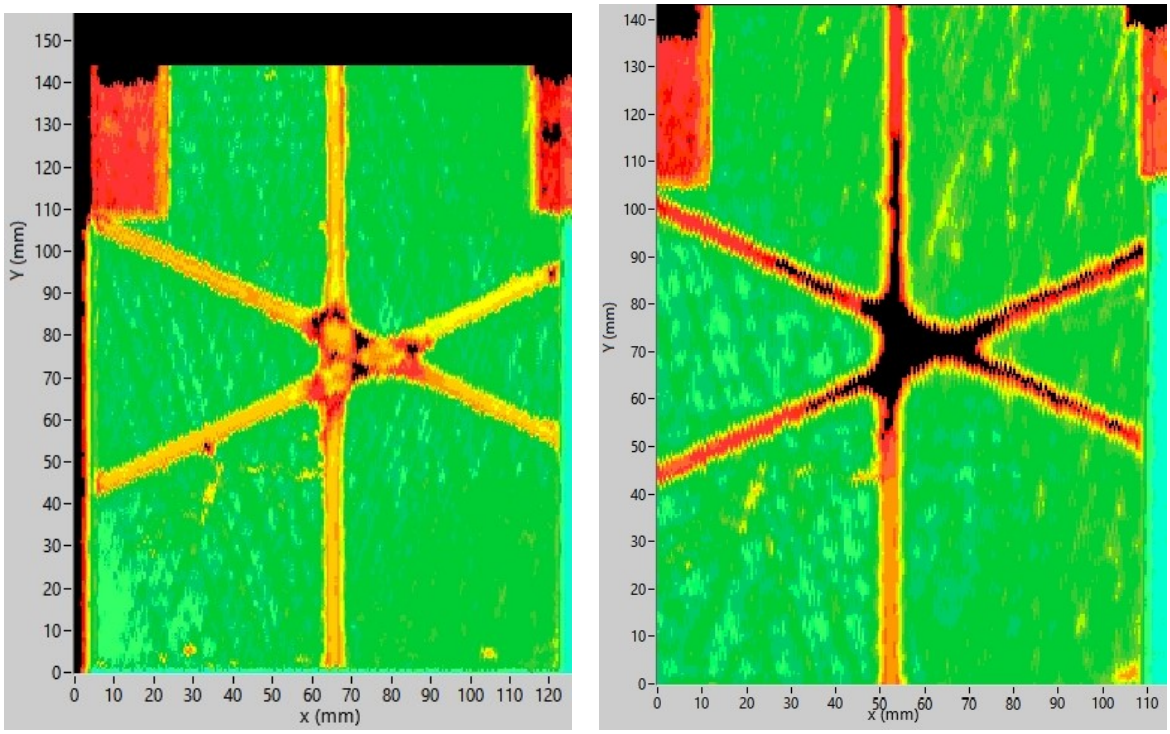


(a) Pre-impact (b) Post-impact

Figure A.15: Specimen P1-N5-BV, 43J

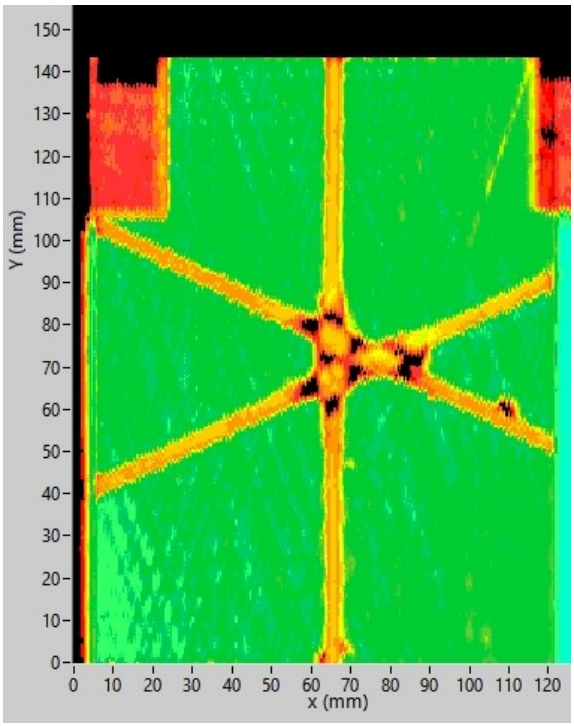


Figure A.16: Specimen P2-N6-UN, Pristine

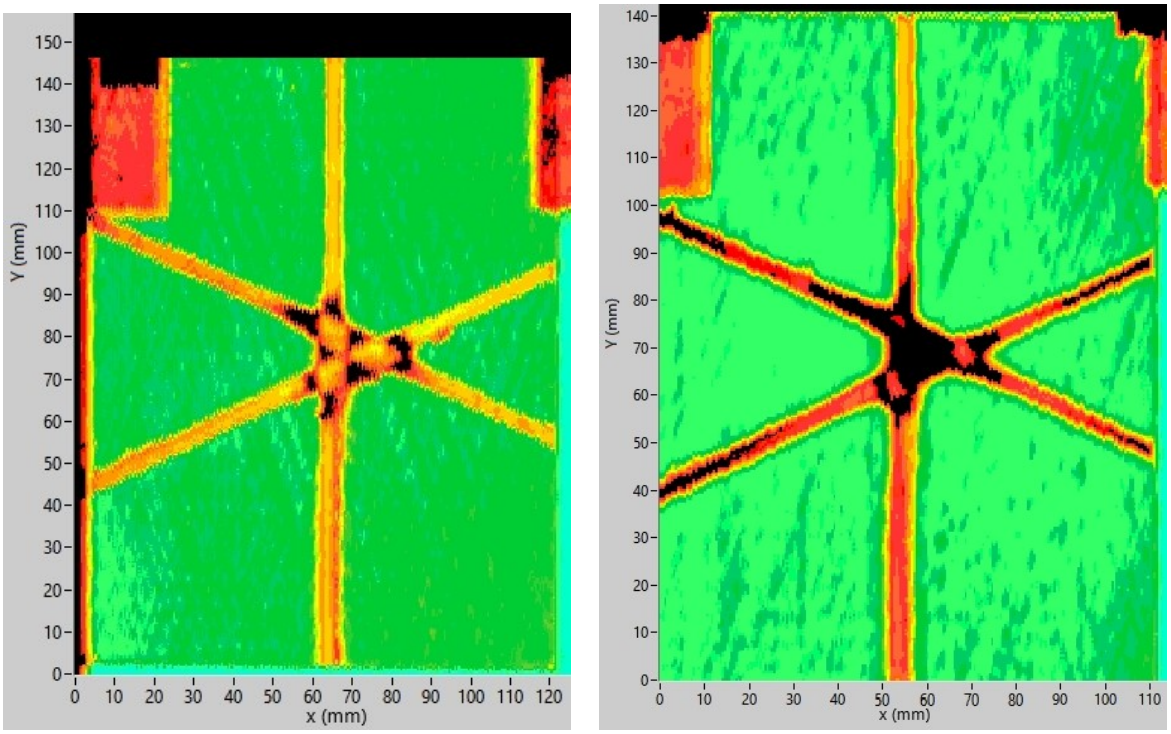


(a) Pre-impact (b) Post-impact

Figure A.17: Specimen P2-N7-BV, 43J

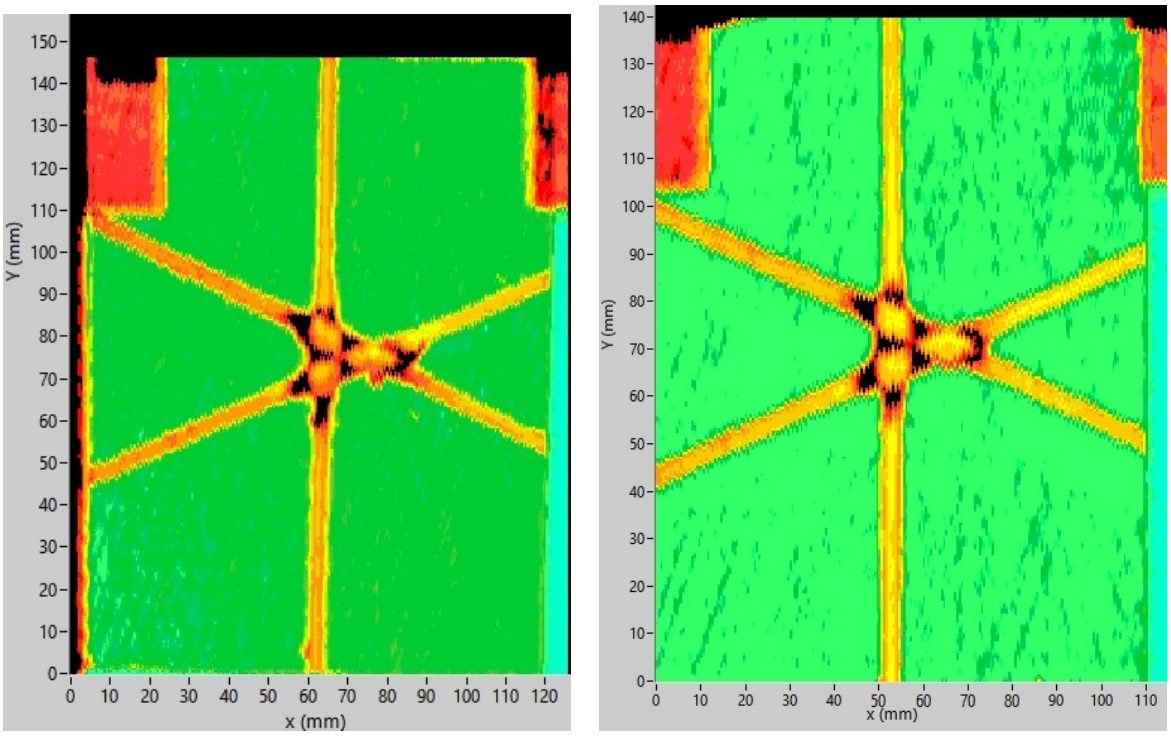


(a) Pre-impact (b) Post-impact

Figure A.18: BVID, Specimen P2-N8-VD, 37J

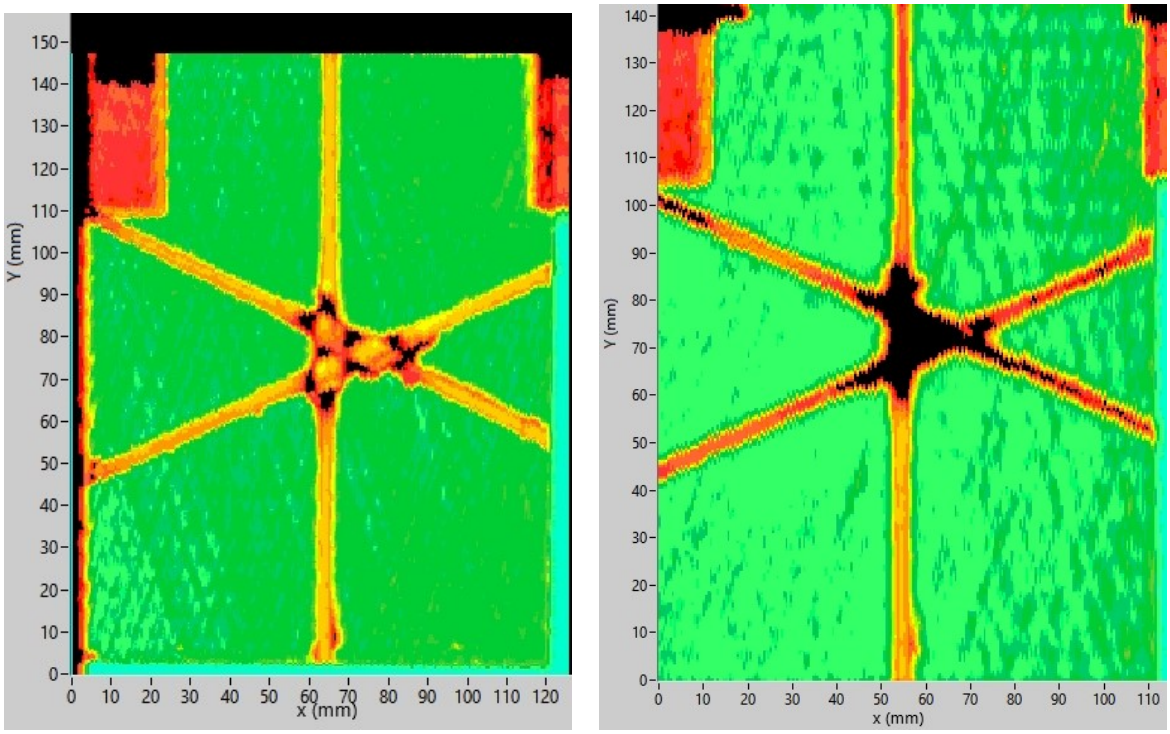


(a) Pre-impact (b) Post-impact

Figure A.19: Specimen P2-N9-VD, 55J

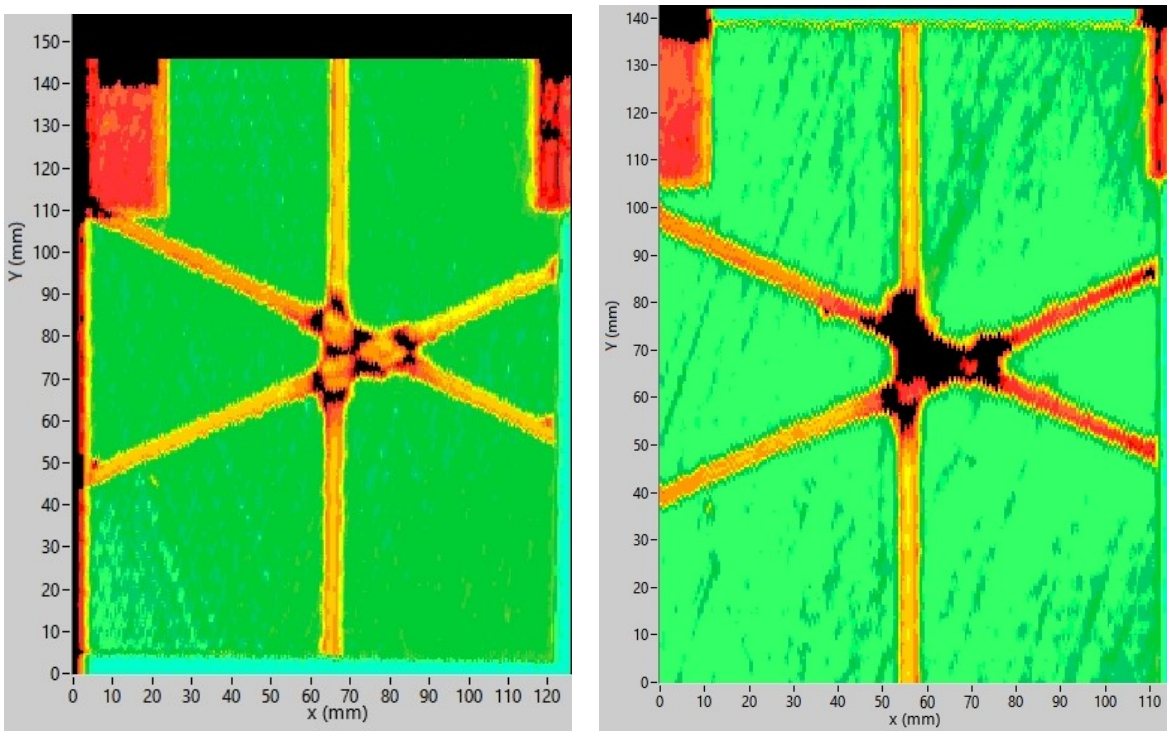


(a) Pre-impact (b) Post-impact

Figure A.20: Specimen P2-N10-SP, 37J

# B

# Test Results

## B.1. Cell specimens

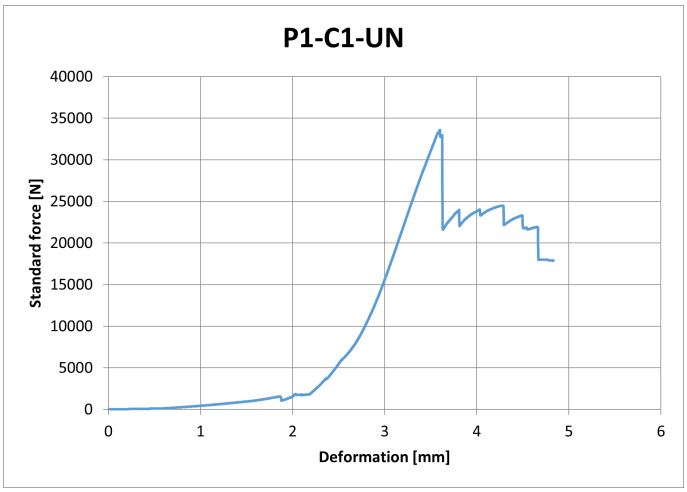


Figure B.1: Compression test results, specimen P1-C1-UN

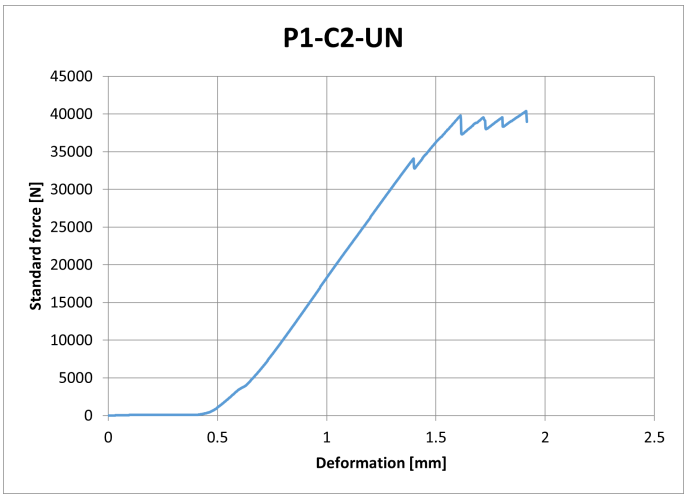


Figure B.2: Compression test results, specimen P1-C2-UN

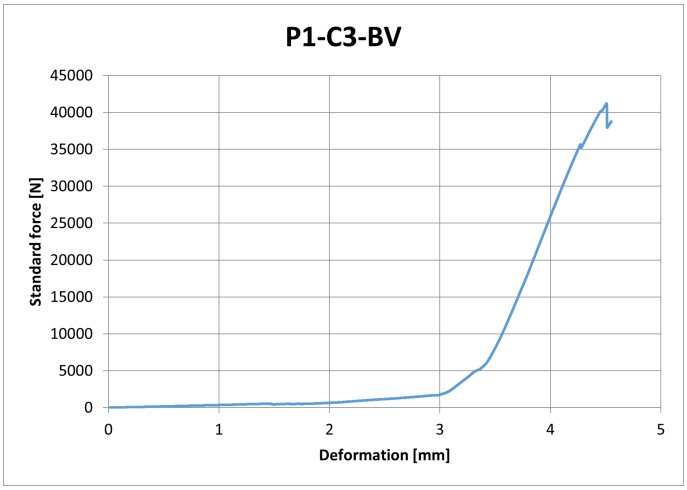


Figure B.3: Compression test results, specimen P1-C3-BV

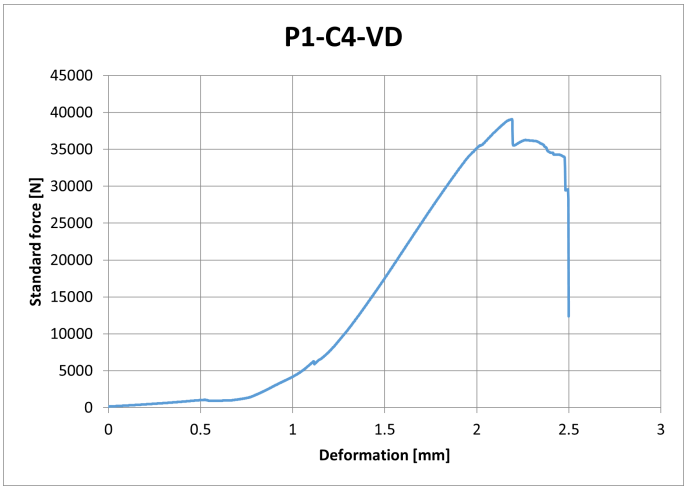


Figure B.4: Compression test results, specimen P1-C4-VD

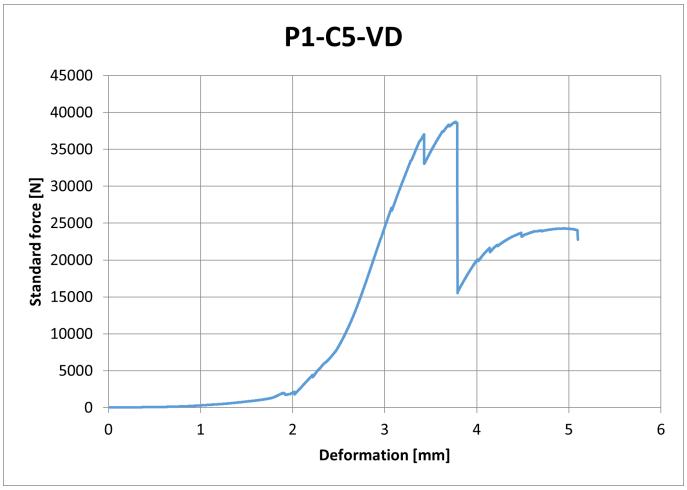


Figure B.5: Compression test results, specimen P1-C5-VD

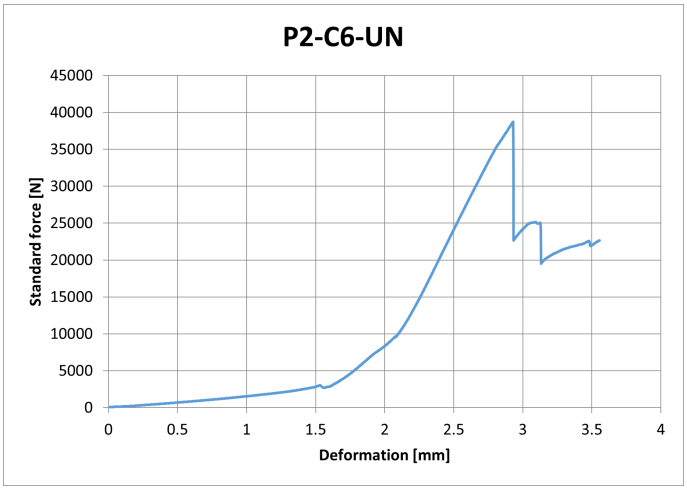


Figure B.6: Compression test results, specimen P2-C6-UN

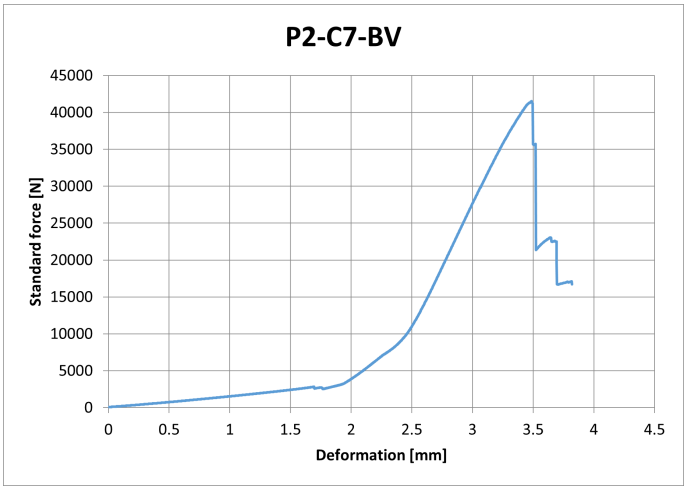


Figure B.7: Compression test results, specimen P2-C7-BV

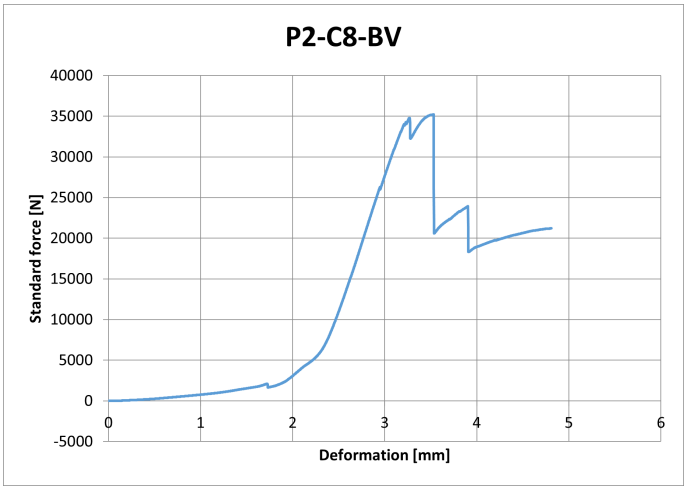


Figure B.8: Compression test results, specimen P2-C8-BV

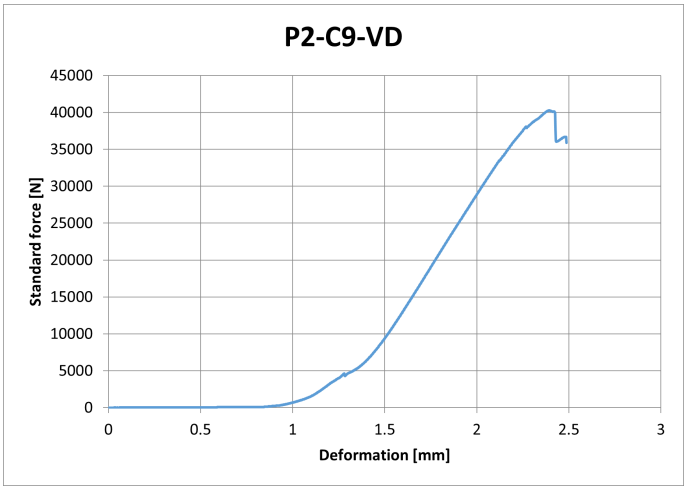


Figure B.9: Compression test results, specimen P2-C9-VD

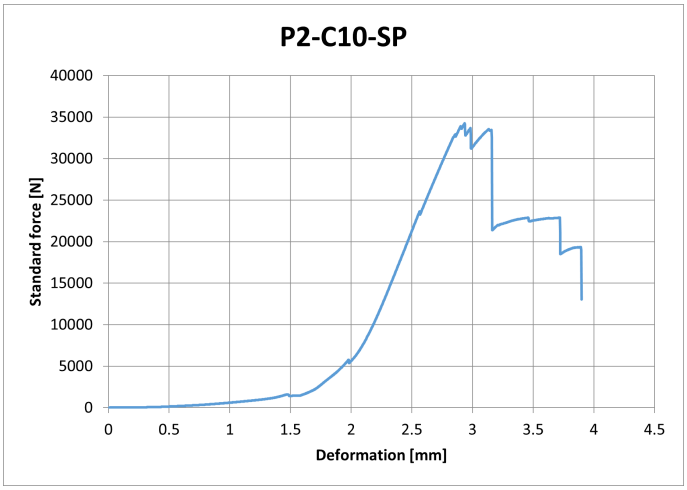


Figure B.10: Compression test results, specimen P2-C10-SP

## B.2. Node specimens

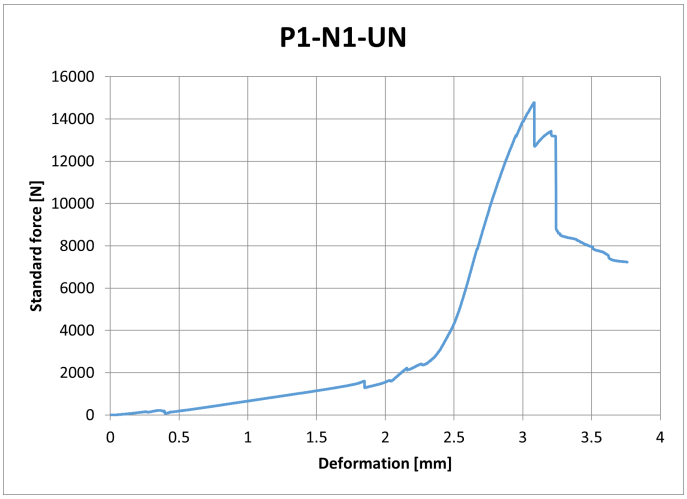


Figure B.11: Compression test results, specimen P1-N1-UN

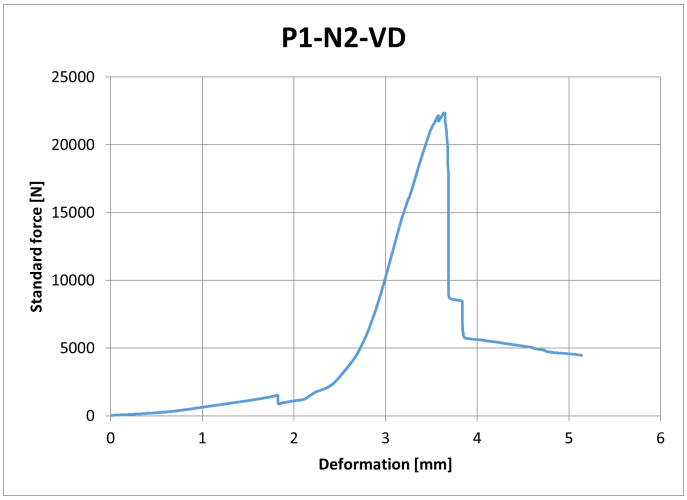


Figure B.12: Compression test results, specimen P1-N2-VD

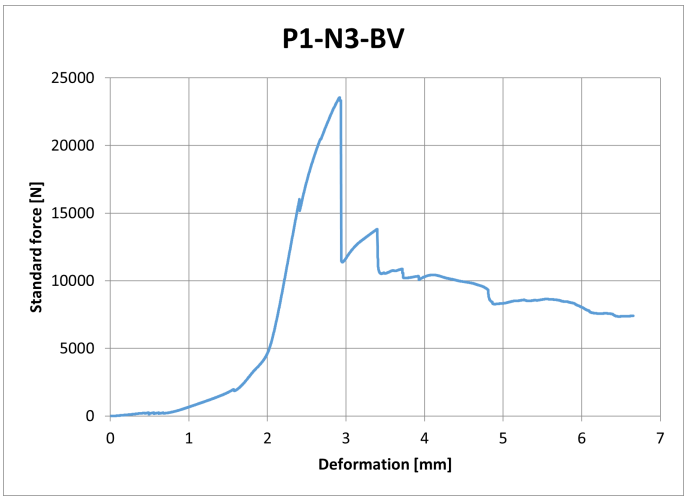


Figure B.13: Compression test results, specimen P1-N3-BV

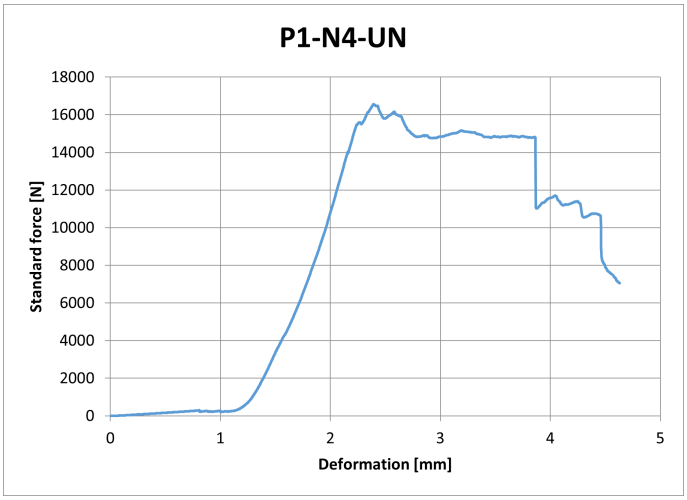


Figure B.14: Compression test results, specimen P1-N4-UN

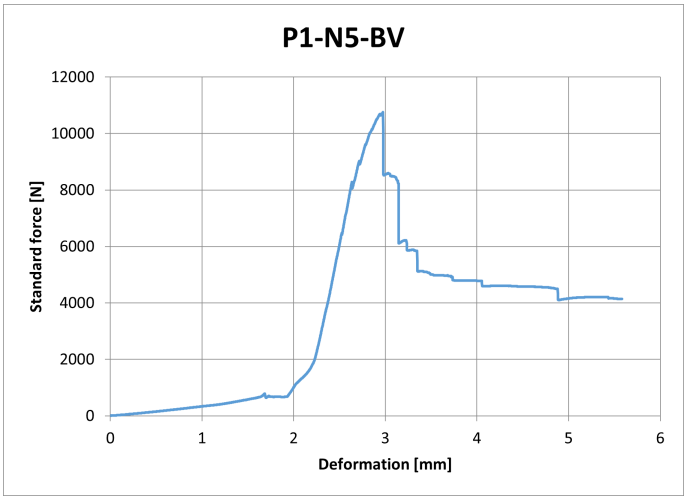


Figure B.15: Compression test results, specimen P1-N5-BV

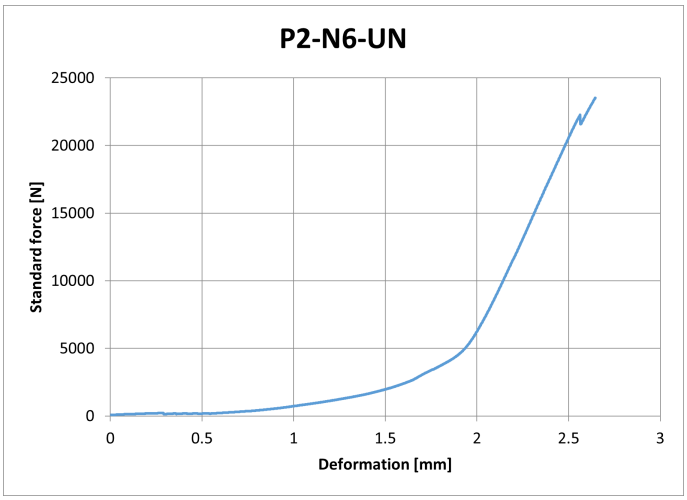


Figure B.16: Compression test results, specimen P2-N6-UN

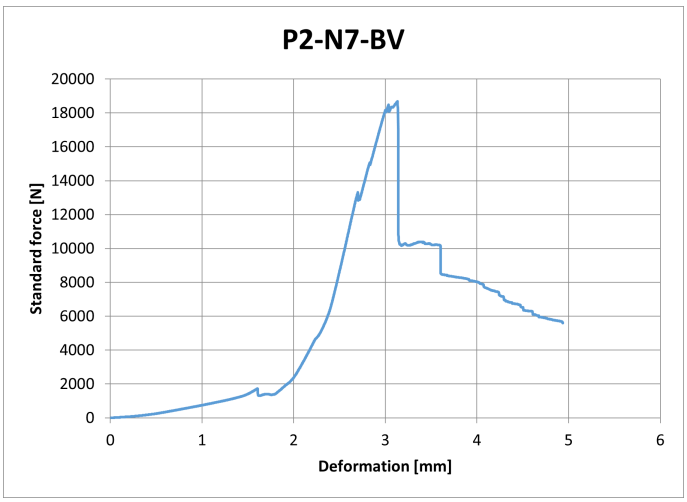


Figure B.17: Compression test results, specimen P2-N7-BV

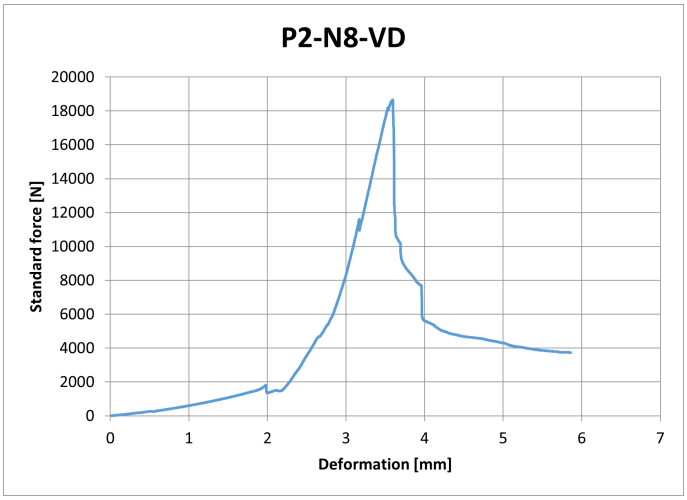


Figure B.18: Compression test results, specimen P2-N8-VD

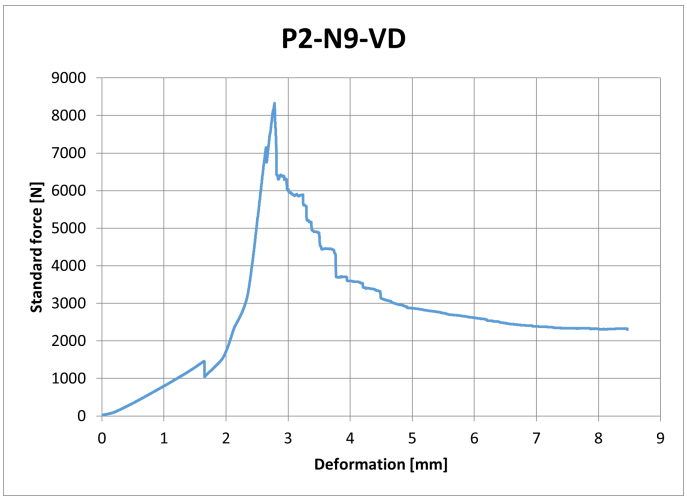


Figure B.19: Compression test results, specimen P2-N9-VD

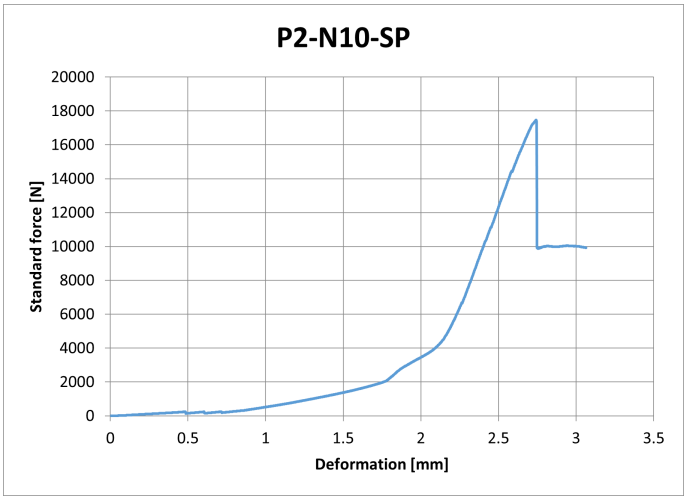


Figure B.20: Compression test results, specimen P2-N10-SP

# C

# Impact trials

This section is intended to discuss the pre-testing trials on scrap material. These were initial impacting trials done on scrape material to validate the choice of the energy levels selected in the early stages of the project, and to ensure that the test setup is working as intended. There were a couple of differences between the two sets of specimens used here and in the actual test:

- The specimens used for these trials were cut from the excess material in the panel after cutting the actual specimens. Hence, they had different dimensions than the other set of specimens.
- The specimens tested had different dimensions. However, they often had to be cut to fit into the already existing fixture
- The actual specimens always had the impact spot in the center point of the specimen, this was not the case with the trials specimens
- Due to the shortage in scrape material, specimens where no visible damage noticed on both sides were used in subsequent impacts

The tests proceeded from lower to higher energies, based on the resultant damage from one test, the next impact energy was selected. The tests done were as mentioned below:

**Node impact, 25 mm impactor, 25J**
No visible damage was seen, not on the skin side or on the grid side.

**Node impact, 25 mm impactor, 35J**
No visible damage was seen, not on the skin side or on the grid side.

**Node impact, 25 mm impactor, 60J**
No visible damage was seen on the skin side. However, clear delamination could be seen on in the ribs, Figure C.1.

(a) Skin side (b) Grid side

Figure C.1: Impact trial, node specimen, 60J

**Node impact, 4.5 mm blunt impactor, 30J**
A small rounded dent was seen, but no noticeable damage. It was not clear whether it could be considered a damage or not, Figure C.2.

(a) Impactor used (b) Skin side

Figure C.2: Impact trial, node specimen, 30J

**Node impact, 3 mm pointed impactor, 35J**
Visible damage with fine crack on the skin side. And separation between the ribs and the skin with small delamination in the ribs and the skin, Figure C.3.

(a) Impactor used (b) Skin side (c) Grid side

Figure C.3: Impact trial, node specimen, 35J

**Cell impact, 25 mm impactor, 6J**
It was suggested to try this as the BVID first, but no damage was seen at all.

**Cell impact, 25 mm impactor, 10J**
No damage was seen at all.

**Cell impact, 25 mm impactor, 15J**
A tiny crack was seen on the skin side, Figure C.4.

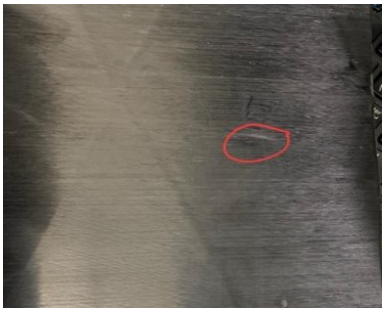

Figure C.4: Impact trial, cell specimen, 15J

**Cell impact, 25 mm impactor, 25J**
The impactor fully penetrated the skin, and no rebounce occurred. The damage was contained within the impacted cell and did not expand to the neighbor cells.

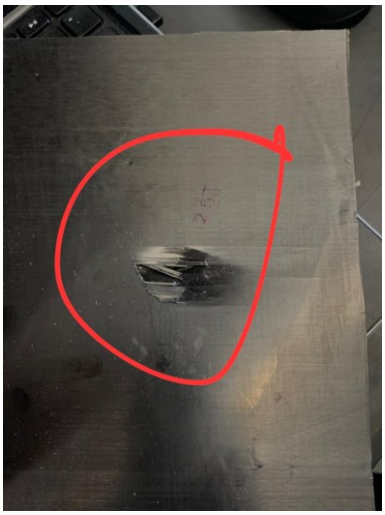

Figure C.5: Impact trial, cell specimen, 25J

**Conclusion:**
After the trials were made, it was decided to change the initially set energy levels, which were 10J for BVID and 25J for VID for both node and cell specimens, to the following:

1. **Cell specimens**
   - 15J for BVID
   - 25J for VID/Clearly VID
2. **Node specimens**
   (a) 27-38J for BVID
   (b) 35-40J for VID/Clearly VID

For node specimens, it was not clear what energy levels would cause the required damage, since for some trial no damage seen and for the rest clearly VID was seen. It was concluded that the required damage can be achieved by an impact energy in the middle between the two used energies. Hence, a range to try within was set for node specimens, for both types of impact.

# D

# Optimization approach

The maximum index failures were found in the top back side of the fuselage, where the rear wing is attached, pointed to in Figure 4.2. Consequently, this area was deemed the most critical. It formed the basis for the optimization model. The global model, with its size, would be very time-consuming to analyze and computationally expensive; hence, the model was reduced to only this area, and a separate model was created, Figure D.1. The easiest way to do so was by meshing the entire fuselage, and then deleting the unwanted area. Thus, one could make use of the project script, and mesh patterning in FEMAP.

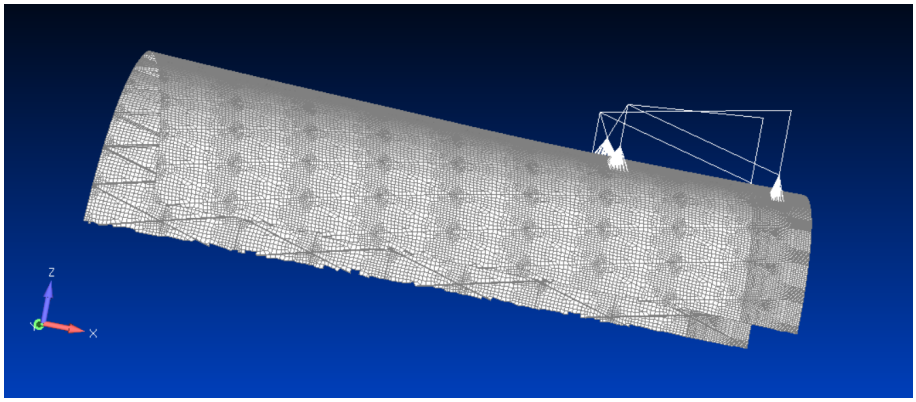


Figure D.1: Optimization model

The critical zone was the area around the rear wing attachment, it was decided, however, to extend the model further to capture the far field area towards the mid-section of the fuselage. To further simplify the model, only the loads from the rear wing were considered. This had a couple of reasons, firstly, the magnitude of the loads from the rear wing are considerably higher compared to other loads. In the region to be optimized, the only other load that could be applied would have been the moment at the rear, applied on the end cross-section in Figure 4.2. This means, any loads, apart from the loads from the rear wing, will have to be translated to the cut edges of the optimization section, which would impose some complications. To ensure the current model is representative, the same design parameters as the global, and the analysis results from this section are compared. The difference has to be small to deem it an adequate approach.

The optimization is done together with a sensitivity analysis. This starts by selecting the parameters to investigate. For this structure, there are many parameters, skin thickness, rib height, rib width, rib separation, and rib angle. One can either choose a few to investigate or do all, which will be much more time-consuming. During the analysis, all the parameters are fixed except the one to be investigated, then this parameter is changed and the effect on the strength and stiffness, and weight of the structure

are investigated. Different values are often tried, for example starting with the maximum and minimum within the design space pre-determined, then selecting a couple of values in between. Depending on the parameter, more or less iterations might be needed. The idea then is to have useful numbers to use in the design. For such a project, one could think of creating ratios, for example, strength increase per one millimeter increase in rib height, and weight increase per one millimeter. These numbers can be combined to get the design parameters. When it comes to the design, other considerations can be taken into account. For example, if the small rib angles result in a better-performing structure, manufacturability, or product quality can be an issue. In which case, a minimum value is set, and other parameters can be changed. It is important to consider other factors like this, since there is an infinitely large number of combinations of design parameters, and one would often need to narrow down the options as much as possible.

The process of running this analysis is similar to what is explained earlier in this chapter. One first starts with the CAD model of a cylinder, where the desired design parameters are chosen. This is then followed by importing the .stp file into the model in FEMAP to create the geometry. The cylinder is then meshed, by meshing a small section and patterning it. The projection script is then used to create the meshed fuselage. Unwanted elements are deleted and only the ones representing the area of interest shown in Figure D.1 are kept. The cut edges are then constrained, and the loads from the rear wing are applied using RBEs. For every single parameter, the rest of parameters are fixed, and the same process is repeated for different values of the selected parameters. For some parameters, however, the CAD model is not needed, and it can easily be changed in FEMAP, for example, the skin thickness, and rib width, and rib height. Rib separation and rib angle can only be changed in the CAD model. This could be extended into another project, to create an automated optimization software. There are few bits that exist already, at ATG for example the worked on an Auto-meshing script. This with the projection script, and other scripts, can be used to create an optimization API for Nastran. Easier said than done, such a project can be a master thesis on its own.

For this project, if a further optimization is done, it can result in one of two things: either a better design will be created, showing that further potential exists for lighter structures. Or it will re-assure the current design.